Prompt gamma-ray imaging of nanoparticles for in vivo range verification in proton therapy

Sonia Escribano Rodríguez

Doctor of Philosophy

Physics

University of York

July 2022

I would like to dedicate this thesis to my family, for all their support.

Declaration

I declare that this thesis is a presentation of original work and I am the sole author. This work has not previously been presented for an award at this, or any other, University. All sources are acknowledged as References.

Acknowledgements

A mis padres, por creer firmemente en mí y haberme apoyado en este camino, y en tantos otros. Nada de esto habría sido posible sin vosotros. A mi hermana y mis sobrinos, Elsa, Enzo y próximamente Emma, por haberme alegrado cada día del doctorado por videollamada. Gracias por estar siempre a mi lado.

I would like to thank my supervisor, Dr. Stefanos Paschalis, for giving me the opportunity to work on this very interesting project, and for guiding me during the PhD, providing valuable feedback during our weekly meetings.

My appreciation also goes to my friend and mentor, Dr. Suso Pereira-López, for his patience and for helping me countless times during this journey.

This experimental work would not have been possible without the help of the people from the mechanical workshop and the research technicians, particularly Chris Silk for helping me cool down the detector and bringing all the equipment to Birmingham University. My thanks also go to Harry Kiewiet and Dr. Tony Price for helping me during the experiments at KVI-CART and Birmingham University, respectively and to Dr. Gonzalo Vallejo-Fernandez for developing the magnetite targets.

I would also like to thank the people in the Nuclear Physics Group at York that shared this journey with me. Special mention to Gustavo, for being an amazing friend and helping me feel at home during the last three and a half years. Diolch yn fawr Rhidian for proofreading this thesis and all the Asda trips.

A mis amigos Luis, Duva y Virginia por haberme acompañado en esta experiencia. Y por supuesto, gracias a mi amiga Juncal, por ser un pilar fundamental a pesar de la distancia.

En último lugar, quiero darle las gracias a Aina, por enseñarme que con dedicación y aguante todo es posible.

Abstract

Proton therapy is an emerging modality for cancer treatment that induces a better dose conformation, compared to traditional photon radiotherapy. In vivo range verification techniques are required to fully exploit the advantages of proton therapy. In the past few years, the use of nanoparticles as dose enhancers has increased due to their potential amplifying the radiation induced damage. This thesis studies the combination of both techniques, as it will generate a dose enhancement, while verifying the range of the protons with the detection of the characteristic prompt gamma-rays emitted by the nanoparticles.

To investigate the feasibility of performing prompt gamma-ray imaging using characteristic gamma rays from nanoparticles, a magnetite (Fe_3O_4) target was developed in house, consisting of a solution of nanoparticles diluted in water. The detection system consists of two different types of detectors: a CLLB scintillator and a hyper-pure germanium semiconductor.

In-beam measurements were performed at the University of Birmingham (UK) and KVI-CART (Netherlands) at three different beam energies. In the current work, it is found that the CLLB detector allows for the distinction of different target compositions using the coarse energy regions in the prompt gamma-ray spectrum. The HPGe detector allows to resolve many more characteristic prompt gamma-rays with a much higher peak-to-background ratio, compared to the scintillator detector, and obtain their intensity profile.

The results presented suggest that the combination of both methods provides a viable way to determine the range of the protons and confirm the location of the tumour area. The present work also indicates that measuring gamma-ray yields, using a treatment dose and nanoparticle concentration similar to the ones applied in clinic, are sufficient for localising the intensity profile of the characteristic gamma rays from the nanoparticles with a precision of a few mm, hence providing an additional tool for in-vivo range verification.

Contents

List of Figures

List of Tables

Glossary

3D 3-Dimensional.

ADC Analog-to-Digital Converter.

AuNP Gold Nanoparticles.

BP Bragg Peak.

DAQ Data Acquisition.

DEF Dose Enhancement Factor.

DPP Digital Pulse Processing.

EM Electromagnetic.

EPR Enhanced Permeability and Retention Effect.

FoV Field of View.

FPGA Field-programmable Gate Array.

FWHM Full Width Half Maximum.

HPGe High-Purity germanium.

IMPT Intensity Modulated Proton Therapy.

MC Monte Carlo.

MCA Multi-channel Analyser.

MCS Multiple Coulomb Scattering.

NPs Nanoparticles.

PBS Pencil Beam Scanning.

PD Photodiodes.

PDF Probability Density Function.

PET Positron Emission Tomography.

PG Prompt gamma-ray.

PGI Prompt gamma-ray imaging.

PGNI Prompt gamma-ray non imaging.

PGS Prompt gamma-ray spectroscopy.

PGT Prompt gamma-ray timing.

PHA Pulse Height Analysis.

PMMA Polymethyl Methacrylate.

PMT Photomultiplier Tubes.

PSD Pulse Shape Discrimination.

PT Proton Therapy.

QA Quality Assurance.

QE Quantum Efficiency.

SiPM Silicon Photomultipliers.

SOBP Spread-Out Bragg Peak.

SPAD Single-Photon Avalanche Photodiodes.

Chapter 1

Introduction

Radiotherapy is a modality in cancer treatment that delivers ionising radiation to destroy cancerous cells and reduce the tumoural volume. There are two types of radiotherapy depending on where the irradiation originates:

- Internal radiation therapy: radioactive sources are placed inside the patient's body, allowing for a higher dose in a smaller area. The nature of the radioactive source can be a solid, a liquid or a gas that emits alpha, beta or gamma particles that target the desired areas. If the source is a solid, it can be placed directly inside the human body (brachytherapy) or linked to a cell-targeting molecule (molecular therapy). On the contrary, if the source is liquid the treatment is called systemic therapy and it travels through the blood.

- External radiation therapy: the radiation source is placed at a distance from the patient. Traditionally, X-rays or electrons were produced by a linear accelerator to treat malignant tumours, however in the past decade the use of heavy and/or charged particles has increased notoriously, developing a new modality called hadrontherapy. The two main charged particles for therapy are protons and carbon ions.

The development of proton therapy has lead to commissioning over 90 proton therapy centres worldwide, with at least 41 more under construction and 30 in planning stage. In the United Kingdom two NHS-funded proton therapy facilities have been constructed: University College London Hospital (UCLH) NHS Foundation Trust in London and Christie NHS Foundation Trust in Manchester. A third NHS centre has also been operating in the UK

delivering low energy proton therapy at The Clatterbridge Cancer Centre NHS Foundation Trust in Merseyside. The Rutherford Cancer Centres are part of a private UK network that offers proton beam therapy, and they have three different locations: The Rutherford Cancer Centre South Wales in Newport, The Rutherford Cancer Centre North East in Bedlington and the Rutherford Cancer Centre Thames Valley in Reading. The expansion in proton beam facilities, not only in UK but worldwide, reflects the increased adoption of proton therapy as a radiation treatment technology.

In this chapter I will firstly introduce proton therapy (PT), and compare it with traditional photon therapy. After describing the physical basis of proton interaction with matter, several range verification techniques will be reviewed. The use of nanoparticles as dose enhancers is also discussed, as the aim of the project is to combine these two techniques to prove the feasibility of nanoparticles as dose enhancers and gamma emitters, so they can be used in conjunction to increase the dose while simultaneously verifying the range.

1.1 Proton therapy: Overview

Proton therapy is a hadron therapy modality that utilises a high energy proton beam for cancer treatment. The energy range of the protons used for treatment varies between 75 and 250 MeV, which corresponds to a penetration length of 4.62 to 37.94 cm in water.

The energy deposition of a proton beam creates a characteristic dose peak, called Bragg Peak (BP). The BP has a high dose gradient that allows the sparing of healthy tissues distal to the tumour, reducing the irradiation in non-cancerous structures nearby. The shape of the BP is dominated by the interaction of the protons with matter, and how their energy loss depends on the speed of the protons.

1.1.1 Protontherapy and X-ray therapy

Traditional X-ray or photon treatments have a high entrance dose, depositing most of the beam energy at the entrance of the beam path, and this energy deposition decreases with the depth in the human body. While traditional treatments deliver extra dose before and after the tumour, the accurate placement of the BP in the tumour area reduces the entrance dose significantly and almost eliminates the exit dose, as shown in figure 1.1.

Nowadays, conventional radiotherapy with photons is the main modality for cancer treatment due to its low cost and availability, while proton therapy treatments are specially indicated for three types of tumours:

- Tumours close to critical structures: the dose gradient reduces the energy received by critical structures that may have a lower resistance to radiation because they are more sensitive to radiation damage.

- Paediatric tumours: it allows to minimise the dose in healthy tissue, reducing the risk of long-term side effects.

- Depth tumours: to reach tumours located deeper in the organism, the beam has to cross many structures, so reducing the relative dose applied to them is crucial.

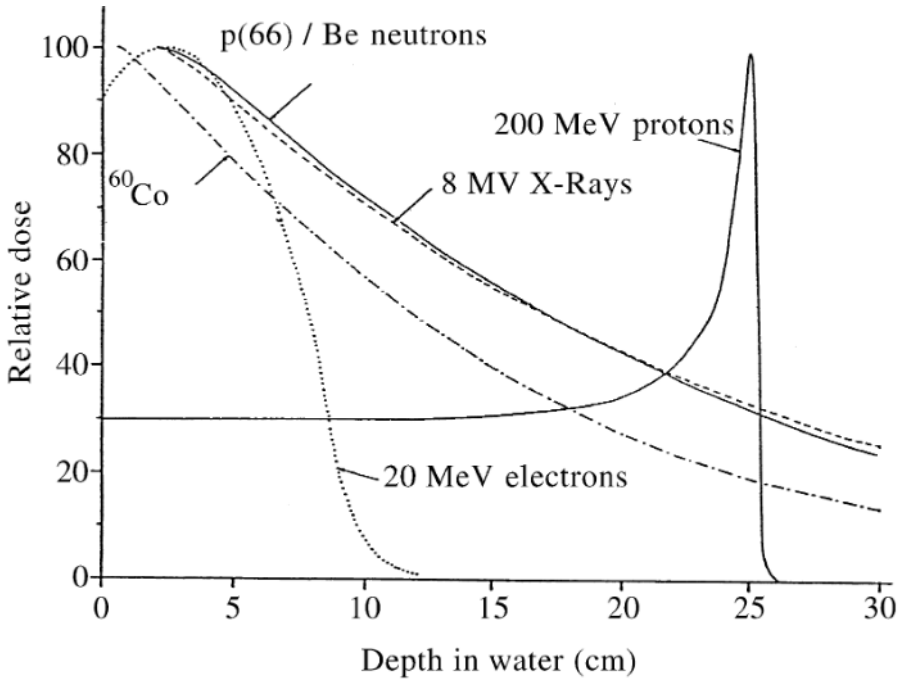

Figure 1.1: Depth-dose curves for photons (from a cobalt source and an 8 MeV linear accelerator), neutrons and 200 MeV protons. The highest dose for protons is released at the end of their path, producing the Bragg peak [1].

1.1.2 PBS and IMPT

The aim of PT is to deliver a homogeneous dose distribution to the target volume. The primary proton beam out of an accelerator is a collimated well-circumscribed pencil, but in order to uniformly irradiate the whole tumoural region a manipulation of the beam must be performed [2]. In the past decade, pencil beam scanning (PBS) has been the technique used to conform the dose to a tumour. The beam targets one small part of the tumour at a time, and the dose from all the points together forms the conformal dose. PBS proton therapy, also known as intensity modulated proton therapy (IMPT) delivers non-uniform dose distributions from each treatment field, creating a uniform dose in the target volume after superimposing the dose contributions from all fields [3]. In order to obtain a homogeneous dose distribution in the target volume, a superposition of many BPs with different energies must be created. The sum of all the BPs spreads out in depth, creating the spread-out Bragg peak (SOBP) that uniformly covers the tumoural region, as shown in figure 1.2.

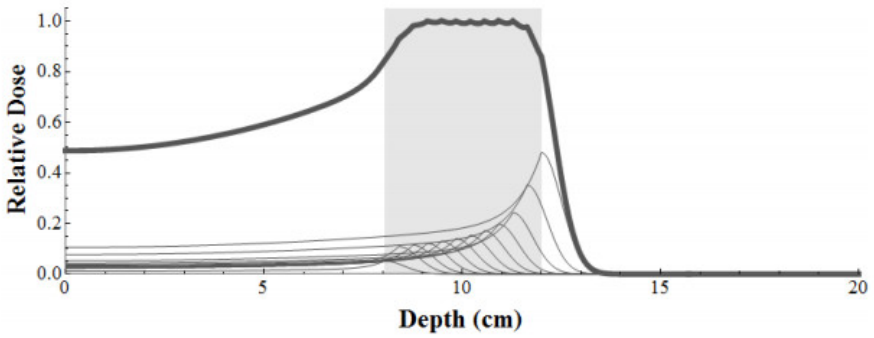

Figure 1.2: Relative dose of a SOBP curve (thick curve) comprised of 12 individual Bragg Peaks (thin curves). The shaded region shows the range of targeted depth [4].

1.1.3 Range uncertainties in proton therapy

To fully exploit the advantages of PT, the range of the protons needs to be calculated as accurately as possible during the treatment planning and delivery process, minimising the unnecessary dose to healthy tissues [5]. A wrong calculation of safety margins has more severe consequences in proton therapy than in photon therapy, due to the high dose gradient in the BP. Therefore, a shift in the range will lead to undershooting or overshooting during the treatment, causing unnecessary damage to the patient.

Proton beams have a finite range in tissues, whose value is affected by the characteristics of the tissue they interact with. The precision and accuracy of the treatment planning and delivery are affected by the uncertainties in the proton range that arise from many different sources: internal organ motion, patient setup, anatomical variations, biological considerations and dose calculation approximations [6].

Therefore, tracking the range of the proton beam is an essential part of the quality assurance (QA) process. During this procedure, the range is generally measured with an ion chamber for pretreatment range verification [7]. The acceptable range uncertainty varies between institutions, but traditionally they have adopted a generic range margin of 3.5% of the beam range in water, plus a 1 mm expansion along the beam direction to account for uncertainties in the patient's setup and organ motion that could not be measured during the QA process [8; 9]. For this reason, it is essential to verify the range of the proton beam online, to mitigate the uncertainties during the delivery of the treatment. Several range verification methods have been studied in the past two decades, and are discussed in the following section.

1.2 Range verification methods

Protons have a finite range which has an inherited spread and the prediction of its exact value can be affected by the uncertainties. To fully exploit the advantages of proton therapy, monitoring the beam range is crucial since it will reduce the effect of the aforementioned uncertainties, discussed in section 1.1.3.

In the past few years, many research groups have focused on the study of in-vivo range verification techniques, particularly in the ones related to the detection of gamma rays created as secondary radiation during the interaction of the proton beam with the tissue nuclei. Two types of gamma rays have been mostly studied: correlated back-to-back gamma rays produced in pairs, created after an electron-positron annihilation, or gamma rays from the direct de-excitation of an excited nucleus.

1.2.1 Positron emission tomography (PET)

Positron emission tomography (PET) is the pioneer nuclear medicine technique for range verification in hadrontherapy, and the use of these images for range verification was firstly pro-

posed at the end of the 20th century [10]. PET consists on the detection of the 3-Dimensional (3D) distribution of short-lived positron emitting nuclei generated during the irradiation, creating an image of the beta decay activity after the proton irradiation. This method produces a volumetric non-invasive verification of the proton range by quantifying the metabolic activity during the treatment, or at the end of the dose delivery [11].

PET measures the two annihilation photons produced after an emitted positron interacts with the surrounding electrons present in the human body, as shown in equation 1.1. Due to energy conservation laws, and because the cross section for this process is maximum after the positron has been slowed down, each of the emitted photons has an energy of 511 keV, corresponding to the rest masses of the annihilating particles.

$$e^- + e^+ \rightarrow \gamma + \gamma \tag{1.1}$$

When irradiating a tumoural region, the beam will interact with the different materials of the tissue and several reactions will occur, generating different positron emitters. Each of the emitters will contribute differently to the total PET signal, and the final image will have a combination of them all. Table 1.1 presents the half lives and reaction channel of the major beta emitters, generated during PT. As each positron emitter has a different decay time, the PET images obtained for range verification are time sensitive. At the beginning of the acquisition most of the contribution will be produced from radioisotopes with shorter half lives, and once these have disintegrated, the elements with longer half lives will be the main contribution [12]. The accuracy of PET is limited by biological washout, this is the loss and delocalisation of signal due to several metabolic decay processes [13; 14].

Nowadays there are three modalities for PET verification depending on when the acquisition begins: in-beam PET, in-room PET and off-line PET. Each modality has its advantages and disadvantages in terms of acquisition time, data quality and cost effectiveness [15].

In-beam PET uses a detection system integrated in the delivery system, so its main advantage is that the delay between the irradiation and PET acquisition is minimised. The acquisition can start immediately, if the treatment takes place in a cyclotron based facility. For synchrotron based facilities, as a pulsed beam is delivered, the data can be collected during the pauses of beam delivery and continued after the treatment, if required [15]. In both cases the effect of biological washout will be negligible, and the activity level in the tissue will be

high for all, long and short half live isotopes. This modality also minimises the errors derived from patient repositioning, as well as anatomical and morphological changes. However, the integration of a dedicated PET system into the beam delivery system is technically demanding and more expensive [16].

In-room PET will start once the irradiation has stopped and uses an independent detection system that is in the irradiation room, reducing the cost. Simultaneously, there is no need to reposition the patient, and the biological washout is reduced significantly because the time elapsed between the irradiation and the detection is brief. Isotopes with short half lives, like ^{15}O, will not be detected, so the images will be obtained from longer living isotopes. The technical limitation is reduced, but a PET/CT scanner is preferred in order to correlate the images of the treatment and PET images [17; 18].

Radionuclide	**$T_{1/2}$ (min)**	**Reaction channel**
^{11}C	20.385	^{12}C(p,pn) ^{11}C ^{14}N(p,2p2n) ^{11}C ^{16}O(p,3p3n) ^{11}C
^{13}N	9.965	^{16}O(p,2p2n) ^{13}N ^{14}N(p,pn) ^{13}N
^{15}O	2.037	^{16}O(p,pn) ^{15}O
^{30}P	2.498	^{31}P(p,pn) ^{30}P
^{38}K	7.636	^{40}Ca(p,2p2n) ^{38}K

Table 1.1: Major radionuclides, associated half lives and nuclear reaction channels for proton induced positron emitter productions [15].

Off-line PET begins when the irradiation has stopped. It requires the transfer of the patient to a different room, which leads to a delay of approximately 15 to 30 minutes between the irradiation and the image acquisition [15]. This method eliminates the contributions of ^{15}O and ^{13}N, and the image will only be obtained from elements whose half-life is longer than the time it takes to transfer the patient, i.e. ^{11}C. The signal will decrease notoriously due to the decay, but also to the biological washout. Furthermore, patient set-up is performed separately for irradiation and imaging, which can lead to additional sources of uncertainty

when correlating the images [19]. The main advantage of this technique is that the price is significantly lower, as there is no need to install a new PET scanner.

1.2.2 Prompt gamma-ray methods

High energy prompt gamma rays (PG) are naturally emitted as a result of the interaction between the protons and the nuclei in the patient's tissue, and they were first proposed for range verification in 2006 [20]. The main advantage of PG compared to PET is that their emission time is just a few nanoseconds, so they are not affected by the biological washout.

Nuclear reactions occur along the whole penetration path, until the Bragg peak region, in which the energy reduces and protons stop. The emission of secondary radiation correlates with the proton range, through the energy dependence of the cross sections for gamma ray emission, because the PGs originate from the region in which the protons interact with the patient tissues.

Both, the energy and intensity of the gamma rays depend on the beam energy and the composition of the irradiated tissue. As different human tissues have different elemental composition, the gamma-ray spectrum will vary depending on the tumour location [21]. There are some elements that are common to most human tissues, so certain gamma rays will always be produced and can be used for monitoring the range of the protons. The energy of these gamma-rays, as well as their reaction channels are summarised in table 1.2 [22].

The majority of the gamma rays escape the human body, therefore their detection can be used for range verification purposes by placing a gamma-ray detector outside the human body. To quantify the range of the proton beam with prompt gamma-rays we must locate precisely their point of emission. There are two different methods: prompt gamma-ray imaging (PGI) and prompt gamma-ray non-imaging (PGNI), and both of them are described in the following subsections.

1.2.2.1 Prompt gamma-ray imaging (PGI)

Prompt gamma-ray imaging (PGI) is a non-invasive range/dose verification method that measures the PGs emitted during the treatment. Since PGs are only emitted during the

irradiation, the feasibility of using them for range verification depends on the design of highly efficient detectors [23].

PG radiation has an energy of few MeV (from 1-2 MeV up to 7 MeV), so it requires detectors capable of operating efficiently at higher energy range than those traditionally used for PET. This method requires a collimated detection system to stop the gamma-rays that are travelling towards the detector but are not perpendicular, in order to reduce their contribution and reconstruct accurately the spatial origin of the gamma emission [20].

1.2.2.2 Prompt gamma-ray non imaging

To reduce the cost and complexity of both the detection systems and the image reconstruction in PET and PGI, non-imaging techniques that use PGs has been proposed and tested by several groups [24–26]. The two main non-imaging methods are prompt gamma-ray timing (PGT) and prompt gamma-ray spectroscopy (PGS).

PGT is a novel technique that evaluates the time distribution of PG generated by a bunched beam, measured with an uncollimated detector with respect to a bunch timing reference. Protons have a finite transit time of about 1-2 ns until they stop 5-20 cm inside the target volume [24]. The width and position of the timing distribution reflect the stopping or transit time of particles in tissue, and this is a direct measurement of the particle's range in that tissue [25].

Target	**Reaction channel**	**Energy (MeV)**
^{12}C	^{12}C(p,pn) ^{11}C*	2.0
	^{12}C(p,p') ^{12}C*	4.44
^{16}O	^{16}O(p,p') ^{16}O*	6.13
	^{16}O(p,pα) ^{12}C*	4.44
	^{16}O(p,pn) ^{15}O*	5.24
	^{16}O(p,2p) ^{15}N*	5.27
^{14}N	^{14}N(p,p') ^{14}N*	1.64, 2.13
^{40}Ca	^{40}Ca(p,p') ^{40}Ca*	3.73

Table 1.2: Proton-induced reaction channel and energies of the main gamma-rays in human tissues [22].

PGS uses both, the arrival time and energy of the detected PGs. The range of the protons can be verified using complex nuclear models, without requiring prior knowledge of the elemental composition of the irradiated matter [27]. Additionally, the measurement of the arrival time of the gamma rays allows a separation of proton and neutron induced gamma rays, which removes background [26].

1.3 Nanoparticles in radiotherapy

The use of nanoparticles (NPs) with high atomic numbers has been proven clinically effective. NPs enhance the radiation effects due to their potential to release electrons into a nanoscale volume, amplifying radiation-induced biological damage in their vicinity and increasing the dose delivered to the tumour [28]. Due to their small size, NPs have the ability to travel through the human body without extravasating out of blood vessels in healthy tissues, allowing them to reach the tumoural region [29]. Simultaneously, they tend to accumulate in the tumoural region according to the enhanced permeability and retention effect (EPR) [30].

The increase of the dose in cancer treatments when nanoparticles are inside the tumoural region can be quantified with the dose enhancement factor (DEF). The amplification of radiation effects with high-Z nanoparticles as radio-enhancers was first demonstrated with gold nanoparticles (AuNP) [31]. Several studies have been carried out to determine which high atomic number NPs are appropriate for proton therapy. NPs of platinum, gadolinium [32], iodine, silver, iron oxides [33] or barium sulfate ($BaSO_4$) can be used as dose-enhancers in proton therapy treatments [34; 35]. All of these nanoparticles have common characteristics, such as high atomic number, high uptake, non-toxicity and stability. For clinical applications, inexpensive biocompatible particles with high atomic numbers are desired.

1.4 Motivation

1.4.1 Challenges

Proton therapy is a promising treatment for cancer that offers a better conformational dose than conventional therapy, but due to the uncertainties its applicability is limited. Several verification techniques have been studied to determine the range precisely, but there is a

necessity for real time range verification methods.

Currently, PET is the most studied technique with off-line PET range verification methods being applied clinically. Despite the progress in this field in the past few years, the method remains expensive and the absence of dedicated detection systems is challenging. Furthermore, the effect of biological washout limits the accuracy of this method.

The use of PGs for range verification is not affected by biological washout, as the emission is almost instantaneous. The main challenge for PG is the lack of a cost-effective detector that allows online beam monitoring during the clinical irradiation.

Nanoparticles have been proven to amplify the radiation effect in the vicinity of the tumour, but so far there have not been studies on the PG emission generated after the irradiation of these radiomarkers.

1.4.2 Aim and objectives

In this project we focus on reducing the uncertainties in proton therapy by applying a novel idea: combining two established techniques used in PT treatments; the use of PGI for range verification with characteristic gamma-rays from a NPs target material which has been proven as a dose enhancer.

To demonstrate the proof of principle, a simple detection system was developed, characterised and tested to study real-time PG profile. The detection system combines two different types of crystals, a monolithic inorganic scintillator of $Cs_2LiLaBr_6(Ce)$ (CLLB) and a high-purity germanium detector (HPGe) to study and compare the response of both materials through in-beam measurements. The configuration and characterisation of the detectors is introduced in chapter 3.

Different concentration magnetite (Fe_3O_4) targets have been created to study their effect on proton therapy, not only as dose enhancers but also as emitters of characteristic PGs that can be detected to determine the range of the proton beam.

The aim of the project can be summarised as the combination of the two methods to develop a simple, low-cost and sensitive prototype that allows real time monitoring of the range while increasing the dose in the tumoural region.

Chapter 2

Theory

The fundamental physics in proton therapy and radiation detection is presented in this chapter. Firstly, the interaction mechanisms of charged particles with matter are presented: electromagnetic (EM) and nuclear interactions. While EM process govern the continuous energy loss of protons, nuclear interactions are responsible for the emission of secondary particles. The emission of secondary PGs correlates with the proton range through the gamma-ray production cross section as a function of the proton energy, and therefore their different interaction mechanisms are discussed. Finally, the principles of radiation detection with scintillator detectors and semiconductors are introduced, including the data acquisition (DAQ) systems, from electronics readout to pulse processing.

2.1 Proton interaction with matter

Radiotherapy protons have a kinetic energy of up to 300 MeV and they interact with matter via electromagnetic (EM) and nuclear interactions. During these interactions, secondary particles such as gamma-rays and neutrons are produced.

EM interactions are responsible for the energy loss of the protons, and these protons will eventually stop because of the EM collisions with the atomic electrons, in a process called stopping. EM interactions can also deflect the protons by a few degrees, this occurs when they collide with atomic nuclei in a process called multiple Coulomb scattering (MCS) [36]. However, nuclear interactions are hard scatters either by the nucleus or by its constituents. The three possible proton interaction mechanisms are illustrated in figure 2.1.

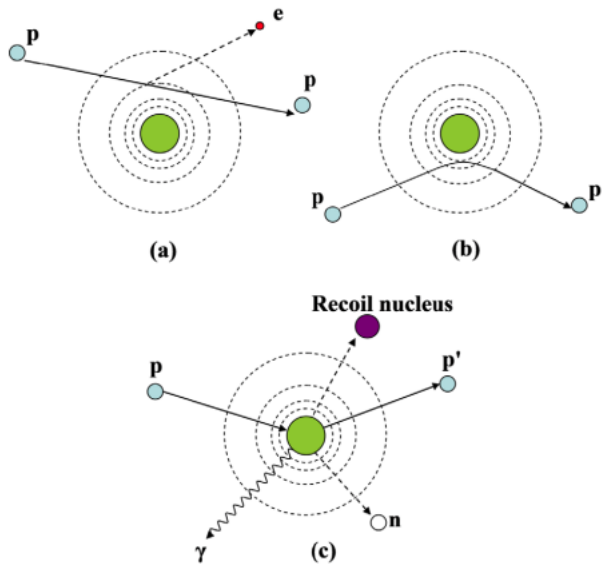

Figure 2.1: Schematic illustration of proton interaction mechanisms: (a) energy loss via inelastic Coulombic interactions, (b) deflection of proton trajectory by Coulomb elastic scattering with the nucleus, (c) nuclear interaction and production of secondary particles [37].

2.1.1 Electromagnetic interactions

Protons primarily lose their energy through EM interactions with atomic electrons during inelastic collisions. The energy loss of the projectile is continuous, and will determine the range of the beam in the patient. The expected value of the rate of energy loss per unit of path length (dE/dx) is defined as the Stopping Power (S). However, it is preferred to define the energy loss independent of the mass density of the absorbing material, hence the **Mass Stopping Power** (S/ρ), in which ρ is the material density, is more often used, and is defined in equation 2.1.

$$\frac{S}{\rho} = -\frac{dE}{\rho\ dx} \tag{2.1}$$

The energy loss of protons is described by the **Bethe-Bloch formula** (equation 2.2) where N_A is Avogadro's number, r_c is the classical Bohr radius, m_e is the mass of an electron, Z is the atomic number of the target, z is the charge of the projectile, A is the atomic weight of the target material, C is the shell correction item, δ is the density correction, $\beta = v/c$ is the ratio of the velocity of the particle (v) to the speed of light (c), and I represents the average excitation energy of the material [38].

Equation 2.2 implies that the energy loss for a given projectile charge is proportional to the inverse square of the velocity of the projectile (i.e. $1/\beta^2$). This dependence implies that the energy deposition is maximum at the end of the particle's path, when the speed of the particles is minimum.

$$-\frac{dE}{dx} = 4\pi N_A r_c^2 m_e c^2 \frac{Z}{A}\frac{z^2}{\beta^2}\left[ln\frac{2m_e c^2\gamma^2\beta^2}{I} - \beta^2 - \frac{\delta}{2} - \frac{C}{Z}\right] \tag{2.2}$$

The average path length travelled by a charged particle until it is at rest is defined as the **range** (R), and can be calculated from the stopping power as shown in equation 2.3. In 1905 Bragg and Kleeman discovered that the relationship between the logarithm of the range and logarithm of the initial energy of the proton beam (E) is almost linear, so the range follows a power law and can be calculated with the Bragg-Kleeman rule, as shown in equation 2.4 where α is a material-dependent constant and the exponent p depends on the proton beam energy [39].

$$R(E) = \int_0^E \left(\frac{dE'}{dx}\right)^{-1} dE' \tag{2.3}$$

$$R(E) = aE^p \tag{2.4}$$

The energy loss is a statistical process, and therefore there are small variations in the energy loss of individual protons. As a consequence, there will be a spread of ranges due to an effect called **range straggling**, that results in a broadening of the BP [40]. Three different theories have been developed to calculate the range straggling based on the thickness of the absorber: for thick absorbers Bohr's theory is established [41], for intermediate absorbers Landau's theory is applied [42] and if the absorber is thin, Vavilov theory must to be considered [43]. For this project only Bohr's theory is applicable due to the thickness of the target materials, therefore Landau and Vavilov theories will not be discussed further.

Bohr's theory states that the range straggling behaves according to a Gaussian probability density function (PDF), and its sigma (σ_Δ) can be estimated as a function of the proton beam range, as shown in equation 2.5 [44]. In this equation R_0 is the range in water for a mono-energetic proton beam (in centimeters), k is a material-independent constant, equal to 0.012 for protons [45], and m is empirically determined [37; 44].

$$\sigma_\Delta \approx kR_0^m \tag{2.5}$$

For this reason, the range is an average quantity, defined for a beam energy and not for individual particles, and in proton therapy the **Mean Projected Range** (R_0) is used [6; 37]. The mean projected range corresponds to the required thickness of a material to stop half of the incident protons when nuclear interactions are not taken into account. It is defined as the depth in water in which the dose is 80% of the total dose (d_{80}), as shown in equation 2.6.

$$R_0 = d_{80} \tag{2.6}$$

In the second type of EM interactions, **MCS**, an elastic collision between the atomic nuclei and the projectile occurs. The proton trajectory is altered due to the force created by the nuclei, as shown in figure 2.1(b), but the scattering angle does not affect the range of the proton beam. Hard scatters are relatively infrequent, and only 20% of the protons in the beam suffer a hard scatter before stopping. MCS is responsible for the scattering of the beam in the transverse plane, resulting in a deviation in the primary path, which increases with the proton energy. This produces a lateral broadening of the beam, and its deflection by scattering is characterised by the scattering power (T), defined as a function of the mean squared scattering angle (θ) and the thickness of the absorber through which the proton travelled (x), as in equation 2.7 [37].

$$T = \frac{d < \theta^2 >}{dx} \tag{2.7}$$

In PT the MCS effect is studied as a net combination of all the scattering events, instead of individually studying many small-angle scattering events [37]. The theoretical calculations of MCS are quite complex, and as they do not affect the range of the proton beam they are not considered in this thesis. However, it is important to note that the MCS angular distribution in PT is often considered to follow the form of a Gaussian distribution, given by equation 2.8 where $< \theta^2 >^{\frac{1}{2}}$ is the root mean square scattering angle [46].

$$P(\theta) \approx \frac{2\theta}{< \theta^2 >} exp\left(\frac{-\theta^2}{< \theta^2 >}\right) d\theta \tag{2.8}$$

2.1.2 Nuclear interactions

Nuclear interactions are harder to model, but their biological effect is small. There are two types of nuclear reactions: elastic and non-elastic. In elastic nuclear reactions the total kinetic energy is conserved, while in nonelastic reactions the kinetic energy is not conserved. Inelastic reactions are a specific type of nonelastic reactions in which the final nucleus is the same as the bombarded nucleus. Particles created from inelastic or nonelastic nuclear reactions are called secondaries. Nuclear reactions inside the patient provide a non-invasive approach to measure the proton beam range, by detecting the secondary gamma-rays from proton-induced nuclear reactions [37].

The main effect of nuclear reactions in proton therapy is a small decrease in absorbed dose due to the removal of primary protons, which is compensated by the liberation of other protons and ions [6]. Secondary protons increase the dose build-up due to the generation of secondary particles from nuclear interactions. They also are the main contributors to the dose, as they can deliver up to 10% of the total dose [47]. However, several studies show that the absorbed dose contribution from secondary particles is approximately 1% of the primary proton dose [48; 49].

In clinical PT, the two nuclear interactions that dominate gamma-ray emission are proton-induced reactions on ^{16}O, as this nuclei is the most abundant in the human body by volume. The first reaction, shown in equation 2.9, corresponds to the decay of the first excited level of ^{12}C, produced after the proton irradiation of ^{16}O, and emitts a PG of 4.44 MeV. The second reaction, shown in equation 2.10, corresponds to the inelastic scattering of ^{16}O that emitts a PG of 6.13 MeV.

$$^{16}\mathrm{O(p,p}\alpha)^{12}\mathrm{C}^{*} \tag{2.9}$$

$$^{16}\mathrm{O(p,p')}^{16}\mathrm{O}^{*} \tag{2.10}$$

The probability of a nuclear interaction to occur is measured by the **cross section** (σ), that has units of barn (1 barn = 10^{-28} m^2). The total cross section is obtained as the sum of the cross sections for each of the individual processes. The cross section for the reactions given by equations 2.9 and 2.10 can be seen in figure 2.2, where we observe that the highest interaction probability occurs at 25 MeV for the 4.44 MeV gamma ray, while for the 6.13 MeV gamma ray the cross section peaks around 12 MeV.

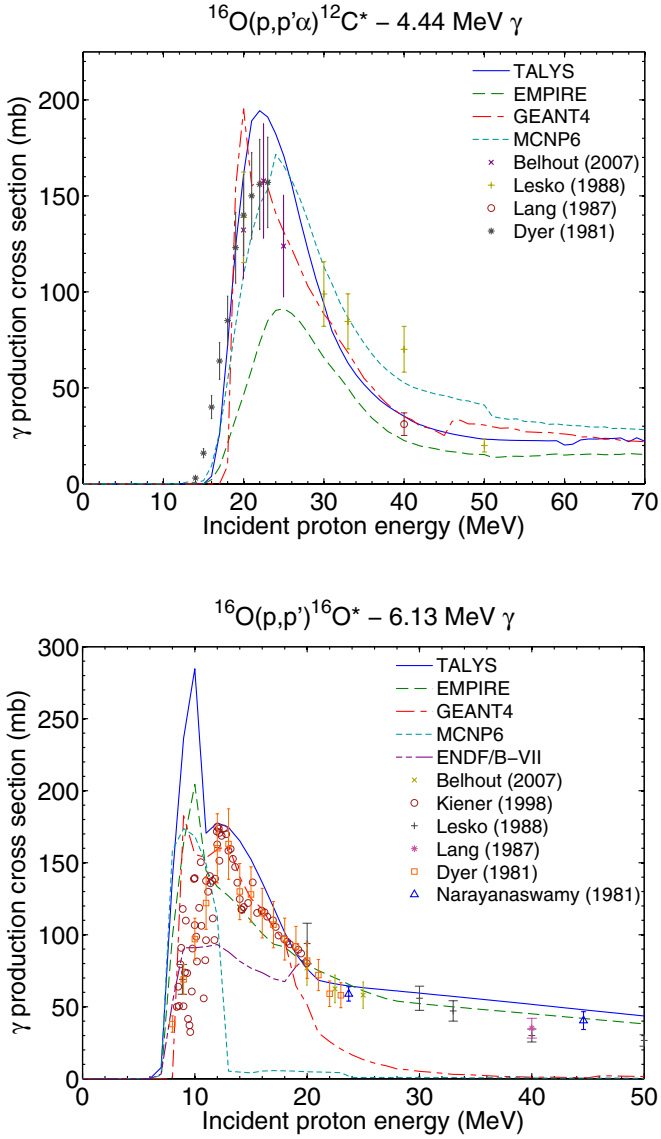

Figure 2.2: Cross-section of 4.44 and 6.13 MeV gamma ray emission due to proton-induced reactions on ^{16}O [50].

In this work, the cross sections from proton-irradiation of iron are also relevant, as the target is an iron-rich compound. Several reactions may occur after the proton-irradiation of ^{56}Fe, and their gamma production cross section for different proton energies can be seen on figure 2.3. We will focus on the three dominant reactions, described in equations 2.11-2.13. For two of these reactions, the inelastic scattering of ^{56}Fe and the production of ^{56}Co, the cross section peaks at around 14 MeV, while for the third reaction, that corresponds to the production of ^{55}Fe, the cross section reaches a maximum value at 24 MeV.

$$^{56}\text{Fe(p,p')}^{56}\text{Fe} \tag{2.11}$$

$$^{56}\text{Fe(p,n)}^{56}\text{Co} \tag{2.12}$$

$$^{56}\text{Fe(p,pn)}^{55}\text{Fe} \tag{2.13}$$

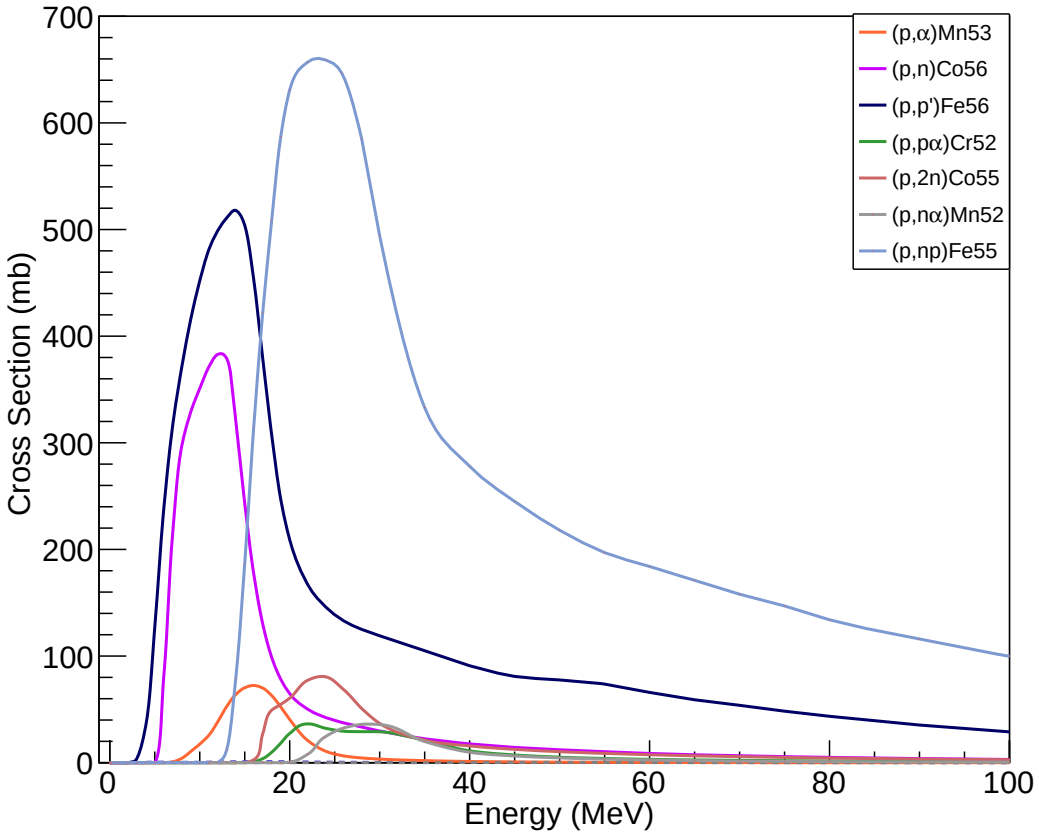

Figure 2.3: Cross-section for different nuclei produced via proton irradiation of ^{56}Fe. Data obtained from nuclear data library *TENDL-2019* [51].

2.2 Neutral particle interaction in matter

Neutral particles do not lose energy continually via the same mechanisms that protons do. Therefore, their interactions mechanisms are different and will be explained in this section. In PT, two types of uncharged particles are most often produced as secondaries: gamma-rays and neutrons.

2.2.1 Gamma-ray interaction

Gamma-rays are EM waves that have the smallest wavelengths of any wave in the electromagnetic spectrum. They are also the most energetic, as the energy (E) and wavelength (λ) are related by the **Planck-Einstein relation** (eq. 2.14), in which h represents the Planck constant, ν the frequency of the photon and c is the speed of light [52].

$$E = h\nu = \frac{hc}{\lambda} \tag{2.14}$$

Gamma-rays, in the range of a few keV to several MeV, interact with matter via three main processes: photo-electric effect, Compton scattering and pair production. The probabilities of each of these interactions occurring are characterised by their individual attenuation coefficients ($\tau_{photoelectric}$, $\sigma_{Compton}$ and κ_{pair}). The attenuation of the photon beam intensity (I) is given by equation 2.15, where I_0 is the initial photon intensity, μ is the total linear attenuation coefficient (in cm^{-1}) defined as the sum of the individual attenuation coefficients, as shown in equation 2.16, and x is the thickness of the absorber in cm.

$$I = I_0 e^{-\mu x} \tag{2.15}$$

$$\mu = \tau_{photoelectric} + \sigma_{Compton} + \kappa_{pair} \tag{2.16}$$

The **photoelectric effect** is an absorption process in which a photon interacts with an absorber atom and disappears, ejecting a photoelectron in the process. The energy of the photoelectron is given by equation 2.17, where E_b represents the binding energy of the photoelectron in its original shell [53].

$$E_{e^-} = h\nu - E_b \tag{2.17}$$

The probability of photoelectric absorption per atom is approximately calculated as a function of the energy (E_γ) and the atomic number (Z), where n varies between 4 and 5 depending on the energy of the gamma ray [54]. The photoelectric effect is the dominant mechanism for low energy gammas interacting in absorber materials of high atomic number Z, as shown in figure 2.4.

$$\tau_{photoelectric} \approx constant \cdot \frac{Z^n}{E_\gamma^{3.5}} \tag{2.18}$$

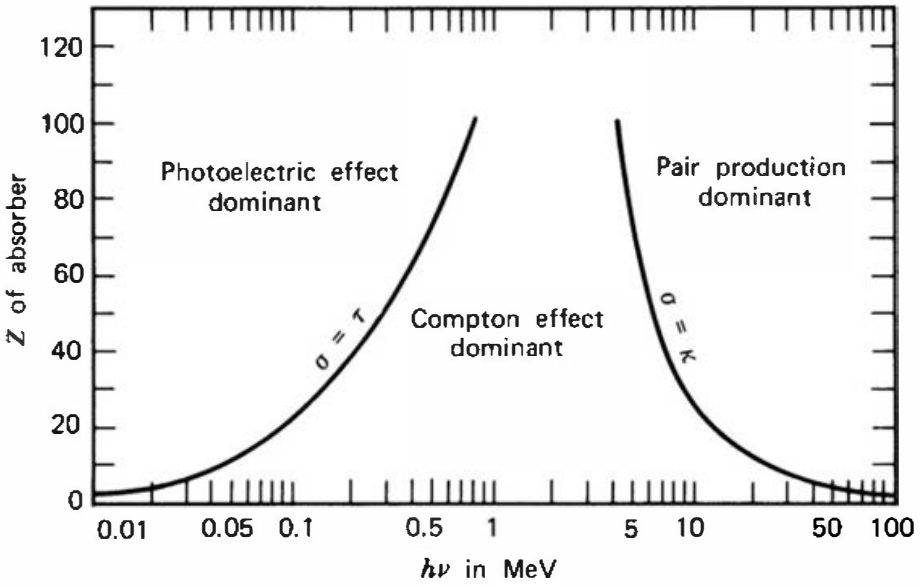

Figure 2.4: Relative importance of the three types of gamma-ray interactions with matter for different initial energies and atomic number of the absorber [55].

The second process of attenuation of gammas is **Compton scattering**, and it dominates for gamma rays with energies between 0.1 and 10 MeV. In this process the gamma ray interacts with an orbital electron, transferring only a fraction of its energy to said electron, that is known as a recoil electron [53]. The actual energy transfer depends on the scattering angle (θ) of the gamma, that is calculated with the Compton scattering formula (equation 2.19), where m_0c^2 is the rest-mass energy of the electron (511 keV), $h\nu$ is the incident gamma-ray energy and $h\nu'$ is the scattered gamma-ray energy.

$$h\nu' = \frac{h\nu}{1 + \frac{h\nu}{m_0c^2}(1 - cos\theta)} \tag{2.19}$$

The probability of Compton scattering per atom of the absorber depends on the number of electrons available as scattering targets, hence it increases linearly with Z, as shown in equation 2.20 [53]. The angular distribution of scattered gamma-rays can be predicted with the Klein-Nishina formula for the differential scattering cross section (equation 2.21), where r_0 is the classical electron radius and $\alpha = h\nu/m_0c^2$ [56].

$$\sigma_{Compton} \approx constant \cdot Z \tag{2.20}$$

$$\frac{d\sigma}{d\Omega} = Zr_0^2 \left(\frac{1}{1+\alpha(1-cos\theta)} \right)^2 \left(\frac{1+cos^2\theta}{2} \right) \left(1 + \frac{\alpha^2(1-cos\theta)^2}{(1+cos^2\theta)[1+\alpha(1-cos\theta)]} \right) \tag{2.21}$$

At higher energy levels, the **pair production** mechanism dominates. When a high energy gamma ray passes close enough to a heavy nucleus, the gamma ray completely disappears, and an electron and a positron are formed. For this reaction to take place, the original gamma must have an energy of at least 1.022 MeV, the sum of the product particle rest masses. Any energy greater than 1.022 MeV becomes kinetic energy shared between the electron and positron, as shown in equation 2.22.

$$E_{e^-} + E_{e^+} = h\nu - 1.022 \text{ MeV} \tag{2.22}$$

The probability of pair production increases significantly for higher energy gammas, as shown in figure 2.4. No simple expression exists for the probability of pair production per nucleus, but its magnitude varies approximately as the square of the absorber atomic number [53; 54].

2.2.2 Neutron interaction

Neutrons have no electrical charge and have a high penetrating power, and they mainly interact with the nucleus. Neutrons can be attenuated by three major interactions: elastic scattering, inelastic scattering, and absorption. Neutron energy drastically affects the probabilities of different types of interactions occurring, so it is convenient to divide neutrons intro three categories: thermal neutrons, with energies below 0.5 eV, intermediate-energy neutrons between 0.5 eV and 10 keV, and fast neutrons with energies higher than 10 keV [57].

In **neutron elastic scattering** the total kinetic energy is conserved: a neutron collides with a nucleus losing part of its kinetic energy, that is absorbed by the recoil nucleus. This

mechanism is responsible for slowing down fast neutrons to thermal neutrons. The energy gained by the nucleus (E_A) is defined as a function of its atomic mass (A), the neutron energy (E_n) and the angle of the collision (θ), as shown in equation 2.23 [58]. The smaller the difference in mass of the neutron and the nucleus, the more effective the slowing down of the neutron will be, as the amount of energy transferred will be maximum. Therefore, targets with lower atomic mass number are more effective as a moderators. For this reason, hydrogenous materials are used for neutron attenuation [59].

$$E_A = E_n \left[\frac{4A}{(A+1)^2} \right] cos^2\theta \tag{2.23}$$

When neutrons undergo **inelastic scattering**, part of the energy of the neutron is transferred to the nucleus, that will remain in an excited state. In order to return to its ground state gamma-rays are emitted. These gamma-rays can not be used for range verification purposes, as they are not emitted due to the proton interaction, and therefore shielding techniques need to be implemented during range verification experiments with PGs to reduce their contribution. However, the importance of neutron scattering becomes important because the neutron can transfer an appreciable amount of energy in one collision, so fast neutrons induce substantial background noise in the detection of PG signals.

The third interaction mechanism is the **radiative capture** that occurs when the neutron is captured by the nucleus. The neutron is completely absorbed, and a compound nucleus is formed. The compound nucleus needs to decay to its ground state by emitting one or more gamma rays. This occurs at most neutron energy levels, but is more probable at lower energy levels. The radiative capture reaction (n,γ) can have a substantial contribution to background in PGI, and to reduce its effect elements with high capture cross sections for thermal neutron, such as Boron, Cadmium or Gadolinium are used [60].

2.3 Dose enhancement with nanoparticles

Radiation sensitisation is the process of enhancing the susceptibility of tumoural tissues to radiation exposure [61]. **Radiosensitizers** are therapeutic agents that enhance the effects of radiation therapy, i.e the cell killing from irradiation in tumour cells [62; 63]. The resistance

of tumour cells to radiation therapy has lead to the study of new radiosensitizers, and over the last few years, NPs have been proposed to enhance the radio-therapeutic effect. This technique is designed to overcome radio therapy limitations, by enhancing the dose received in the tumour.

NPs have the ability to travel through the human body because, due to their size, they cannot extravasate out of blood vessels in healthy tissues, which allows them to reach their final destination [64]. Simultaneously, they tend to accumulate in the tumoural tissue, according to the **enhanced permeability and retention effect** (EPR) [30; 65]. The EPR effect relies on specific physiopathological characteristics of tumoural tissues: the abnormally wide fenestrations in the blood vessels allows for the extravasation of materials with sizes up to several hundreds of nanometers [29]. Together with the absence of lymphatic drainage, leads to a relatively effective and selective accumulation of nanoparticles in tumours [66]. The EPR effect has been accepted as a universal pathophysiological characteristic of solid tumours [67], and the detailed characteristic mechanisms are not discussed here, since they are not relevant to this work.

The benefits of using NPs in cancer treatment can be quantified with the **dose enhancement factor (DEF)**, defined as the ratio of the dose with nanoparticles over the dose without it, as shown in equation 2.24.

$$\text{Dose enhancement factor} \rightarrow DEF = \frac{\text{Dose with NP}}{\text{Dose without NPs}} > 1 \tag{2.24}$$

In PT, the energy loss of protons is directly proportional to the atomic number of the media (Z). Due to this dependence, particles with high atomic number amplify the radiation-induced biological damage. The amplification of radiation effects with high-Z nanoparticles as radio-enhancers was first demonstrated with gold nanoparticles (AuNPs) [31].

AuNPs are the most studied nanoparticles for dose enhancement, due to their low toxicity, high stability and high biocompatibility [68; 69]. However, it has been proved that the dose enhancement effect generated by AuNPs in proton therapy is smaller than in photon therapy, because while photons can produce photoelectrons with a long range, protons produce short-range secondary electrons from the collisions with AuNPs and thus, cannot generate dose enhancement on larger scales [70]. For this reason several studies have been carried out to determine which high atomic number NPs are most suitable for proton therapy. It has been

proven that nanoparticles of platinum, iodine, gadolinium, silver, iron oxides or barium sulfate ($BaSO_4$) can be used as dose-enhancers for proton therapy treatments [32–35]. All of these nanoparticles have common desired characteristics for clinical application: biocompatibility, high atomic number, high uptake, non-toxicity, stability and a lower price.

The combination of nanoparticles with external beam radiotherapy has already been evaluated in clinical trials, showing improvements in efficacy and in tolerability while enhancing the dose in the tumoural region [29; 71].

2.4 Gamma-ray detection with scintillators

A scintillator is a material that exhibits luminescence when excited by ionising radiation. Luminescent materials absorb the kinetic energy of ionising radiation and then they scintillate, i.e re-emit part of the absorbed energy as light. Scintillator detectors must be then coupled to light sensors in order to convert the light into an electrical pulse. The light sensors can be, for example, photomultiplier tubes or photodiodes.

2.4.1 Scintillator materials

Scintillating materials are classified in two categories: organic and inorganic crystals. The classification is based on the main components of the material. While organic scintillators are mostly composed of Carbon (C), Hydrogen (H) and Oxygen (O), inorganic scintillators are made of other elements, and are primarily ionic solids and composed of high-density crystals, such as CsI or NaI [72]. The scintillation mechanism is different for different types of scintillator crystals.

In **organic scintillators**, the scintillation mechanism called fluorescence arises from transitions in the energy level structure of a single molecule [53]. The singlet energy levels (spin = 0) are labelled as S_0, S_1, S_2 and S_3. The energy spacing between the ground state (S_0) and the first excited state (S_1) is around 3 to 4 eV, while the spacing between higher states is smaller, as shown in figure 2.5. Higher singlet electronic excited states are quickly de-excited to level S_{10} via internal conversion without emitting any radiation [73]. Then they decay to the ground state, emitting scintillation light in a process known as prompt fluorescence that has a time scale of nanoseconds (10^{-8} s). The triplet energy levels (spin = 1) are labelled as

T_1, T_2 and T_3. Molecules from the first triplet decay to singlet ground states via phosphorescence, that emits light with a longer emission time (μs to hours depending on the material) and different wavelength spectrum than the fluorescence. A transition called inter-system crossing transforms singlet states in level S_1 to the first triplet (T_1). Some molecules may be thermally excited back to the S_1 state, and decay through fluorescence in a delayed process called delayed fluorescence that emits the same spectrum as fluorescence, but with longer emission times [73].

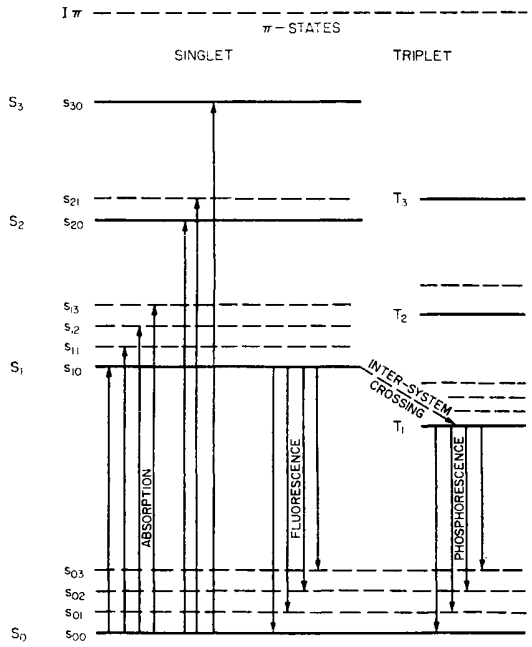

Figure 2.5: Electronic energy levels of an organic molecule with singlet and triplet excited states. The de-excitation of these states (fluorescence and phosphoresence) causes the prompt and delayed scintillation light [73].

Inorganic crystals, however, have a different scintillation mechanism, that depends on the structure of the crystal lattice. In a pure inorganic crystal electrons are only allowed to occupy selected energy bands. In pure crystals, n electrons can elevate from the valence band to the conduction band after the absorption of energy, leaving a gap in the valence band. However, the return of an electron to the valence band with the emission of a photon is an inefficient process. Therefore, to overcome the limitations, small amounts of impurities are added to the crystal. The impurities, called activators, create special sites in the lattice at which the band gap structure is modified. The electron can de-excite through these levels back to the valence band [74].

The energy levels created by the activator's presence within the crystal are narrower than in the pure crystal, as shown in figure 2.6. The photons emitted by the transition will be lower in energy than in the pure crystal: the emission spectrum is shifted to longer wavelengths and is not absorbed by the bulk material of the crystal.

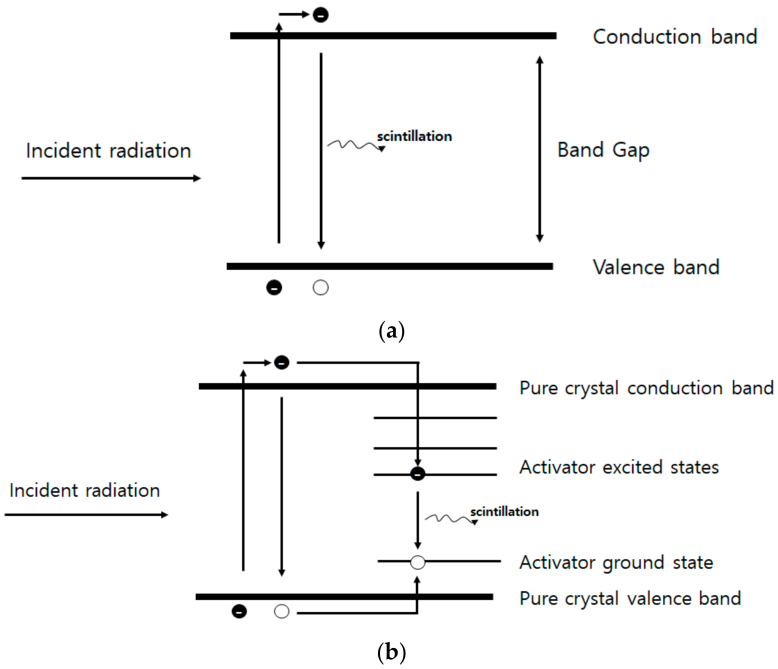

Figure 2.6: Energy band structure of an inorganic scintillator: (a) Pure crystal (b) Activated scintillator [74].

2.4.2 Photosensors

Photosensors couple to scintillators to convert the light emitted by the scintillating material into an electrical pulse. There are two main types of photosensors: photomultiplier tubes and photodiodes.

Photomultiplier tubes (PMT) are the most commonly used photosensors, since they have high amplification. They consist of a photocathode and some dynodes. The photocathode is made of a material in which the valence electrons are weakly bound and have a high cross section for converting photons to electrons via the photoelectric effect. Once the light created in the scintillator strikes the photocathode of the PMT, it releases photoelectrons.

The photoelectrons are internally amplified through dynodes with different voltages. Each subsequent dynode releases further electrons, so there is a current amplifying effect at each dynode [75]. At the final dynode, sufficient electrons are available to produce a pulse, that carries information about the energy of the radiation, of sufficient magnitude for further amplification. The sensitivity of a photocathode is quoted in terms of the quantum efficiency (QE), that is the probability for the conversion of incident photons to an electrical signal, and is defined as equation 2.25. The common value of QE for photocathodes is established between 20% and 30%, but it can increase up to 40% [53].

$$QE = \frac{\text{number of photoelectrons emitted}}{\text{number of incident photons}} \tag{2.25}$$

On the other hand, **photodiodes** (PD) are a semiconductor p-n junction that convert the light into an electrical signal by converting one photon into one electron-hole pair. Photodiodes have high quantum efficiency, lower power consumption and a compact size [76]. However, electronic noise is a problem due to the small signal amplitude.

Photodiodes can be manufactured from a variety of materials. With the advances in semiconductor materials, new types of photomultipliers have been created. The most widely used are silicon photomultipliers (SiPM), that consists of an array of photosensitive microcells, called single-photon avalanche photodiodes (SPAD). SPADs generate electron-hole pairs when a photon hits them. These pairs are then accelerated under the influence of a strong electric field and fast moving electrons produce an avalanche of secondary electrons, causing a measurable photocurrent [77]. Each SPAD operates in Geiger mode and several thousand microcell SPADs are needed to count the photons from scintillation.

Overall, PMT and SiPMs provide a fast response, with PMT having a higher gain factor and a smaller dark current. SiPMs are more compact and can operate in strong magnetic fields and environmental extremes however they have a relatively small dynamic range due to the finite number of SPADs in each of them. This causes saturation and introduces a non-linear response for high energy gamma-rays detection while PMTs have wider dynamic range, and therefore a better linear response for high energy gamma-rays.

2.5 Gamma-ray detection with semiconductor detectors

Semiconductor detectors are made of solid materials, and they are commonly used when the best energy resolution is required. Their better energy resolution often outweighs their disadvantages of small size and high cost in applications in which energy resolution is critical, because they allow the distinction of γ-rays differing by few keV only.

The two main materials used in semiconductor detectors are silicon and germanium. The probability of photoelectron absorption of gamma-rays varies as $Z^{4.5}$, so germanium detectors, with Z=32, are more suitable for this purpose that silicon detectors (Z=14) because the probability for an incident gamma-ray to deposit all its energy is larger in germanium. Also, silicon detectors cannot have a thickness of more than a few millimetres, while germanium-based detectors could reach thicknesses of several centimetres, and therefore can be used as a total absorption detector for gamma rays up to a few MeV. For these reasons, germanium detectors are widely used for gamma-ray spectroscopy, and their characteristics are detailed in subsection 2.5.1.

In semiconductor detectors, the charge carriers are electron-hole pairs, which are produced along the path of the particle through the detector [78]. The creation of electron-hole pairs is due to the energy lost by ionising radiation. The probability per unit time that an electron-hole pair is thermally generated is given as a function of the absolute temperature (T), the bandgap energy (E_g), the Boltzmann constant (k) and the proportional constant characteristic of the material (C) as equation 2.26 shows.

$$p(T) = CT^{3/2} exp\left(-\frac{E_g}{2kT}\right) \tag{2.26}$$

Thermal excitation in semiconductor materials is strongly dependent on temperature. At absolute zero every semiconductor is an insulator, and as the temperature increases the electrons are thermally excited from the valence band to the conduction band. Detectors should not have current in the absence of radiation, and for this reason some semiconductor detectors, such as HPGe, require cooling with liquid nitrogen (77 K), as cooling reduces the number of electron-hole pairs thermally created [79].

The average energy (ϵ) necessary to create an electron-hole pair in a given semiconductor at a certain temperature depends only on the detector material. A comparison of these values for germanium and silicon at liquid nitrogen temperature (77 K) and room temperature (300 K) is shown in table 2.1.

Material	**Temperature (K))**	ϵ **(eV)**
Ge	77	2.96
Ge	300	-
Si	77	3.81
Si	300	3.62

Table 2.1: Average energies for electron-hole creation in germanium and silicon at different temperatures [80; 81].

2.5.1 Germanium detectors

Germanium detectors are semiconductors that are especially suitable for gamma-ray spectroscopy due to their excellent energy resolution, that allows the separation gamma rays close in energy, because of their relatively high density and high atomic number. Their operational principle is based on the production of electrons and holes after the gamma rays interact with the sensitive material of the detector. Then they are swept by the electric field to the p and n electrodes. This charge, proportional to the energy deposited in the detector, is converted into a voltage pulse by an integral charge-sensitive preamplifier [82].

Germanium detectors have a small band-gap, so room-temperature operation of these detectors is not possible as there will be a large thermally-induced leakage current. Therefore, they need liquid nitrogen to cool down. The detector must be kept in a vacuum-tight cryostat to suppress the thermal conductivity between the crystal and the surrounding air. The crystal is usually covered by a thin end window not to attenuate the gamma rays before they interact with the germanium crystal.

To account for deviations from pure Poisson statistics, the Fano factor (F) is introduced [83]. This factor is an adjustment, and is calculated with equation 2.27. This value varies between 0 and 1, and several experiments have determined that for HPGe detectors

the Fano factor is small, and has a value of approximately 0.1 [84; 85].

$$F = \frac{\text{observed statistical variance}}{E/\epsilon} \tag{2.27}$$

The FWHM of a gamma ray detected by a germanium detector can be calculated as shown in equation 2.28, where w_D is the peak width due to detector effects and w_E accounts for the broadening of the peak width due to electronics effects.

$$FWHM = \sqrt{w_D^2 + w_E^2} \tag{2.28}$$

While w_E is dependent on the detector capacitance, its bias voltage and readout electronics, w_D can be calculated as a function of the Fano factor (F), the energy necessary to create one electron-hole pair (ϵ) and the energy of the gamma-ray (E), as shown in equation 2.29. In the case of germanium, the value of ϵ is low ($\approx$ 3 eV) so a large number of electron-hole pairs are produced, which results in good statistics from the charge collection and therefore a good energy resolution [82].

$$w_D = 2\sqrt{(2ln2)F\epsilon E} \tag{2.29}$$

2.6 Electronics readout and pulse processing

Radiation detectors require pulse processing electronics to extract the information from the pulses produced by the detectors after the incident particles interact with them. There are two types of pulses: linear and logic. Linear pulses carry information through its amplitude and shape, while logic pulses carry information only with its presence. Usually, linear pulses are produced by the interactions and then converted to logical pulses.

There are two different ways of processing a signal: the traditional analog signal processing and the digital signal processing. The basic components of an **analog pulse processing** chain are shown in figure 2.7. Once the particles interact with the detector, their energy is converted into a current pulse. The total charge is too small so the current is sent to a preamplifier, a charge sensitive module, that integrates the pulse converting the current into a voltage step that is proportional to the charge (Q). Then, the shaping amplifier converts the signal into a form suitable for measurements, usually a semi-Gaussian pulse whose height corresponds to the output voltage (V_{peak}) and is proportional to the deposited charge. The

signal will then be digitised by the analog-to-digital converter (ADC) of a multi-channel analyser (MCA). The MCA will produce the energy distribution of the incident particles. Simultaneously, the shaped signal is also sent to a timer or discriminator that sets a threshold for the events by generating a trigger, limiting the events that will be recorder by the MCA to those whose height is larger than the threshold.

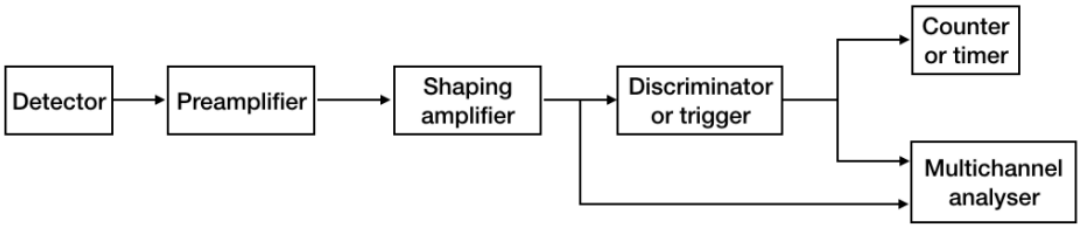

Figure 2.7: Schematic diagram of the detector and electronics readout chain in radiation measurements [53].

In **digital pulse processing** (DPP) systems however, the detector analogue signal is digitised with a sampling ADC immediately after the preamplifier that digitises the pulse, at fixed time intervals, into discrete samples. The digitised signal will then be shaped digitally, as the samples are sent to a field-programmable gate array (FPGA) that has been programmed with DPP algorithms to perform the energy, time and pulse shape analysis of the digitised pulses as shown in figure 2.8. Digitised pulses are processed in software, so the digital processor is the key element that shapes and digitises the signal every few nanoseconds. Finally, the communication interface transfers the information to a laptop.

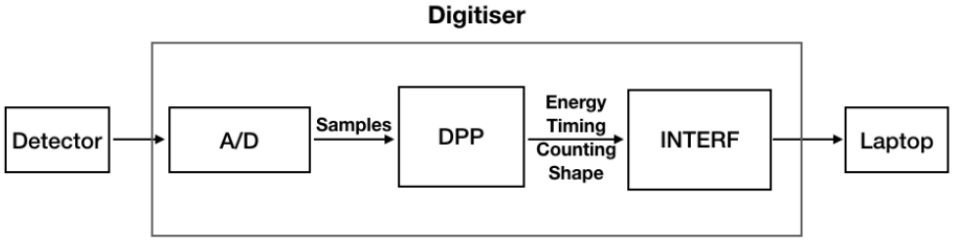

Figure 2.8: Schematic diagram of signal processing with a digitiser [86].

In all the experiments that are part of this project the signals are processed digitally using a CAEN digitiser, model DT5730 [86]. The digitiser has 16 channels and supports two types of DPP based algorithms: pulse shape discrimination (PSD) and pulse height analysis (PHA). Both of the algorithms are described in detail in the following chapter.

2.7 Summary

The protons generated during therapy penetrate the human body, and they can interact with matter in two different ways: via EM or nuclear interactions. Protons primarily interact with the atomic electrons via Coulomb interactions, depositing energy along their path. The energy deposition can be characterised by the Bethe-Bloch formula. This formula shows an inverse dependence with the square of the protons speed, therefore the energy deposition is maximum at the end of the proton's path, when their speed tends to 0. This gives the energy deposition a characteristic shape, the BP. The range of the protons can be estimated from that same formula. Simultaneously, protons may be scattered by the target nucleus. Although this process does not affect the range much, it causes the beam profile to spread along the path.

Protons can also interact with matter via nuclear reactions. These interactions do not affect the proton range, but reduce the dose as protons are removed from the beam. Nuclear reactions also are responsible for the production of secondary particles, including gamma-rays, neutrons and other ions,. The probability of emission of a certain particle is determined by the cross section of the responsible reaction. The two most important secondary particles emitted during PT are gamma-rays and neutrons, and their interaction mechanisms have been described in this chapter. The gamma-rays generated as secondaries are uncharged particles, and therefore they interact with matter through the photoelectric effect, Compton scattering or pair production.

The PGs emitted along the protons path are specially important, as they are used to determine the position of the BP, providing a real-time method for range verification. The main idea of the project is to detect the PGs from NPs that are radiosensitizers, therefore the basis of the enhanced permeability and retention effect that govern the dose enhancement are explained.

In this the chapter, the two types of detectors that are most commonly used in gamma-ray spectroscopy (scintillators and semiconductors) are introduced. Their interaction mechanisms and main properties have been described. The chapter concludes with a review of the electronics readout and pulse processing mechanisms.

Chapter 3

Experimental set up

In this chapter, we present the configuration of the experimental PG detector setup that was developed for this thesis project. It consists of two different types of radiation detectors: a scintillator and a semiconductor, and their mechanical collimators. To study the NPs effect, five different targets were developed in house with different materials, dimensions and concentrations. Finally, the characterisation of the two detectors will be presented, including their energy calibrations and energy resolutions, obtained using radioactive sources.

3.1 Targets

Five targets were used in this project: two nanoparticle-based targets, a solid PMMA target, a water target and a water phantom. All of them can be seen in figure 3.1.

Two **nanoparticle-based targets** were designed in house for the experimental work. Both targets are compounds of magnetite (Fe_3O_4) diluted in water, as the feasibility of this material for dose enhancement has been proven before [87; 88]. The density of the final material is calculated with the respective water and magnetite concentrations ($[water]$ and $[magnetite]$), and their densities (ρ) using equation 3.1. The first target is a NPs fluid with a 5% concentration of magnetite, which translates to a fluid density of 1.21 g/cm^3, and it is contained in a plastic box of dimensions 37×37×16 mm^3.

$$\rho_{fluid} = [water] \cdot \rho_{water} + [magnetite] \cdot \rho_{magnetite} \tag{3.1}$$

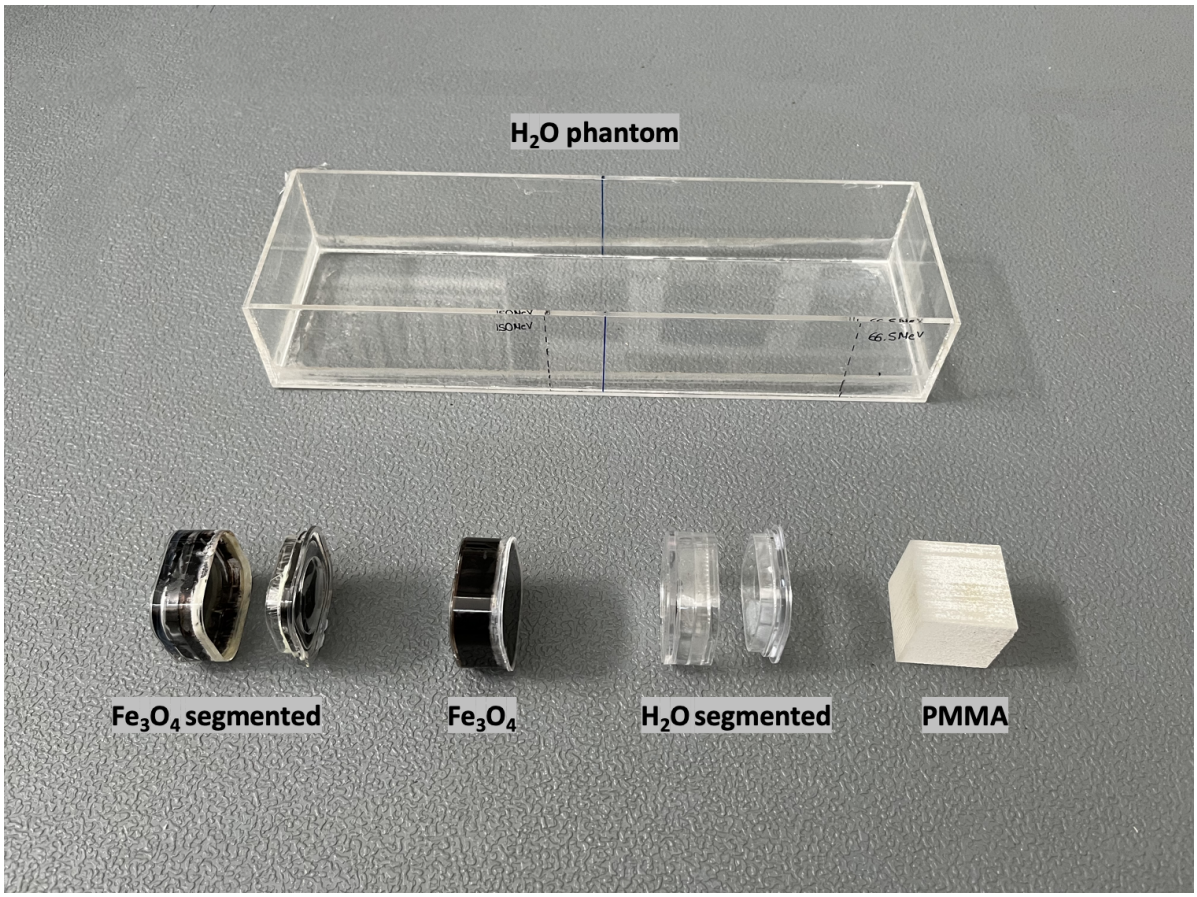

Figure 3.1: Targets used during the experiments: one PMMA target, two Fe_3O_4 targets and two water targets.

The second magnetite target has a more complex design, as it is a segmented target. It is divided into two regions, that can be seen in figure 3.2, where the distance between the two sections can be adjusted. The thickness of the first section was initially 9mm, but as the target was specially designed for low energy beam (E$\leq$ 40 MeV), the thickness of the front wall was reduced by 1.5 mm, creating a circular opening of 25mm diameter. With this modification, the final dimensions of the first section of the target are 33×33×7.5 mm^3. The second section of the target has a 1μm membrane on the front side, to contain the fluid while minimising the stopping of the incoming protons. Its x and y dimensions are identical to the first section for alignment, and it has a depth of 9 mm. Both sections are filled with the same NPs fluid, that has density of 1.36 g/cm^3, due to a concentration of 8.5% nanoparticles in water.

A **water phantom** of dimensions 80×40×270 mm^3 was created for high energy proton beams. All of the phantom's walls are made of plastic, except the top that is removed in order to place the continuous NP target inside, to emulate the conditions inside the human body. A second **water target** was developed for low energy beams. This target is also segmented, and has identical dimensions to the segmented magnetite target, but the filling fluid differs as the material inside is pure water. Both water targets can be seen in figure 3.1.

The last target is a solid **polymethyl methacrylate** (PMMA) target with cubic shape and dimensions 30x30x30 mm^3. The density of the target is 1.19 g/cm^3. This target was solely irradiated for low energy beams, and was placed inside the first water phantom for high energy beam measurements.

Figure 3.2: Segmented Fe_3O_4 target designed in house for low energy proton beams.

Each of the targets was placed in a remotely controlled linear platform that can move downstream with a sub-milimetrical precision. This will allow us to scan the emission of the gamma rays for different depths. The movement of the platform is managed by a laptop placed inside the beam room, that was remotely controlled from the data acquisition room. A summary of the targets, including the target material, its dimensions and densities can be seen in table 3.1 .

Target	**Dimensions (mm^3)**	**Density (g/cm^3)**
Fe_3O_4	37x37x16	1.21
Fe_3O_4 segmented	33x33x7.5 and 33x33x9	1.36
H_2O	80x40x270	1.0
H_2O segmented	33x33x7.5 and 33x33x9	1.0
PMMA	30x30x30	1.19

Table 3.1: Target materials, their dimensions and densities that have been irradiated during this project.

3.2 CLLB detection system

The first detector used during the experiment is an inorganic scintillator with a single CLLB ($Cs_2LiLaBr_6(Ce)$) crystal. The detector is a dual gamma-neutron sensitive scintillator detector that allows for simultaneous gamma and thermal-neutron detection. These two types of particles can be separated with pulse-shape discrimination algorithms (PSD). The CLLB is coupled directly to a SiPM for signal readout.

The detector is cylindrical and has a 1.5 inches (3.81 cm) diameter and length. The density of the material is 4.2 g/cm^3, and it has an energy resolution of around 4% at 662 keV for gamma-ray detection.

The detector was placed behind two lead blocks, separated by 3mm, to create a single collimation slit. Due to the collimation slit, the CLLB will only detect the gamma rays emitted in a certain region. The maximum area in which the gammas could be detected is called field of view (FoV). The FoV can be calculated by equation 3.2, where w corresponds to the slit distance, D to the width of the target, while d_1 and d_2 correspond to the distance between the target and the blocks and the distance between the beginning of the blocks and detector, respectively, as shown in figure 3.3 [89].

$$FoV = w\left(1 + \frac{2d_1}{d_2} + \frac{D}{d_2}\right) \tag{3.2}$$

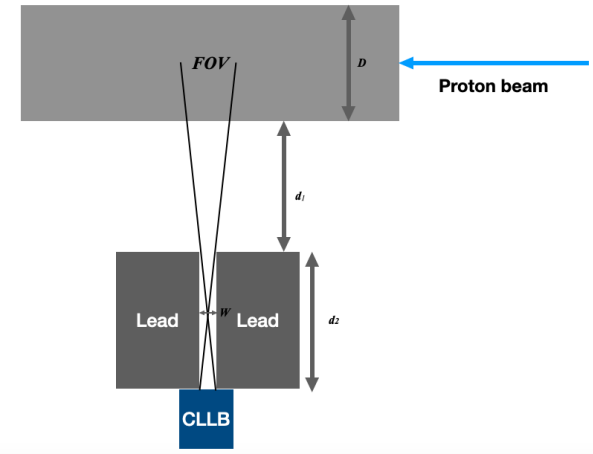

Figure 3.3: Schematic diagram of a CLLB detector collimated by two lead blocks and the FoV created (top view) [89].

3.3 Single-slit collimated HPGe detection system

A second detection system, based on a High-Purity Germanium detector (HPGe), was also used during the experiment to obtain gamma-ray spectra with a better energy resolution. The detector has a single high-purity germanium cylindrical crystal of 51.6 mm diameter, 60 mm length and density 5.33 g/cm^3.

Our detector, ORTEC model GMX-25200, is shown in figure 3.4. The crystal is mounted in a vacuum chamber, which is attached to the liquid nytrogen dewar, because as mentioned in section 2.5.1, germanium detectors need to be kept at a low temperature. The dewar has a capacity of 15 L and it will be periodically filled with liquid nitrogen. The cooling down time required by the detector is 6 hours, and the static holding time is 7 days. The detector needs a high voltage module to operate and during the experiment the ORTEC HV 659 module is used. The operating bias of the detector is -3500 V. If the system is warmed up while bias is on, the automatic HV shutdown will prevent damaging the detector by minimising the risk of preamplifier damage.

A Beryllium layer of depth 0.5 mm is placed before the germanium crystal allowing low energy photons to interact with the sensitive crystal due to its low atomic number. The end cap to crystal distance, i.e the distance between the beginning of the detector and the beginning of the germanium crystal, is 3 mm.

For collimation, two lead blocks, identical to the ones used for the CLLB, were used. The slit width is also 3 mm, but the FoV will differ from the CLLB, as the distances between the target, the blocks and the detector are different.

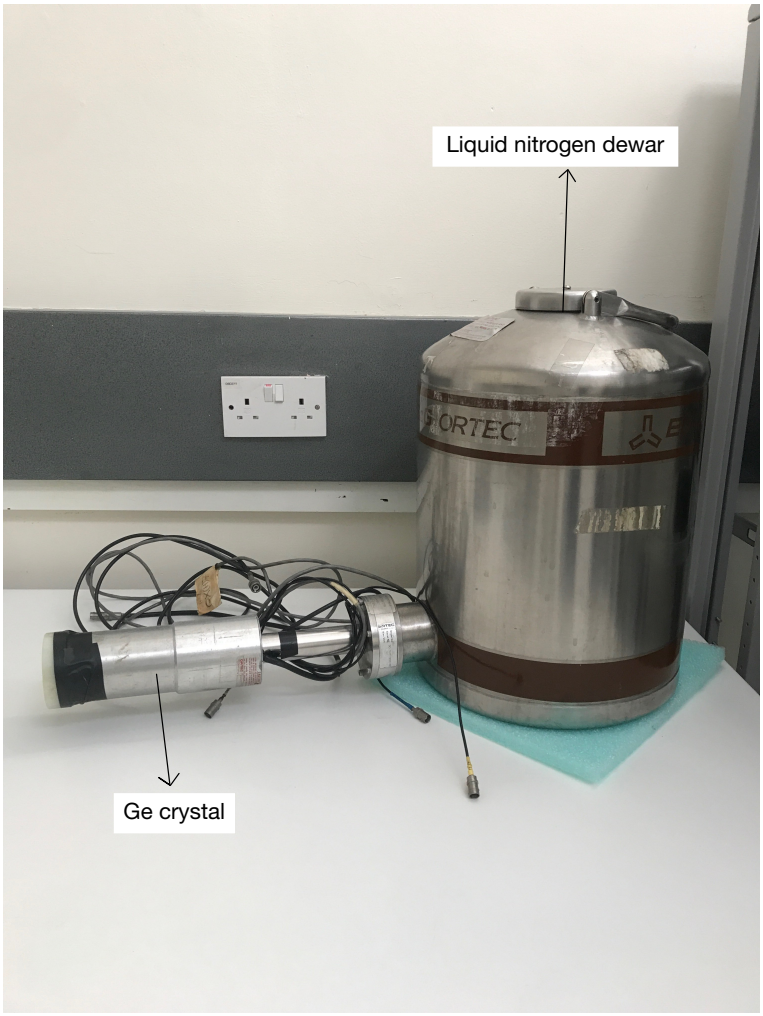

Figure 3.4: Ortec GMX-25200 High-Purity Germanium detector used in this project. The liquid nitrogen dewar and the position of the crystal are indicated.

3.4 Digital Pulse Processing Algorithms

The signals from both detectors are processed digitally, using a CAEN digitiser model DT5730 [86]. The digitiser features DPP firmware, so two different algortihms, PSD and PHA, can be implemented in the firmware.

3.4.1 Pulse Shape Discrimination

PSD algorithm allows for the differentiation between events whose shape is different. Detecting the differences in pulse shape is useful to discriminate different types of radiations, and in this work PSD will allow to discriminate the neutrons and gamma-rays when acquiring data with a dual scintillator.

The CLLB crystal has two different decay times: a fast decay of 180 ns and a slow decay of 1080 ns. The fractions of fast decay and slow decay are different for gamma-rays, with 61% fast decay and 39% slow decay, and neutrons with 50% fast decay and 50% slow decay [90]. This results in different pulse shapes, in which the neutrons have a longer tail than the gamma rays, as shown on figure 3.5(a). The signals are processed with two different energy gates, a short one and a long one to differentiate them. A function of the ratio between both will allow to determine the PSD factor that discriminates between the different types of radiation, as can be seen in figure 3.5(b).

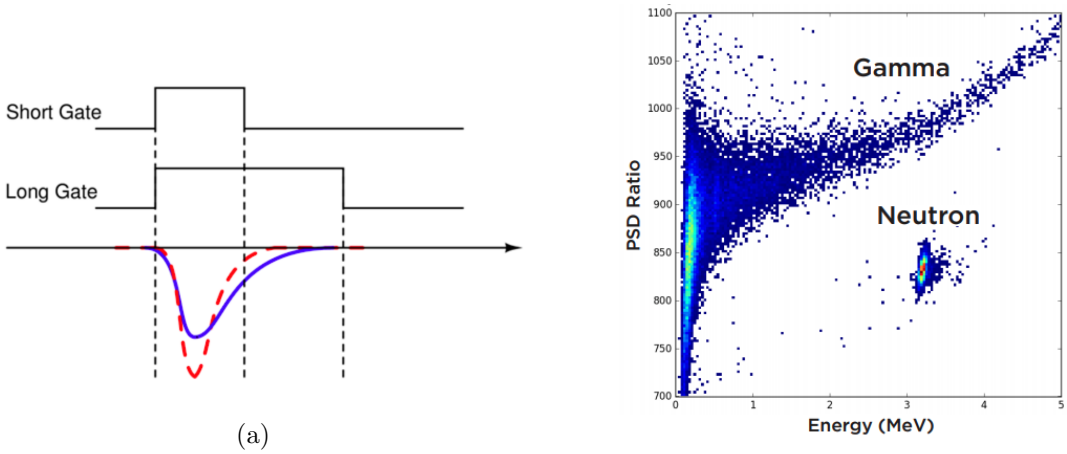

(a) (b)

Figure 3.5: (a) PSD of a neutron (blue line) and a gamma ray (red line) signal [86].
(b) PSD ratio of the CLLB crystal versus energy [91].

3.4.2 Pulse Height Analysis

The second pulse processing algorithm that is used during our experiment is PHA. The goal of the algorithm is to implement a digital version of the analog chain made by a shaping amplifier plus a peak sensing ADC. The digitiser admits signals directly from charge sensitive preamplifiers or photomultipliers, without needing to connect a shaping amplifier, allowing to obtain energy and time measurements [92].

The pulses are digitised and then passed through a trigger filter and a trapezoidal filter. The trigger filter differentiates the signal twice to generate sharp pulses, after passing the signal through a threshold. The trapezoidal filter is a filter to transform the exponential decay signal into a trapezoid with a flat top whose height is proportional to the amplitude of the pulse, i.e to the energy of the particle that interacts with the detector. Figure 3.6 shows the main parameters needed to apply the PHA method with a trapezoid filter.

This algorithm is optimised for the gamma-ray energy spectroscopy using long-tail pulses that are following a charge sensitive preamplifier stage in semiconductor detectors, and therefore in our experiment it is optimised for HPGe measurements.

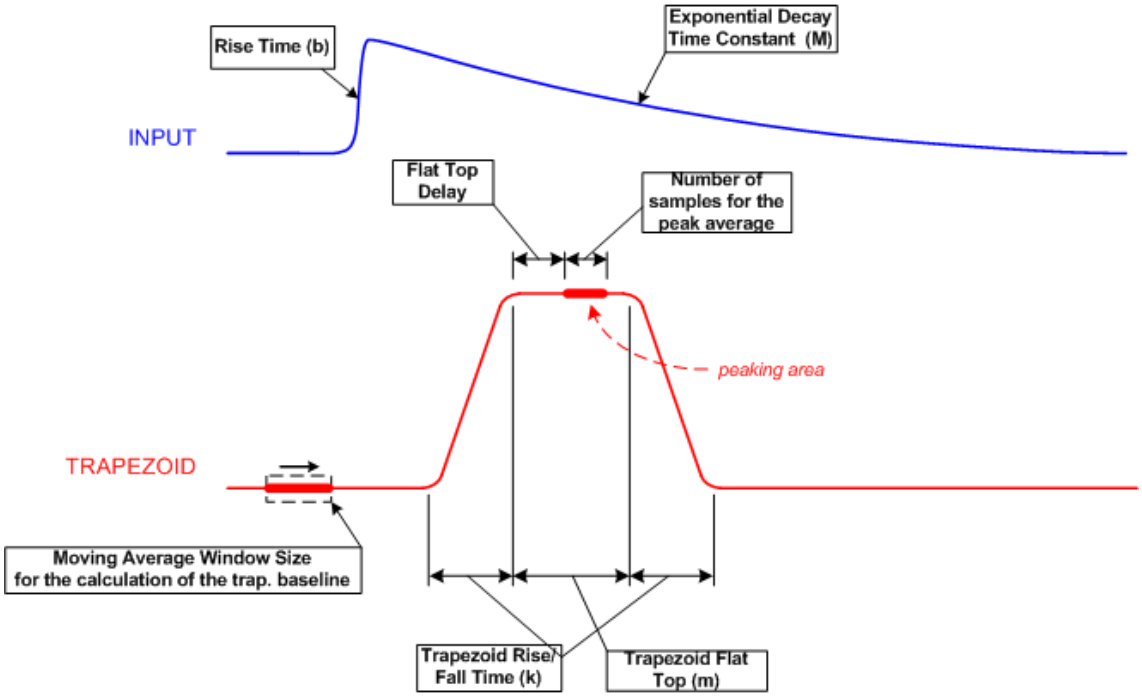

Figure 3.6: Pulse Height Analysis with trapezoid method [92].

3.5 Characterisation of the detectors

Characterising the detectors is a key process during any nuclear physics experiment. In this section we introduce the two main properties of any radiation detector: the energy calibration and the energy resolution. The energy calibration of a detectors is the function that relates channel number to energy, and it is calculated with radioactive sources in order to evaluate the response of the detector to radiation. The energy resolution is the ability of a detector to determine the energy of the incoming radiation and separate radiations that are close in energy. Energy calibration and energy resolution are obtained independently for both detector systems and compared to the theoretical values provided by the manufacturers.

3.5.1 Energy calibration and resolution of the CLLB detector

Firstly, we calibrated the CLLB using PSD algorithms. Two common radioactive sources were used: ^{137}Cs and ^{152}Eu. The first source has one characteristic gamma ray at 662 keV, while ^{152}Eu has six gamma rays at 779, 867, 964, 1086, 1112 and 1408 keV. A diagram of the experimental set up used for calibration of the scintillator detector can be seen in figure 3.7.

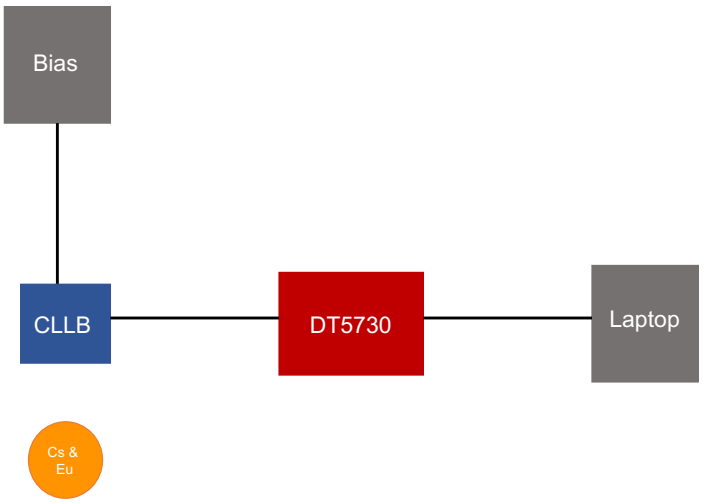

Figure 3.7: Experimental set-up for the energy calibration of the CLLB detector using two gamma-ray sources (^{137}Cs and ^{152}Eu).

The uncalibrated energy spectra of ^{137}Cs and ^{152}Eu is illustrated in figure 3.8, where 6 peaks can be clearly differentiated. The two peaks from ^{152}Eu, at energies 1086 keV and 1112 keV, merge together into a peak whose centroid is the average of the two, at 1099 keV. Each of the peaks follows a Gaussian distribution, while the background follows a linear trend. An algorithm was created to fit the peaks to a Gaussian function plus a first degree polynomial for the background, as can be seen for the 662 keV peak in figure 3.8. The obtained calibration points are then fitted to a linear function to obtain the function that relates energy and channel number, as shown in figure 3.9. The calibration function that can be applied to the gamma rays detected by the CLLB to convert channel number (x) into energy (E, in keV) is given by equation 3.3.

$$E = 7.267x - 7.767 \tag{3.3}$$

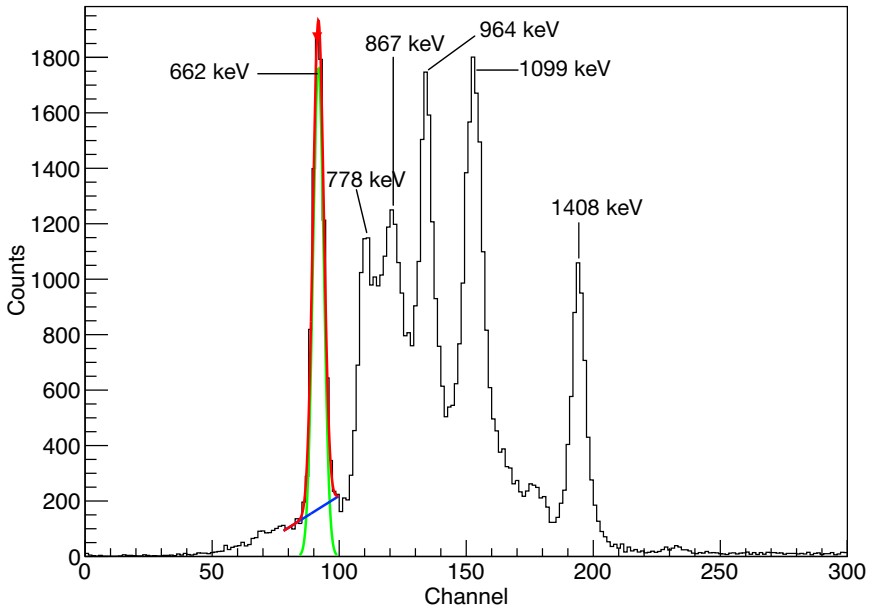

Figure 3.8: Uncalibrated energy spectrum of ^{137}Cs and ^{152}Eu in the CLLB detector using PSD algorithms. The peak at 662 keV is fitted with the sum (red line) of a Gaussian function (green line) plus a linear polynomial (blue line)

Once the histogram has been calibrated, the Full Width Half Maximum (FWHM) is obtained as a function of sigma, as shown in equation 3.4. The FWHM value is then be used to determine the energy resolution of the CLLB detector, using equation 3.5.

$$\text{FWHM} = 2.35\sigma \tag{3.4}$$

$$\text{Energy resolution } (\%) = \frac{\text{FWHM}}{\text{centroid}} \cdot 100 \tag{3.5}$$

The resolution obtained is (5.97±0.09)% at 662 keV, that is slightly worse than the manufactured established value of 4% at 662 keV, due to the use of PSD algorithms that are not ideal for energy spectroscopy. During this project we also implemented PHA algorithms for the CLLB detector, so we need to obtain the energy calibration and resolution for this mode of DPP, as the values will vary from the previous ones.

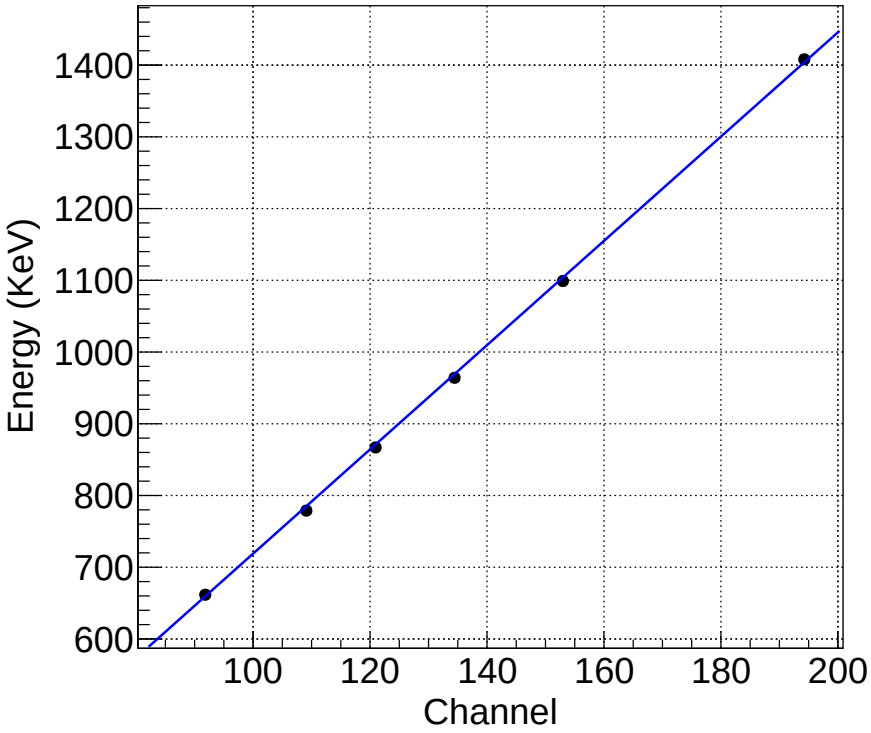

Figure 3.9: The fitted linear function for channel vs energy for the calibration of the CLLB detector using ^{137}Cs and ^{152}Eu peaks.

Using a set-up identical to the one illustrated in figure 3.7, the calibration of the CLLB detector using PHA algorithms is performed. The same calibration sources are used (^{137}Cs and ^{152}Eu). The uncalibrated spectra can be seen in figure 3.10. We observe that the peaks are shifted towards lower channel numbers in comparison to the previous one (shown in figure 3.8), therefore we expect a higher value for the first degree coefficient. After applying the sum of a polynomial and a Gaussian function to fit the peaks, we obtain the new calibration polynomial (in keV), given by equation 3.6.

$$E = 13.41x - 20.21 \tag{3.6}$$

The energy resolution is again be calculated using equation 3.5, and the final value obtained is (6.02±0.02)%. This value is very similar to the one obtained previously, because the PHA algorithm used was optimised for the germanium detector and not the CLLB.

Comparing the results obtained from the two DPP algorithms, we can conclude that the resolution does not change notoriously. In general, we would expect a better energy resolution for PHA algorithms, but as the parameters of PHA pulse processing were optimised for the HPGe, the value obtained is not ideal for CLLB. However, the calibration does change significantly, and this will need to be taken into account when we run the experiment.

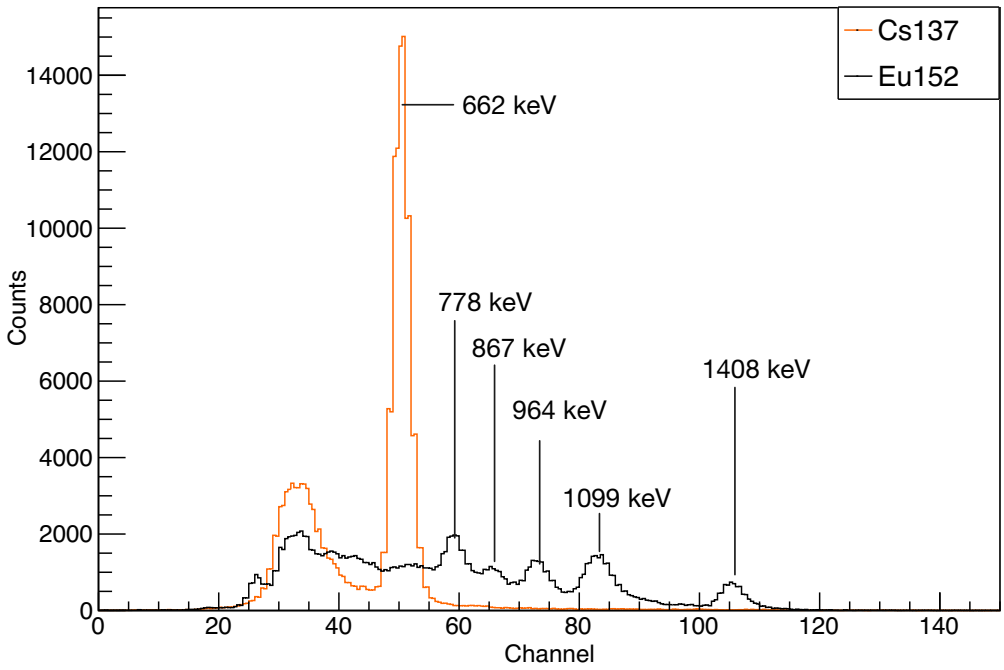

Figure 3.10: Uncalibrated energy spectrum of ^{137}Cs and ^{152}Eu in the CLLB detector using PHA algorithms.

3.5.2 Energy calibration and resolution of the HPGe detector

The HPGe detector was calibrated using PHA algorithms, that are ideal for semiconductor detectors, as discussed in section 3.4.2. The experimental set-up used for calibration can be seen schematically in figure 3.11, where two commonly used radioactive sources were placed in front of the germanium detector: ^{137}Cs and ^{152}Eu.

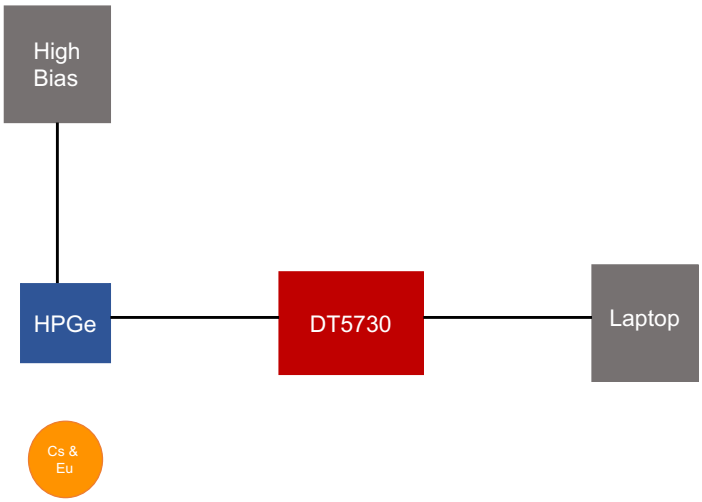

Figure 3.11: Experimental set-up for the energy calibration of the HPGe detector using two gamma-ray sources (^{137}Cs and ^{152}Eu).

As shown on figure 3.12, each of the sources produces its own spectra as they were measured individually. The uncalibrated spectra of the sources has several peaks, of which six are fitted (the ones in the region of interest, between 600 keV and 1500 keV). Using the same algorithm that was developed for the CLLB calibration each peak is fitted to a Gaussian function plus a linear background. The relation between the energy of the gamma rays detected (E) and the channel number (x) is calculated with a linear fit of the points. The obtained function for the energy calibration, in keV, is given by equation 3.7.

$$E = 11.74x + 7.05 \tag{3.7}$$

The energy resolution of the HPGe is obtained using equation 3.5. HPGe has a very good efficiency, and our particular Ortec detector has a theoretical resolution of 0.15% for 1332 keV. The experimental value at 1332 keV, obtained with a Cobalt 60 gamma-ray source, is (0.162± 0.007)%. This result is very close to the one provided by the manufacturer, and the slight difference can be justified by the age of the crystal, that was produced in 1986.

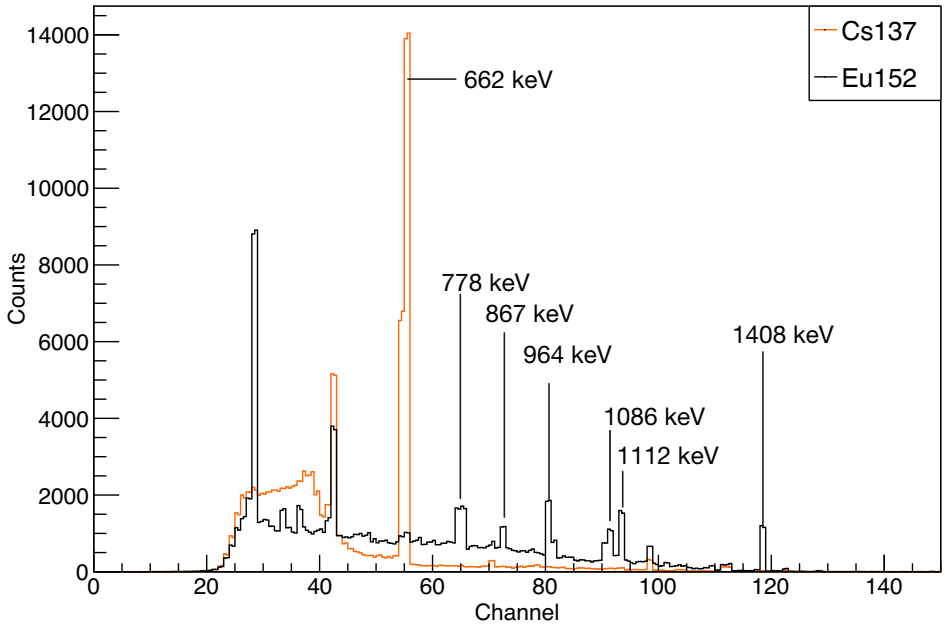

Figure 3.12: Uncalibrated energy spectrum of ^{137}Cs and ^{152}Eu in the HPGe detector using PHA algorithms.

3.6 Summary

This chapter shows the different components of the experimental set up. Firstly, the specifications of the different targets irradiated during the experiments are introduced. Later on, the configurations of the two PGI detectors used as part of this project are described. The first detector is a monolithic CLLB scintillator, while the second detector is a semiconductor HPGe detector. The electronic digital pulse processing algorithms that are implemented during the experiment are described.

Finally, the characterisation of both detectors is shown by studying the detector response to low energy gamma rays by using radioactive sources. Their energy calibrations are calculated, showing a good linear response for both detectors. The detector resolutions are obtained as a function of the energy, and the results provide a value of 6% for 662 keV in the CLLB detector and a much better result, of 0.162% at 1.332 MeV for the HPGe. The resolution values adjust well to the one provided by the manufacturers, confirming that out set up works correctly.

Chapter 4

Geant4 Monte Carlo simulation

Monte Carlo (MC) methods are widely used to simulate complex problems that involve the transport of particles through matter, and is a critical toolkit in nuclear physics [93; 94]. For this thesis, the MC simulation was performed with the GEANT4 toolkit (version 10.05.p01) as it includes a complete range of functionality, including tracking, geometry, hits and physics models [95].

In this project, the code was developed to study the emission of PG after the irradiation of a magnetite target, and compare it with the PG emitted from a water target. Several magnetite concentrations were initially modelled to study the change in the BP position, as well as the dose enhancement. The two detector systems, CLLB and HPGe, were implemented to study the detector response of our set-up. Finally, the intensity profile for two different magnetite targets, placed alone and in water, were studied at two different beam energies to understand how the emission of PG varies along the target length, with the slow down of the protons, and the effect the collimation slit has in this distribution.

4.1 Physics Lists

The physics processes are implemented in Geant4 by different physics lists. In this work protons and γ rays are the main particles of interest. With this objective, three physics lists were included in the simulation: RadioactiveDecay, emstandard-opt4 and QGSP-BIC-HP. RadioactiveDecay is needed to model the de-excitation of the generated excited nuclei, while Emstandard-opt4, is used for modelling the EM interactions and for tracking with higher

accuracy the hadrons, ions and electrons, using the most accurate standard and low-energy model [96]. The list QGSP-BIC-HP utilises the binary cascade model that describes the production of secondary particles generated through interactions of protons and neutrons with nuclei. This list is highly recommended for medical applications, and it is ideally used at energies below 200 MeV [97; 98].

The validation of the simulation must be performed to confirm that the Physics Lists chosen reproduce the experiment accurately. The EM processes and nuclear interactions will be validated independently. To validate the hadron interactions, which occur during the proton irradiation of the target, the cross sections must be obtained and compared to the literature, while for EM processes the range of proton beam will be obtained. In this project, the validation of the nuclear processes was performed with the total inelastic cross section of ^{56}Fe. The obtained results are shown in figure 4.1, where one can observe a good agreement between literature and simulation. The slight variation between the two can be explained with the difference in software to model them: our result has been produced with Geant4, whereas the tabulated values from TENDL are calculated with the Talys software [51]. The simulated result confirms the feasibility of QGSP-BIC-HP as an appropriate physics list for proton therapy simulations.

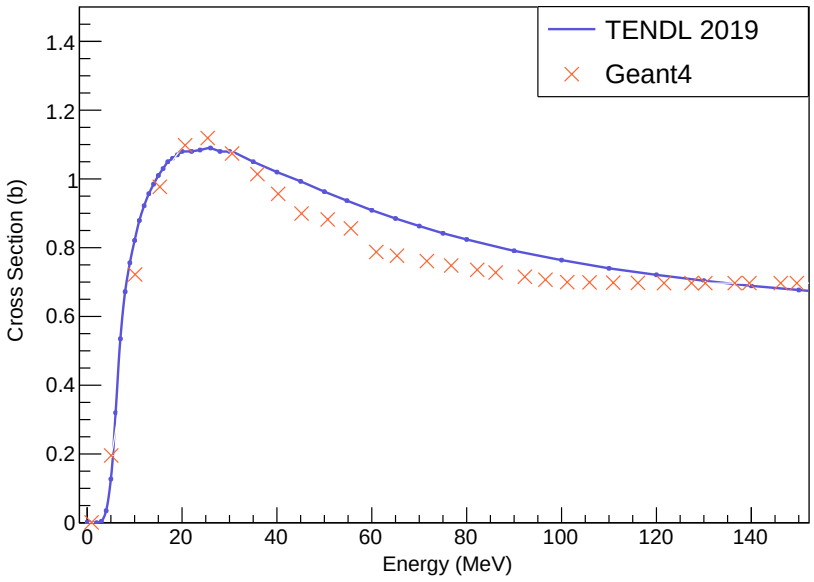

Figure 4.1: Total inelastic cross section of ^{56}Fe simulated in Geant4 compared to the literature value [51].

4.2 Range

To validate the EM models in the simulation, the BP was initially simulated for various beams of 10^6 protons with energies ranging from 36 MeV to 150 MeV, to study how the range varies with the energy of the incoming protons.

To assure that the beam stops inside the phantom, a uniform cylindrical water target of radius 4 cm and length 30 cm was created. For the water material we use the already defined material *G4_WATER*. Figure 4.2 displays the simulated dose-depth curve for the target, where we can observe that the range increases with the energy of the beam, while the dose rate decreases as the energy increases. Furthermore, one can observe that the BP broadens for higher energy beams due to the increase of depth that enhances the range straggling.

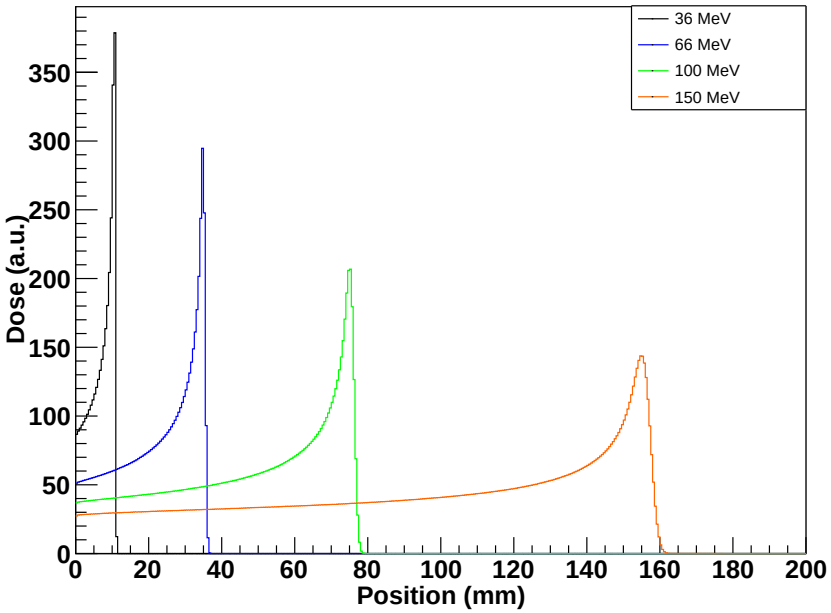

Figure 4.2: Geant4 simulated Bragg curves for a water phantom irradiated with a beam of 10^6 protons, with energies of 36 MeV (black line), 66 MeV (blue line), 100 MeV (green line) and 150 MeV (orange line).

Once the BP curves have been validated for a generic water phantom, the target material can be modified to pure magnetite (Fe_3O_4). The magnetite material needs to be defined by the user, and in order to do so we must implement each element individually. Once the two elements (Fe and O) have been defined, we create the final material, which is a combination

of these two nuclei, specifying their mass fraction as a percentage. Finally, the density of the fluid must be implemented. Magnetite has a higher mass density (5.2 g/cm^3) and atomic number compared to water, so the protons will stop earlier in the target, notoriously reducing the range of the beam. The comparison between the BP curves for a pure water phantom and a pure magnetite target can be seen in figure 4.3, where two different beams irradiated each of the targets.

The difference in the range for both materials is clearly visible: the position of the BP is shifted towards lower values for the magnetite, as expected due to the material properties. From this plot, and knowing the small concentration of magnetite in the experimental diluted targets, we can predict that the BP for our target fluid will be closer to the water results. The higher the concentration of magnetite, the more it will shift away from this value, towards the pure magnetite BP. This plot also shows a difference in the dose between the two materials, and this dose variation will be studied in more detail in the following section.

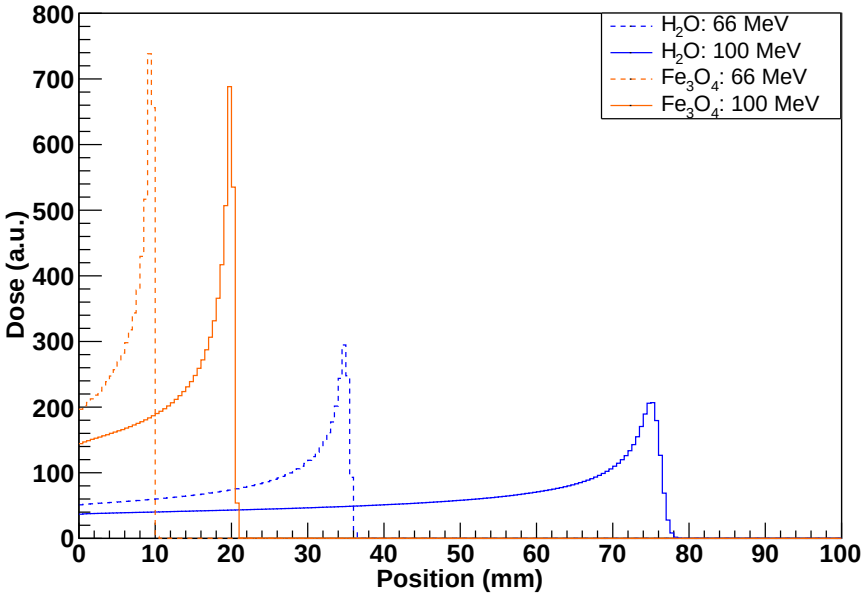

Figure 4.3: Geant4 simulated Bragg curves for water (blue) and magnetite (orange) for a beam of 10^6 protons and energies 66 MeV (dashed line) and 100 MeV (solid line).

4.3 Dose Enhancement with NPs

Magnetite NPs exhibit dose enhancing behaviour, that has been previously studied by other groups experimentally [87] and with Monte Carlo simulations [99]. To analyse the effects of the dose enhancement in the target, five different simulations were performed with a beam of 10^6 protons at energy 100 MeV. In every simulation a target of identical dimensions to the one designed for the range measurement was created and filled with magnetite diluted in water. The concentration of the two materials varied in every simulation, to analyse the possible cases, from pure water (Fe_3O_4 concentration equals to 0%) to pure magnetite (100% Fe_3O_4 concentration). To obtain the total dose deposited in the phantom, the integration of the depth-dose histograms was performed.

The DEF can be calculated from the simulation, by integrating the total dose and dividing by the reference dose (i.e pure water), as shown in equation 2.24. The results show that DEF increases as a direct function of the magnetite concentration, as expected. The obtained values of the DEF for different percentages of magnetite and water concentration in the target material can be seen in table 4.1. The DEF reaches a maximum of 4.26 for a pure magnetite target, which agrees well with other studies [87; 100]. Our targets, described in section 3.1, have a 5% and 8.5% concentration of magnetite, respectively, so the dose is enhanced by 12.6% for the continuous target, and between 12.6% and 25.2% for the segmented one. These results confirm the feasibility of the magnetite targets as a dose enhancer agent.

$[Fe_3O_4]$ (%)	$[H_2O]$ (%)	DEF
0	100	1
5	95	1.1262
10	90	1.2516
25	75	1.6775
50	50	2.4017
100	0	4.2556

Table 4.1: Simulated DEF for different concentrations of magnetite and water in a cylindrical phantom that is irradiated with 10^6 protons of 100 MeV.

4.4 Experimental Geometry

After studying the range and DEF simulated in a generic phantom with different energy beams, we can confirm that the results from the simulation are in good agreement with experimental observations, confirming that the implemented physics models are correct. Hence, we can develop a more complex geometry in order to replicate the experimental targets, detection systems and collimators, described in chapter 3. The obtained results will then be used for future comparison between the experimental work and the simulation.

The implementation of the geometry consists of two different parts: initially we must implement the targets, with the adequate geometries and concentrations, and then the detection system. The detection system includes the two detectors introduced previously (CLLB and HPGe), as well as their respective collimation systems.

4.4.1 Targets

A logical volume must be created for each target individually. All of our targets will be defined as solid boxes, hence their length, width and height must be implemented. The composition of the target is key, therefore, the elements that compose the target material, their atomic number, mass number, as well as their relative abundances must be defined. The total density of the material also needs to be implemented for accurate calculations.

Two different magnetite NPs targets were designed in-house for this simulation. For simplicity, the targets were defined as a uniform compound of magnetite diluted in water, instead of taking into account the size of the nanoparticles that conform the target. This approximation is accurate because the dimensions of the NPs are not relevant to our project, as the beam spot size during clinical treatments is in a higher scale ($\sigma \approx 2$ mm), and therefore the effects of the nanoparticles' diameter are negligible for the PGI analysis we perform. The two magnetite targets, whose properties were given in table 3.1, can be seen in the Geant4 visualisation shown in figure 4.4.

Two water targets are created during the simulation: a large water phantom, and a segmented target. The segmented target has the same dimensions as the magnetite target, and since the concentration of magnetite and water in the target can be modified directly, there is no need to define a separate segmented water target, as the two are never irradiated

together. The continuous water target, of dimensions 40×80×270 mm^3, is filled with pure water (*G4_WATER*), and will be used to place the magnetite target inside for higher beam energy simulations (above 40 MeV), and it can also be seen in figure 4.4.

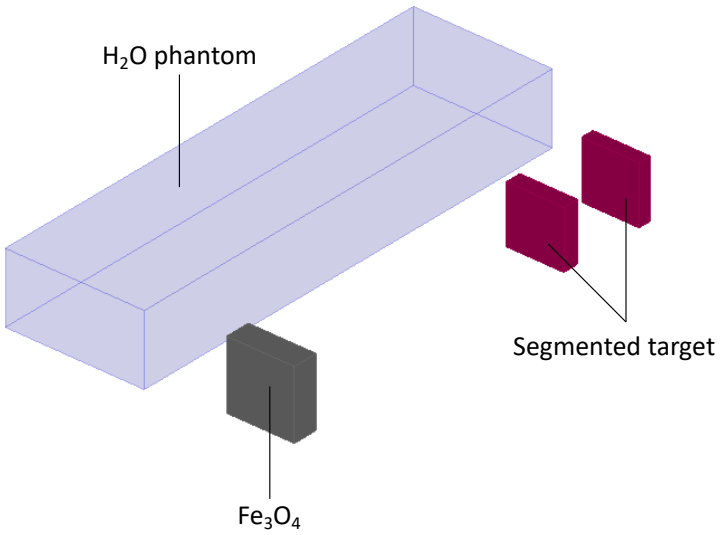

Figure 4.4: Geant4 simulated targets: a long water phantom, a magnetite cube and segmented target of variable composition.

4.4.2 Detection systems

The detection system in this project is formed by two detectors and their respective collimators. Although none of the electronic components are implemented in the simulation, implementing the detectors is a more complex process. The detectors are first created as logical volumes, whose placement and dimensions can be modified. Then, the volumes will need to be defined as sensitive volumes in order to detect the deposition of energy (hits). A hit is a snapshot of the interaction of the particles in the sensitive region of the detector, so each time a track goes through a sensitive volume and loses energy a hit will be created [101]. The hits will then be added and can later be analysed. The hits' information is crucial, as it directly relates to the detector's response.

Two different sensitive volumes are created, one for each detector. For the CLLB detector, a G4Tubs class is defined that corresponds to a cylinder of length and diameter 1.5 inch. The elemental composition of the CLLB is defined, as well as the density of the material that is obtained from the manufacturer [90]. The detector is defined as an ideal crystal, i.e perfect energy resolution is considered. The HPGe detector is defined following the same geometric class: a cylindrical Germanium crystal, of radius 5.16 cm and length 6 cm, is created and then defined as a sensitive volume in order to track radiation. To reproduce the real detector as accurately as possible, a Beryllium layer needs to be defined and placed before the crystal. This layer is a logical volume, as it is designed for attenuation purposes and does not measure radiation. To maintain consistency through our simulation, the HPGe is also defined as an ideal detector.

Each of the detectors are placed behind a pair of collimators in order to solely detect the gamma-rays emitted perpendicular to the target. Every collimator is defined as a solid box of dimensions $10\times12.6\times5.2$ cm^3, made from pure lead (Pb). A pair of such collimator blocks is placed immediately in front of each detector, and the distance between the two blocks will is kept constant at 3 mm to for a collimation slit. The position of the collimators, and the detector, will be shifted relative to the water phantom between the different simulation runs to study the emission of PG at different target depths.

The complete simulated geometry with the targets, detectors and collimators is adjusted for each of the experiments, as the target, target material, target placement and distances between the targets, the collimators, and detectors will differ between the experiments. However, a general representation of the whole simulated set-up can be seen in figure 4.5. This image shows all the components: the unsegmented magnetite target placed inside the water phantom for high energy proton beam irradiation, in which both collimators are separated 10 cm from the target, and the detectors are immediately placed behind the collimators.

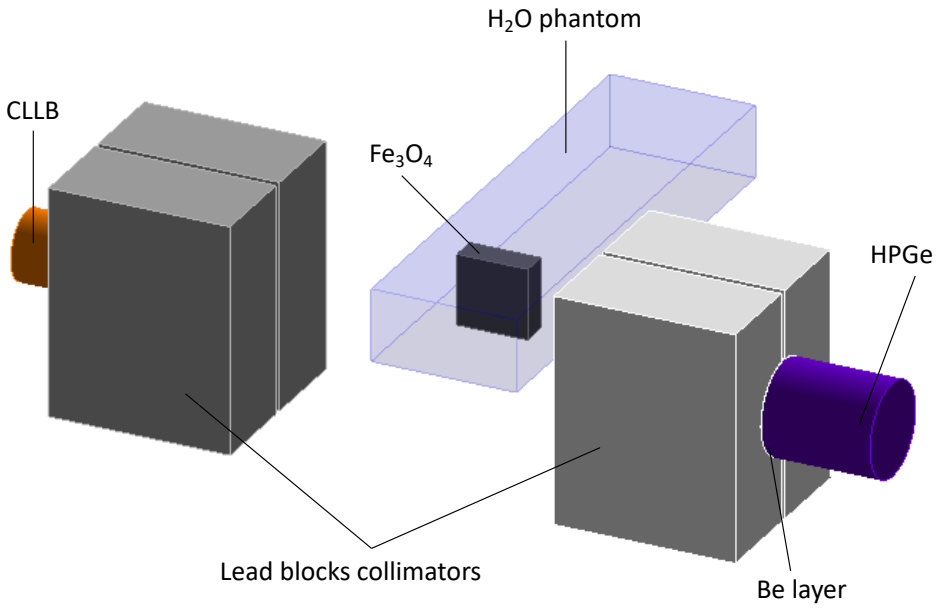

Figure 4.5: Geant4 simulated set up consisting of a magnetite target placed in a water phantom, a CLLB detector, a HPGe detector and four lead blocks acting as collimators.

4.4.3 Resolution Effects

Prior to the proton irradiation of the targets, both detectors are tested to ensure that they function correctly in the simulation. The two gamma-rays from a ^{60}Co radioactive point source were simulated, with energies of 1.172 MeV and 1.332 MeV. For simplicity the emission probability of both gamma-rays was set to be identical, producing 10^6 emitted gamma rays in total. The detectors' faces were placed 21.4 cm away from the source, aligned with the centre of the collimator window, and the emission distribution was set to be isotropic. The targets were removed to avoid any possible interaction with the gammas.

The ideal spectra obtained for both detectors, is shown in figure 4.6. We observe that the two gammas have been detected in both detectors, and their energies correspond to those expected from the radioactive source. Furthermore, we observe that when using the same radioactive source, placed at the same distance from both detectors, the CLLB detects

a higher number of counts than the HPGe detector, which is a direct result of the higher efficiency of the material.

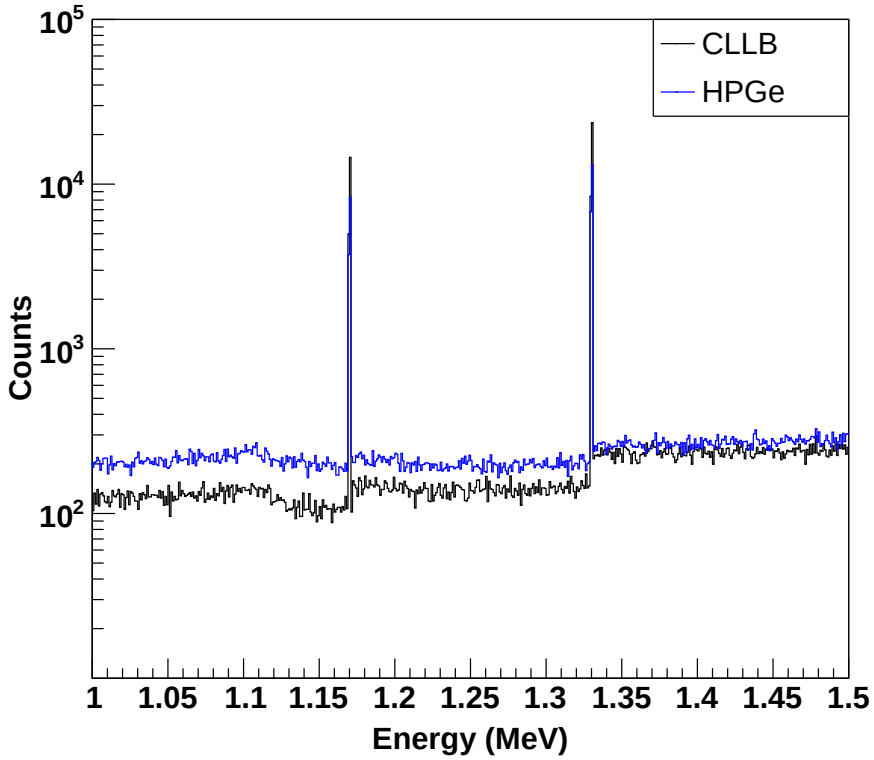

Figure 4.6: Geant4 simulated spectra for ideal CLLB and HPGe obtained with a ^{60}Co placed equidistant to both detectors.

Both detectors are responding to radiation and reproduce the expected spectra, so the next step is to obtain a more realistic response of both detectors by implementing the resolution. The resolution of the detectors is implemented as a Gaussian function, whose mean will be the energy of the detected radiation and the standard deviation is defined as the corresponding energy resolution of the detector. We assume that the resolution is constant, even though this is a coarse approximation it is valid here because there are always relatively high energy gamma-rays involved, and the resolution values are 4% for CLLB and 0.15% for HPGe, as calculated in chapter 3. The result after convoluting the expected detector resolution is shown in figure 4.7. There is a broadening of the peaks for both cases, but the effect is more notorious in the CLLB detector, as its resolution is worse. The broadening of the peaks is much wider, but the two peaks are clearly separated, and can be identified as two different gamma-rays.

With this result, we can conclude that while both detectors will be useful for PG detection, the CLLB will not allow us to differentiate between gamma-rays that are very close in energy, and will have much broader peaks than the HPGe.

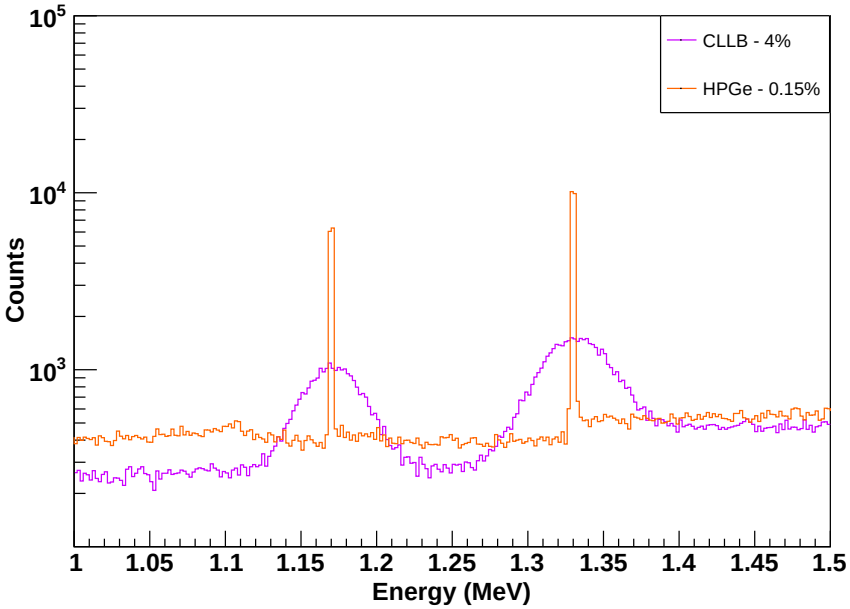

Figure 4.7: Geant4 simulated spectra for a ^{60}Co placed equidistant to both detectors with resolution 0.15% for HPGe (orange) and 4.0% for CLLB (pink).

4.5 Statistics of prompt gamma-rays

Secondary radiations are generated instantaneously as the incident protons slow down in the phantom, and includes PG, neutrons, scattering protons, electrons, positrons and other ions. The study focuses on the PG primarily, as these are the particles we will detect during our experiment. The secondary prompt gamma-rays produced during the proton irradiation of the different targets will be studied in this section. Studying the statistics of the secondary particles emitted has been crucial for the design of the targets and optimisation of the experimental set-up.

4.5.1 Prompt gamma-rays emitted

To verify the feasibility of the magnetite target as a gamma-ray emitter, we irradiated the target of lowest concentration (5%) with a proton beam of 10^9 protons, and a beam energy

of 38 MeV. As the NPs are diluted in water within the target, we also irradiated a pure water target of identical dimensions, with the same beam to identify the gamma-rays that are originated from the NPs. A comparison between the spectra of the emitted gamma-rays from the target can be seen in figure 4.8, in which we observe that there are several characteristic gamma-rays originating from the magnetite that are not present in the water target.

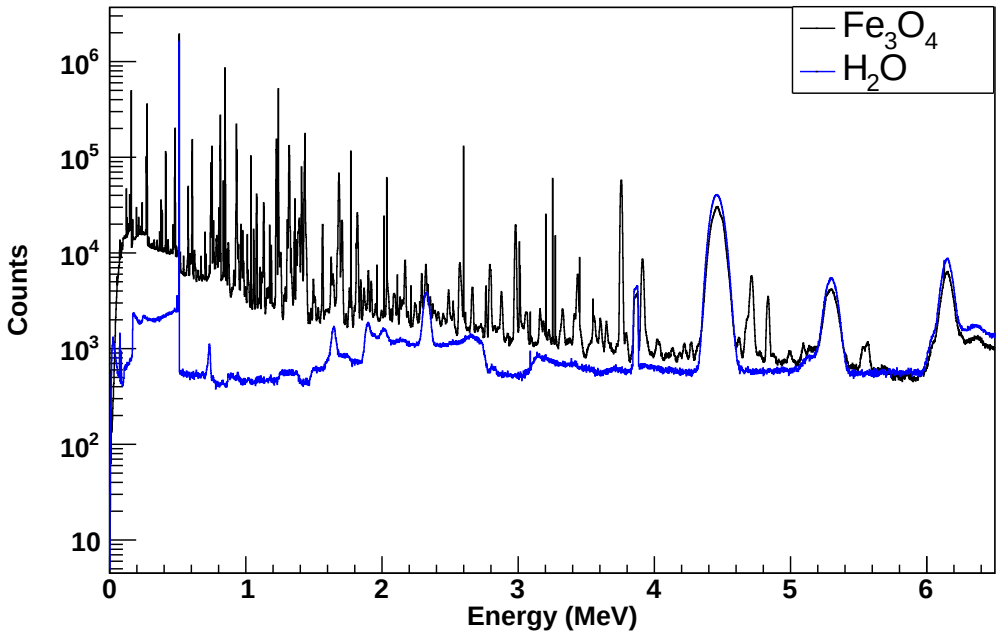

Figure 4.8: Geant4 simulated PG emitted spectra for water and magnetite targets with a proton beam of 38 MeV and 10^9 protons.

Figure 4.8 shows that there are five common gamma rays between the two targets. Their energies are 511 keV, 3.86 MeV, 4.44 MeV, 5.24 MeV and 6.13 MeV. While the first energy corresponds to the annihilation gamma-ray, the other three gammas are due to the oxygen component of the targets. The 3.86 MeV gamma-ray originates from the E1 transition of ^{13}C, that can be produced directly by the proton beam via the ^{16}O(p,p+^{3}He)^{13}C*, or with the secondary neutrons via ^{16}O(n,α)^{13}C*. The gamma-ray with energy 4.44 MeV is associated to the ^{16}O(p,pα)^{12}C reaction, while the 5.24 MeV gamma-ray originates from ^{16}O(p,np)^{15}O*. The inelastic scattering reaction, ^{16}O(p,p')^{16}O*, is responsible for the 6.13 MeV PG. The total PGs emitted at 511 keV are higher in the Fe_3O_4 target, while the other four PGs have a higher yield per proton for the water phantom, due to an increase in the oxygen concentration.

Table 4.2 shows the yield per proton of each PG for both target materials.

Energy (keV)	**Transition**	**H_2O yield**	**Fe_3O_4 yield**
511	Annihilation	1.64 x 10^{-3}	1.95 x 10^{-3}
3860	^{16}O(p,p+^{3}He)^{13}C* or ^{16}O(n,α)^{13}C*	8.69 x 10^{-5}	8.50 x 10^{-5}
4440	^{16}O(p,pα)^{12}C*	2.42 x 10^{-3}	1.78 x 10^{-3}
5240	^{16}O(p,np)^{15}O*	3.25 x 10^{-4}	2.67 x 10^{-4}
6130	^{16}O(p,p')^{16}O*	1.01 x 10^{-3}	8.32 x 10^{-4}

Table 4.2: Energies of the common gamma rays emitted from the magnetite and water targets during the proton irradiation, associated transitions and yield per proton for each target.

We can also observe that three of the peaks, at 4.44 MeV, 5.24 MeV and 6.13 MeV, are wider than other gamma-rays in the spectra, which can be explained with Doppler Effect. The Doppler broadening of spectral lines occurs if a gamma ray is emitted while the nucleus is in motion. The broadening directly relates to the life time of the element, if the element's life time is shorter than the time of flight of the nucleus, broadening will occur [102; 103]. The two aforementioned processes have very short half-lives: while the excited ^{12}C decays within the lifetime $\tau = 6.1\times10^{-14}$ s, the ^{15}O* decays within $\tau = 3.25\times10^{-12}$ s and the ^{16}O* has a lifetime of $\tau = 2.7\times10^{-11}$ s, which explains the broadening of the peak [104].

Looking at the differences between the two targets we observe that most of the characteristic PGs from magnetite are emitted in the low energy region, particularly below 4 MeV. Focusing the analysis on those with highest intensities, the spectra is reduced to the gamma rays located with energies between 800 keV and 1400 keV. A close-up of this region is shown in figure 4.9, where each peak is labelled with their corresponding gamma-ray energy.

The PGs intensity varies for the different energies, and therefore the yield per proton of every gamma-ray needs to be calculated to understand the contribution of each of them to the final spectrum. This information is also used to determine the number of protons required to irradiate the target during the experiment, in order to obtain sufficient statistics. The yield, energies and associated nuclear reactions of each PG are summarised in table 4.3.

Table 4.3 show that all the transitions, but one, come from the proton irradiation of ^{56}Fe. This result is expected, as it is the main contributing isotope in natural iron, with an abundance of 91.75% [105]. The other reaction comes from the irradiation of ^{54}Fe, the second contributing isotope with an abundance of 5.85% and a strong charge exchange cross section.

The two main gamma-ray contributions correspond to the 847 keV and 1238 keV gamma-rays, both generated from the inelastic scattering of ^{56}Fe. The first gamma-ray, at 847 keV, corresponds to the E2 transition from $2^+ \rightarrow 0^+$ in ^{56}Fe, while the one at 1238 keV is associated to the E2 transition $4^+ \rightarrow 2^+$. These results confirm that the simulated histograms agree with the expected literature value [106], as the inelastic scattering of ^{56}Fe is the most likely reaction to occur during the proton irradiation of an iron target, due to its higher cross section.

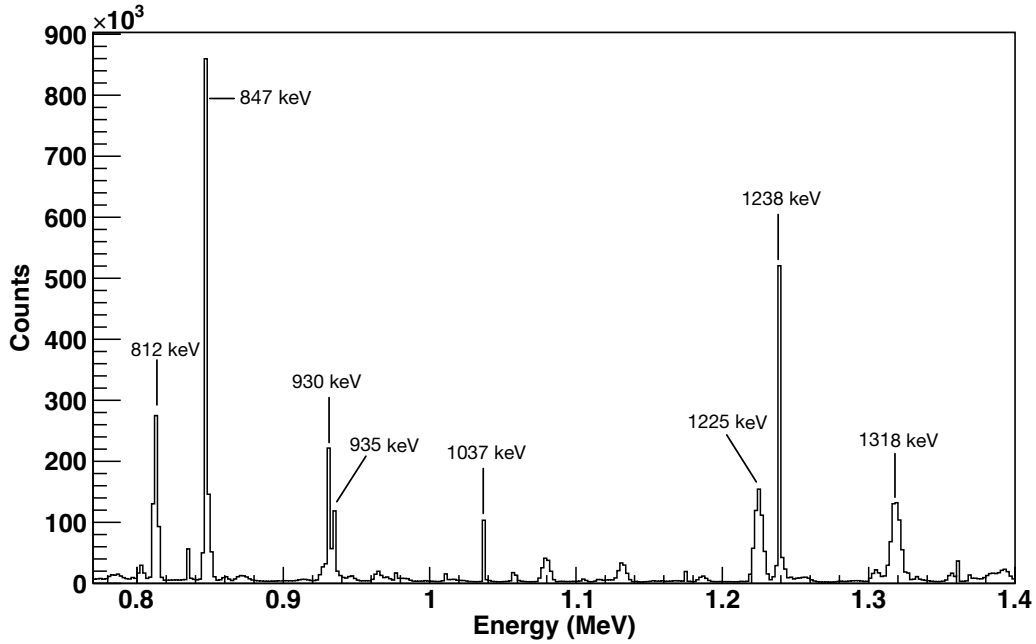

Figure 4.9: Geant4 emitted PG spectra for a magnetite target irradiated with a proton beam of 36 MeV in the region between 0.8 MeV and 1.4 MeV. Each major peak is labelled with its energy.

Energy (keV)	**Transition**	**Yield per proton**
812	^{56}Fe(p,n)^{56}Co	5.18 x 10^{-4}
847	^{56}Fe(p,p')^{56}Fe	1.13 x 10^{-3}
930	^{56}Fe(p,n+p)^{55}Fe	3.38 x 10^{-4}
935	^{54}Fe(p,n)^{54}Co	2.08 x 10^{-4}
1037	^{56}Fe(p,p+2α)^{48}Ti	1.17 x 10^{-4}
1225	^{56}Fe(p,γ)^{57}Co	5.49 x 10^{-4}
1238	^{56}Fe(p,p')^{56}Fe	6.45 x 10^{-4}
1316	^{56}Fe(p,n+p)^{55}Fe	5.73 x 10^{-4}

Table 4.3: Energies of the gamma rays emitted from the magnetite target during the proton irradiation, in the energy range 800-1400 keV, and associated transitions and yield per proton.

4.5.2 Prompt gamma-rays detected

To study the detector response much higher statistics are needed and in order to achieve the desired number of events, several parallel runs will be performed on the Viking research computing cluster [107].

For this project a total of 10^{10} protons with a beam energy of 36 MeV irradiate the magnetite target with 5% NPs concentration. The spectra of the emitted gammas, and the ones detected by ideal CLLB and HPGe detectors, in the region between 0.65 and 2 MeV, can be seen in figure 4.10. From this figure we can confirm that ideal detectors are capable of detecting the characteristic gammas from iron after the proton irradiation. A quantitative comparison for the 847 keV gamma-ray shows that the percentage of detected gammas in the CLLB is 0.130%, while for the HPGe the value is reduced to 0.070%. Therefore, an ideal CLLB will detect 1.86 times more PGs with an energy of 847 keV than the HPGe. This difference between the two materials can be explained with the difference in effective atomic number between the materials, as the interaction probability depends on Z, as explained in section 2.2.1.

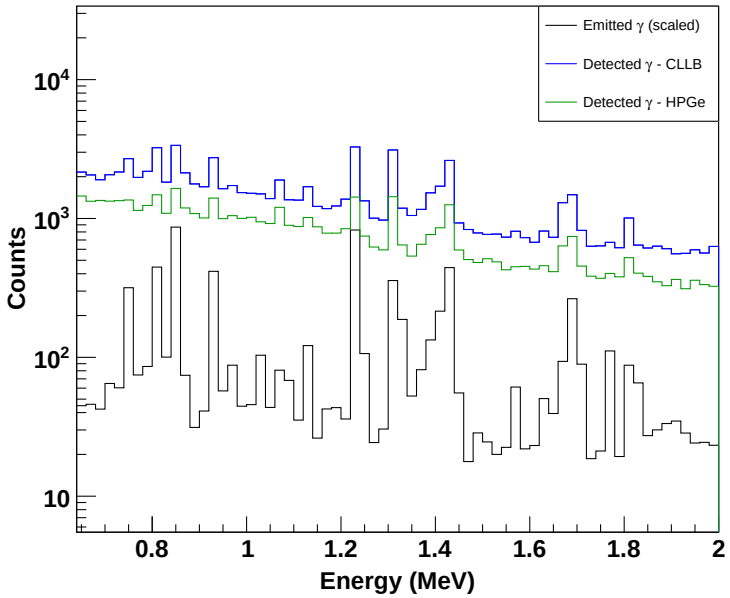

Figure 4.10: Geant4 detected gammas by the ideal CLLB and HPGe detectors in the energy range 0.6 to 2 MeV.

To compare the simulation with the experimental results, we need to enact the energy resolution of both detectors. The results can be seen in figure 4.11, where one can observe that that this implementation will not drastically modify the detected PGs for the HPGe detector, but it will notoriously affect the CLLB spectrum. The low energy resolution of the CLLB detector will broaden the peaks, and it will not allow us to differentiate the gamma rays in the region between 700 and 900 keV, as the peaks coalesce into a broader peak.

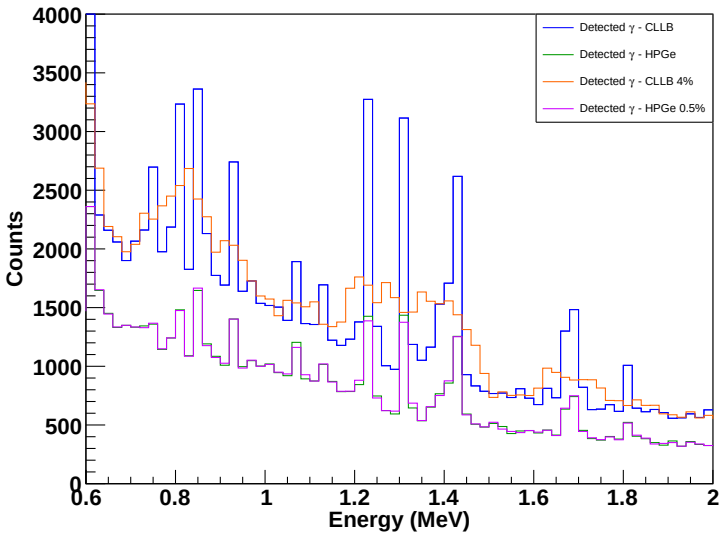

Figure 4.11: Geant4 detected gammas by the ideal CLLB and HPGe detectors, and comparison with realistic detectors in which the energy resolution has been implemented.

4.6 Prompt-gamma intensity profile

The emission of gamma-rays in a target is non uniform, as the statistics of prominent PG increase as a function of depth, reaching a maximum near the BP region. The PG intensity versus depth distribution for various energies will show how the intensity of emission varies through the target, in order to draw conclusions on the BP position. In this section, the PG intensity profile will be studied for different beam energies and targets, in order to evaluate the intensity profile.

4.6.1 Segmented target

To study the variation of the intensity for different positions, the irradiation of the segmented magnetite target, with a 8.5% NPs concentration, is performed. The dimensions of the target are shown in table 3.1, and the separation between the two targets is set to 1.6 cm. This target is ideal to study how the intensity changes before reaching the fall-off region, as there is an air region between the two targets that will allow us to study the possible gamma-rays that go through the collimator slit and will be detected, even when they have not been emitted perpendicularly to the beam line.

A beam of 10^{10} protons with an energy of 36 MeV irradiated the target. The intensity histogram as a function of depth for the energy region between 700 keV and 1000 keV is shown in figure 4.12 for the emitted gamma rays, in which the limits of the target are indicated. Three regions are differentiated: the first one corresponds to the front part of the segmented target, the middle region is the air gap between the targets and the third region is the second part of the segmented target. We observe that no characteristic PG are emitted in the region between the two segments of the target, as expected.

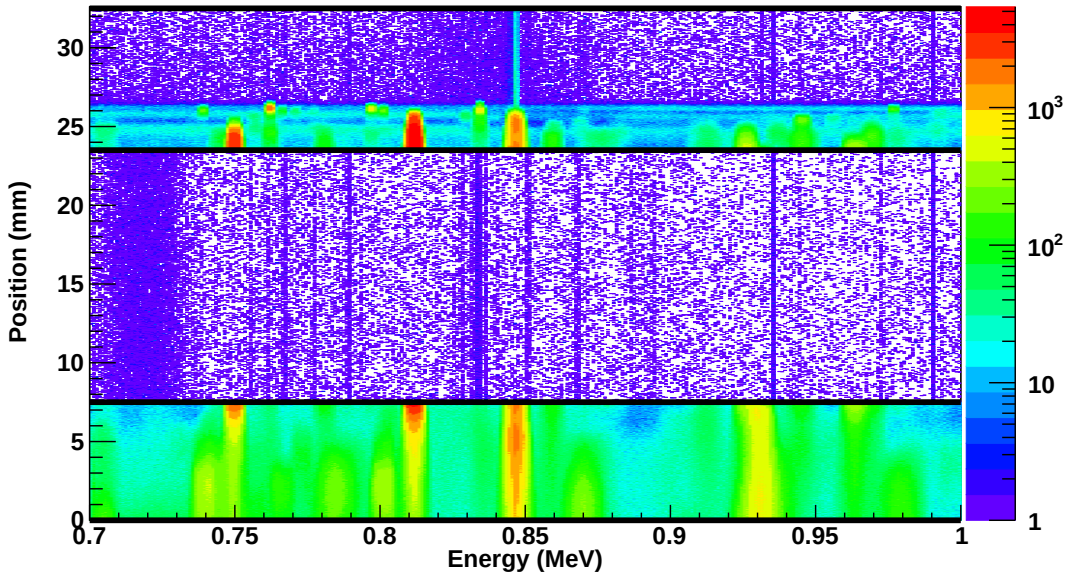

Figure 4.12: Geant4 simulated PG energy versus depth in a segmented magnetite phantom irradiated with a proton beam of 36 MeV. Three different regions are visible corresponding to the two parts of the magnetite target (between 0 mm and 7.5 mm and between 23.5 mm and 33 mm), while the middle region (between 7.5 mm and 23.5 mm) corresponds to the air gap between the two segmented sections.

Figure 4.12 shows that in both of the segmented magnetite regions, there are two main gamma-rays. Their energies are 812 keV and 847 keV, which correspond to decays from excited ^{56}Co and ^{56}Fe, respectively. The emission of the 812 keV gamma-ray reaches a maximum before the BP region, and it stops after the protons have reached this region where their speed is 0. However, the gamma-ray from ^{56}Fe reaches a maximum at the end of the proton path, but its emission does not stop once the BP has been reached. The intensity of this PG lowers, but it is still emitted until the end of the target, even passed the BP region. This is because the population of the 847 keV state can also occur by secondary neutrons, generated during the proton irradiation, which continue past the BP region and can excite the ^{56}Fe nuclei present in the final region of the magnetite target.

The collimation slit is then placed at different target depths to obtain the histograms for different positions, separated by a 3 mm window. To simulate the moving of the linear stage, the collimators will be placed at different depths to study the PG profile versus the positions. Figure 4.13 shows how the intensity of several gamma-rays changes within the target region. We can observe a run in which no characteristic gamma rays from iron are seen, this is the run collimated at 10.50 mm and represented with a dashed line. It corresponds to the inter-space between the two parts of the segmented target, and therefore no characteristic gamma rays are emitted nor detected as there are no NPs in this region.

In figure 4.13, the second run with lowest statistics corresponds to a collimation window placed at 31.50 mm, this is past the Bragg peak. In this region, the protons have fully stopped in the target and no gammas are emitted from the proton irradiation. However, a remaining peak at 847 keV is visible, and it corresponds to the first excited state of ^{56}Fe generated by the neutron irradiation of the target, which agrees with the previous results.

The different gamma-rays peak at different positions, due to the direct relation of the cross sections with the energies, that was shown in figure 2.3. The 847 keV gamma, originating from the inelastic scattering of ^{56}Fe, will peak before the 812 keV, as the cross section for the inelastic scattering of ^{56}Fe reaches a maximum later than the cross section for the production of ^{56}Co, responsible for the 812 keV gamma-ray.

The variation on the intensity of the gamma-rays versus the position can be used to draw conclusions on the proton range: the emission of gamma-rays will be maximum for the region before the BP, and the number of gammas will depend on the cross section of the process. However, the different gamma rays show maximum number of counts at different collimator positions.

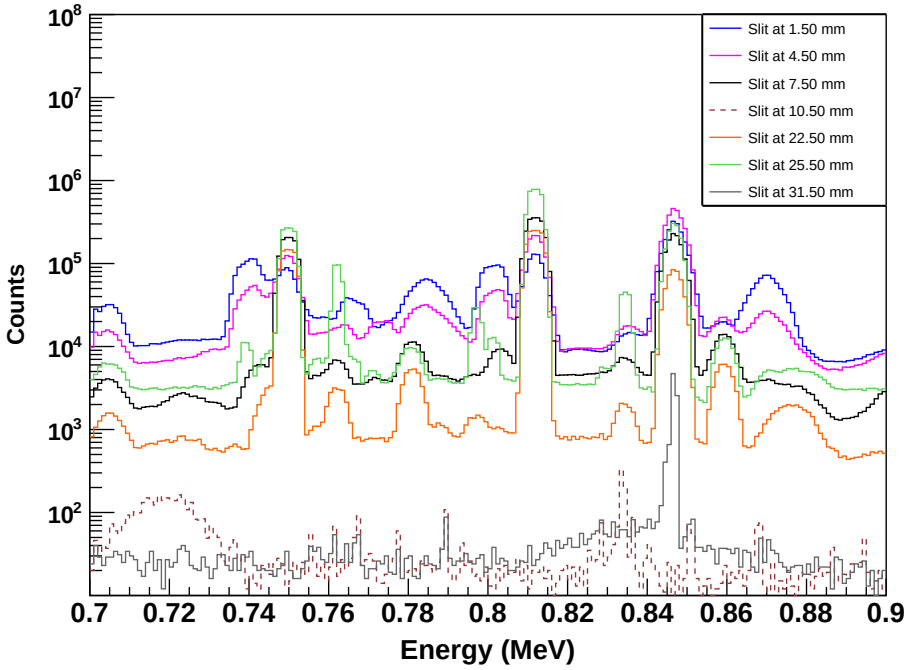

Figure 4.13: Geant4 simulated PG spectra for different positions of the slit collimations in the segmented NPs target.

To study in more detail the variation in intensity as a function of depth for the different gamma rays, the yields from the dominant reactions are plotted as a function of depth separately. Figure 4.14 shows how the counts vary with the position independently for the four processes with the highest cross sections. We observe that in the second region of the target they all peak at the same depth, while in the first region the position of the peak changes between processes. The 812 keV gamma-ray from ^{56}Co peaks later than the other gamma-rays, which agrees well with the expected results from the cross-sections.

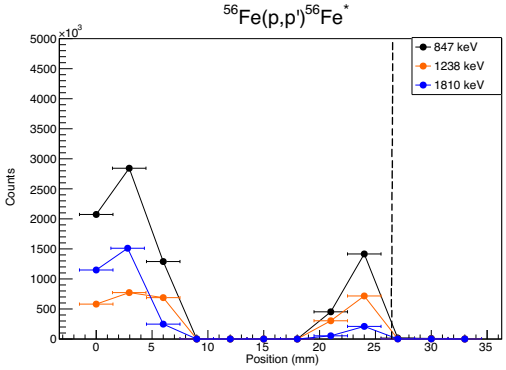

(a) Gamma-ray intensities as a function of the depth for protons on ^{56}Fe.

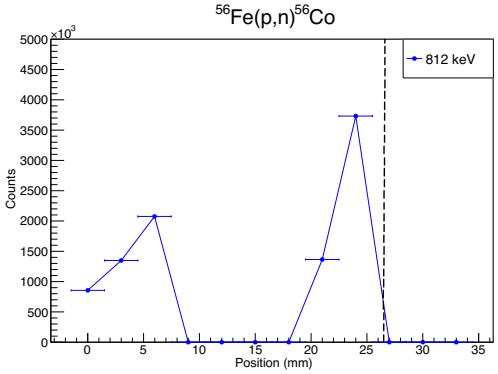

(b) Gamma-ray intensity as a function of the depth for charge exchange reaction populating the first excited state in ^{56}Co.

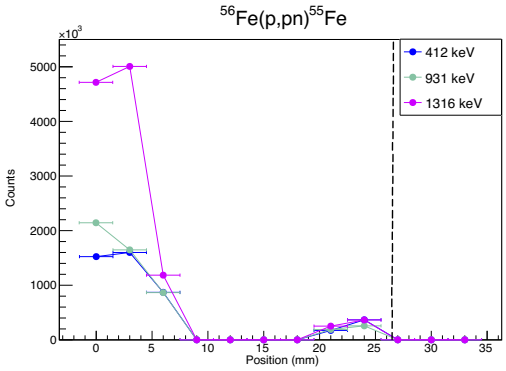

(c) Gamma-ray intensities as a function of depth for a neutron knockout reaction producing ^{55}Fe.

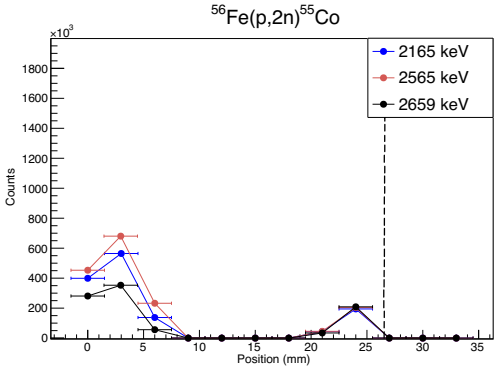

(d) Gamma-ray intensities as a function of depth for a two neutron knockout reaction producing ^{55}Co.

Figure 4.14: Projection of the intensity profile for different collimator positions for the segmented target. BP position is indicated with a dashed line. The uncertainties in x and y are too small to be visible, 0.1 mm and $\leq$2500 counts respectively. For clarification, the size of the collimated window is indicated in the x axis for each of the points.

The results obtained for the segmented target are affected by the empty region between the targets, which changes the statistics of the detected gammas in the limits of the targets. For this reason, and due to the collimator width, the results obtained when the collimation slit is placed at the end of the first target, or the beginning of the second, can not be compared to the results obtained when the collimation window covers a bigger target region. To compare the two sets of results we must collimate the empty region with 1.5 mm of each of the targets, disregarding the air region between the two of them. This reduces the geometric effects, producing results that can be compared accurately with the other regions. With this new

collimation geometry we reproduce the previous results, obtaining a new distribution that can be seen in 4.15. The trend is smoother now, as we have no air gaps between different measurements. The overall trend remains the same: the number of counts increase, until the region before the fall-off, and then the counts decrease quickly. The results obtained show how important it is to choose an appropriate collimation slit.

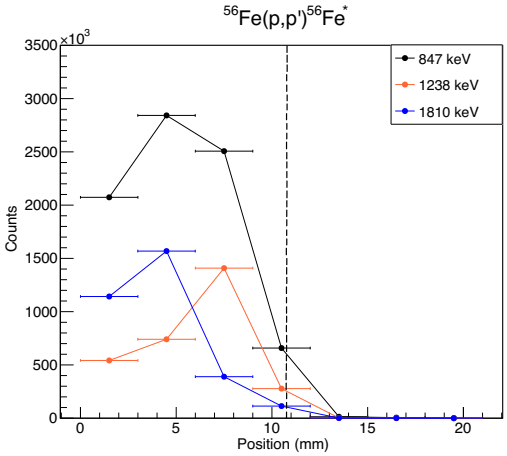

(a) Gamma-ray intensities as a function of the depth for protons on ^{56}Fe.

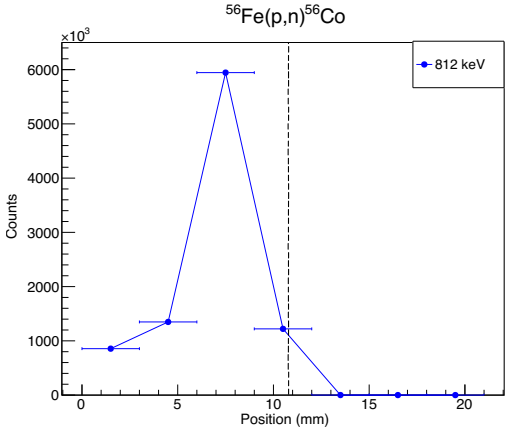

(b) Gamma-ray intensity as a function of the depth for charge exchange reaction populating the first excited state in ^{56}Co.

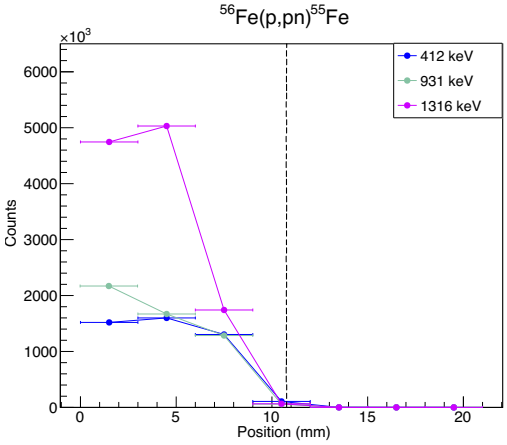

(c) Gamma-ray intensities as a function of depth for a neutron knockout reaction producing ^{55}Fe.

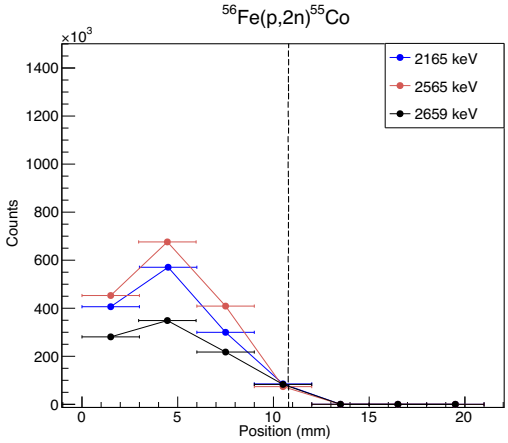

(d) Gamma-ray intensities as a function of depth for a two neutron knockout reaction producing ^{55}Co.

Figure 4.15: Projection of the intensity profile for different collimator positions, after eliminating the empty air region between the two segmented targets. BP position is indicated with a dashed line. The uncertainties in x and y are too small to be visible, 0.1 mm and $\leq$2500 counts respectively. For clarification, the size of the collimated window is indicated in the x axis for each of the points.

To further study the effect of different collimation slits the total the number of events detected for several collimation windows for the 847 keV gamma ray can be seen in figure 4.16. One can clearly observe the effect of different sized windows: the number of gammas detected is lower for narrower slits, as fewer events pass through it. Widening the collimation window allows to detect more gammas, however the precision in the spatial origin of those gammas will be reduced. Therefore finding the optimum slit size is key, as we want to obtain enough statistics and reduce the position determination error as much as possible.

In the experiment a compromise between the number of events and the precision in the positioning to relate the 847 keV gamma emission to the BP must be reached. With the results obtained in figure 4.16, we observe that if a 1 mm or 2 mm window are used, the number of gamma rays detected drops significantly, while if the window size is 3 mm or 4 mm the variation in number of events is not that notorious. As a reduction in the positioning error is desired, a 3 mm window is the ideal collimation slit for this project.

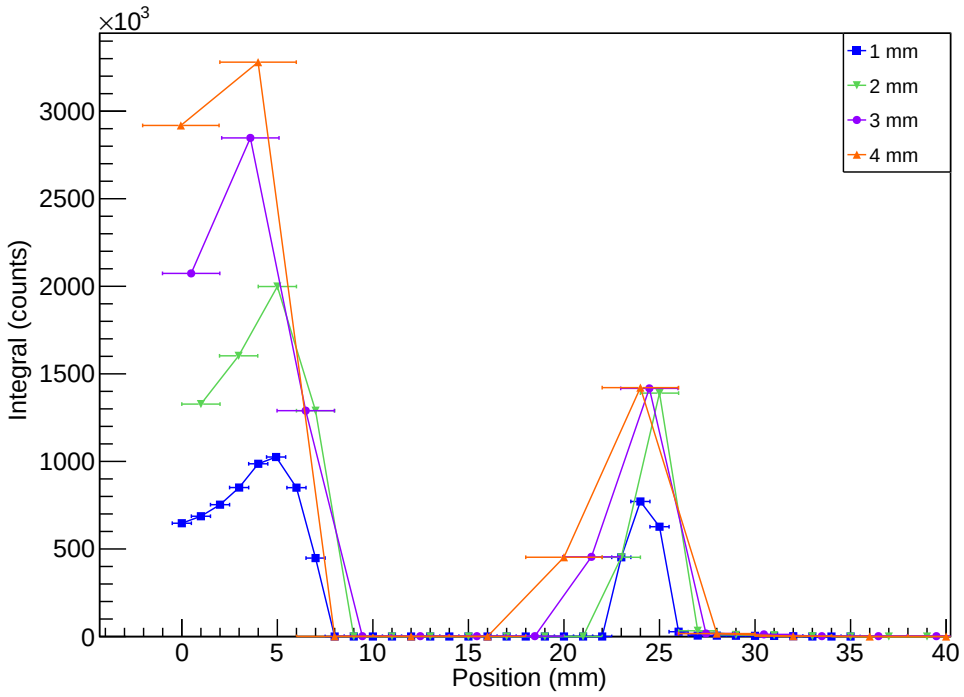

Figure 4.16: Geant4 simulated emitted PG counts versus position in the magnetite segmented target for the 847 keV PG using different collimation slits: 1 mm (blue), 2 mm (green), 3 mm (violet) and 4 mm (orange).

4.6.2 Continuous target

To compare the results, the same analysis must be performed for the continuous magnetite target. Figure 4.17 shows the intensity profile for the magnetite target with 5% concentration, placed inside the water phantom, and irradiated with a proton beam of 66.5 MeV. The walls of the magnetite target are indicated with black lines, and we can observe that the emission of the characteristic gamma-rays never exceeds the region of the target, proving that all the observed gammas are characteristic from the magnetite. The BP is also indicated with a dashed line, and we observe that the maximum intensity of the gamma-rays is reached before the BP. Therefore, the placement of the collimator system is crucial to detect the desired gamma rays. Depending on the placement of the collimator window, some gamma-rays will not be visible. If we place the collimator system between the beginning of the target and the BP, all the gamma-rays will be observed and their intensity will vary depending on the collimator's position, reflecting the cross section for the corresponding nuclear reaction at that proton energy. Contrariwise, if we place the collimation slit beyond the BP only the 847 keV gamma-ray will be detected.

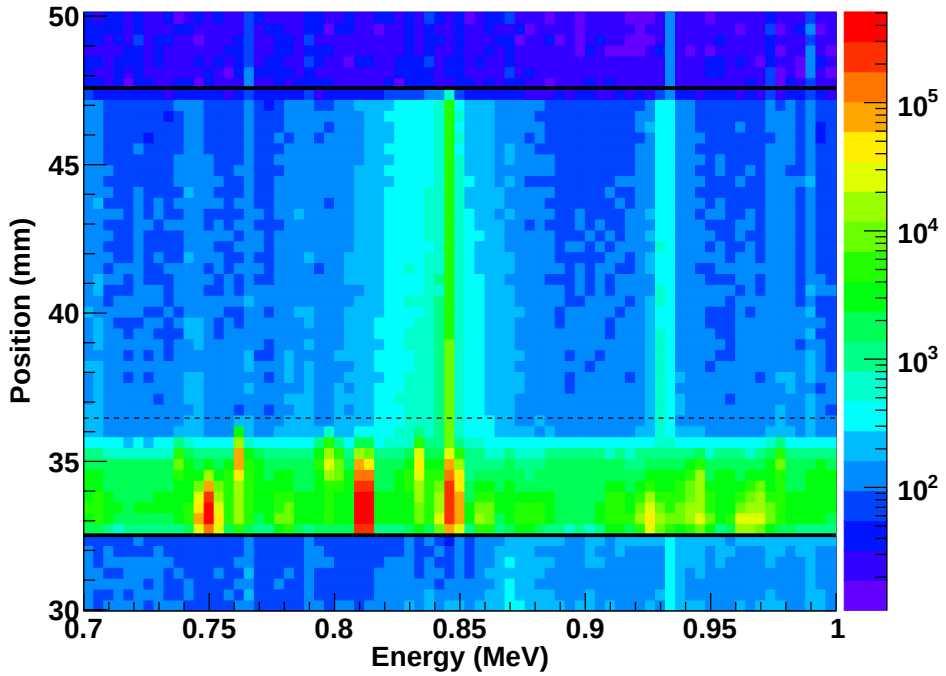

Figure 4.17: Geant4 simulated PG energy versus depth in a magnetite target placed inside a water phantom and irradiated with a proton beam of 66.5 MeV. Emission is maximum before the BP, indicated with a dash line.

Figure 4.18 shows the projection of the intensity plot obtained in figure 4.17, using a 3 mm cut, for four different positions: at the beginning of the target (fig. 4.18a), in the BP (located at 36.46, and shown in fig. 4.18b), past the BP (fig. 4.18c) and at the end of the target (fig. 4.18d). We can observe that initially the gamma-ray with highest intensity is the 812 keV, but as we approach the BP region the 847 keV dominates. If we collimate past the BP region, the only visible peak of the spectra will be the 847 keV. Hence, for experimental purposes, we know that when we align our target with the collimator system we should always detect the 847 keV gamma-ray, and the intensity will change based on the positioning of the target with respect to the collimators. Due to the cross section dependence, other gamma-rays, such as the 0.74 MeV gamma-ray, will only be visible at the beginning of the target, when their intensity is maximum.

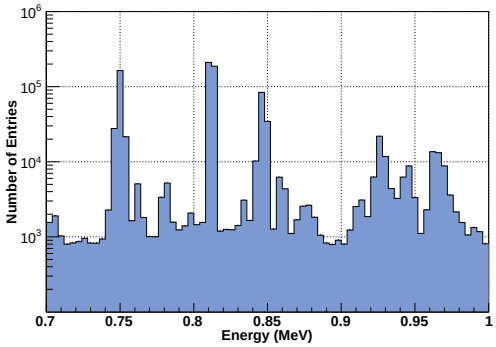

(a) Collimated at 32.7 mm

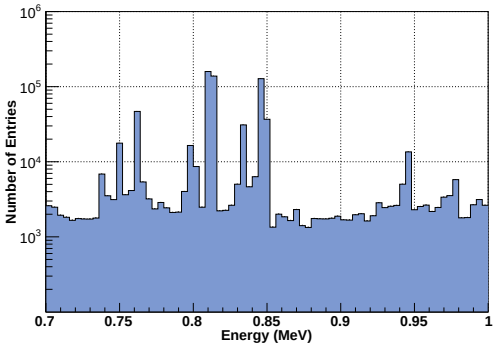

(b) Collimated at 34.5 mm

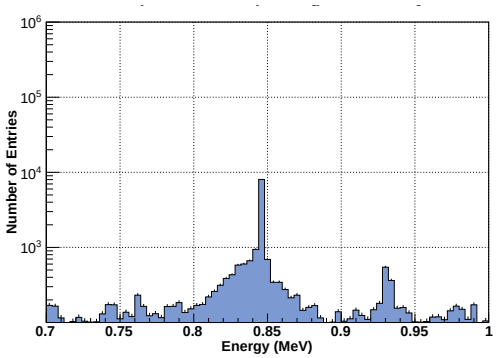

(c) Collimated at 36.4 mm

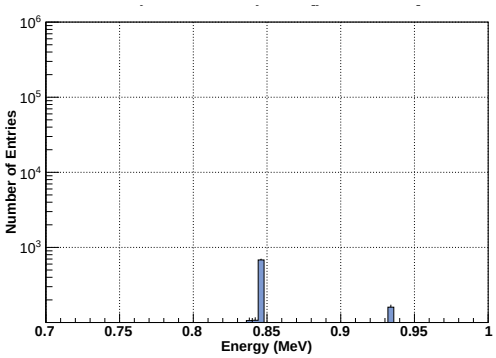

(d) Collimated at 37.4 mm

Figure 4.18: Projection of the intensity profile from figure 4.17 for different collimated positions. The uncertainties in x and y are too small to be visible, 0.1 mm and $\leq$2500 counts respectively. For clarification, the size of the collimated window is indicated in the x axis for each of the points.

The variation in intensity that we have seen before can be used to draw conclusions concerning the range. If we integrate the projected gamma-rays for the different peaks, we can analyse the trend the intensity follows. These results, for the different reaction channels and characteristic gamma-rays, can be seen in figure 4.19. We observe that, that, in all the cases thereafter, the number of counts increases smoothly until the region before the BP and then decreases.

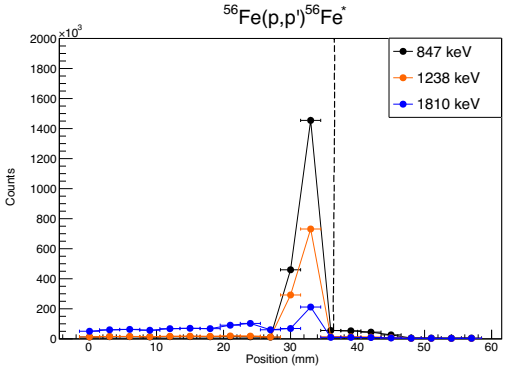

(a) Gamma-ray intensities as a function of the depth for protons on ^{56}Fe.

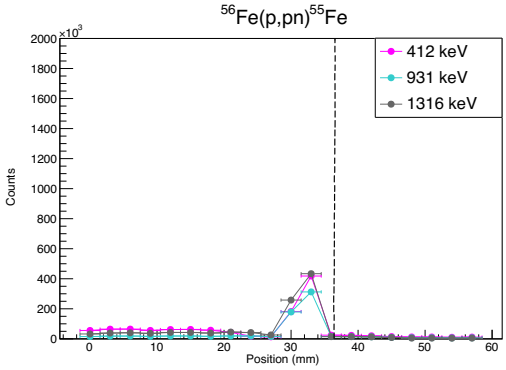

(b) Gamma-ray intensities as a function of depth for a neutron knockout reaction producing ^{55}Fe.

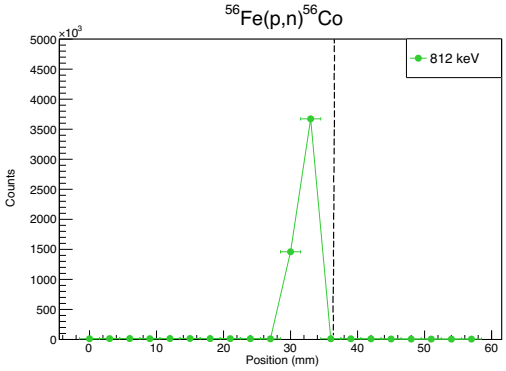

(c) Gamma-ray intensity as a function of the depth for charge exchange reaction populating the first excited state in ^{56}Co.

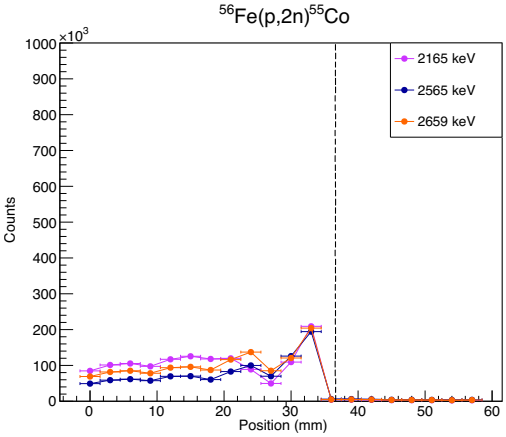

(d) Gamma-ray intensities as a function of depth for a two neutron knockout reaction producing ^{55}Co.

Figure 4.19: Projection of the intensity profile for different collimator positions for the unsegmented magnetite target. The uncertainties in x and y are too small to be visible, 0.1 mm and $\leq$2500 counts respectively. For clarification, the size of the collimated window is indicated in the x axis for each of the points.

Figure 4.19 also shows that all the PG from a single reaction mechanism follow the same trend, however between different reactions the depth in which the PG emission is maximum changes. This is due to the difference of the cross sections for each of the processes: the reactions that reach the maximum cross-sections at higher energies will peak well before those that reach the maximum at lower energies, as the energy of the protons is reduced along the depth of the phantom. Determining where the emission of PG is maximum will allow us to study the position of the BP. The results obtained for a target with lower magnetite concentration still show positive results, that agree well with the segmented target.

4.7 Summary

Initially, the position of the BP for different beam energies in a water phantom was studied to validate the code. The target composition was then changed to pure magnetite, in order to study the reduction in the BP position. The concentration of magnetite in the target was implemented with values between 0% and 100% to study the effect this material has in the dose, and the different DEF were calculated. These results showed that with the experimental targets we designed, decribed in chapter 3, the expected dose enhancement is in the range of 12.6% for the continuous target and between 12.6% and 24.2% for the segmented target.

After testing the physics of the simulation with generic targets, the experimental geometry was implemented. The dimensions and materials of targets and detectors were simulated to replicate the experimental set-up. Resolution of both detectors was implemented and analysed with a ^{60}Co source, where we observe that HPGe will differentiate better between different PG, due to its excellent energy resolution.

The characteristic PG from magnetite were studied, and associated to their corresponding transitions. The yield per proton was calculated, showing that the 847 keV gamma-ray is emitted with the highest intensity, as expected from literature. The resolution study was applied to determine if the distinguish-ability between the characteristic PGs can be observed in the experimental set-up. Results show that the HPGe will differentiate these peaks, while for the CLLB many of the peaks will coalesce into a broader peak.

Finally, the intensity profile was studied separately for the segmented and continuous targets. In both cases we observe how the emission of PG changes along the depth of the target, and how the behaviour of the gammas, originating from different transitions, differ. The obtained results agree well with the tabulated cross-section obtained from *TENDL* [51], as those gamma-rays, emerging from transitions that peak at higher energies, will have a maximum PG emission before those whose maximum cross section is reached at lower energies, since the protons slow down in the phantom. The effect of different collimation slit widths was also studied in the segmented target, proving that choosing a suitable window for the collimators will be key for the data acquired during the experiment.

Chapter 5

In-beam experiment with the CLLB

In this chapter, we introduce the set-up and methods for the two experiments performed with the CLLB scintillator detector. The experiments took place at the University of Birmingham and KVI-CART, with energy beams of 38 MeV and 66.5 MeV, respectively. The low energy beam is rarely applied in clinical cases, but it is ideal to study the characteristic PGs emitted from the proton irradiation of magnetite, as most cross sections of interest of ^{56}Fe peak between 10 and 25 MeV. The medium beam energy is used in clinic for treatments of superficial tumours, such as ocular melanomas. The results obtained using a magnetite target with 5% concentration and a water target are presented.

The aim of both experiments is to determine if characteristic gamma-rays emitted from the NPs target can be detected with a single CLLB detector, and to characterise the detector performance at two different beam energies. The secondary goal is to calculate the ratio of the water and the magnetite material to determine if it follows a trend that can be used to draw conclusions on the position of the BP region.

5.1 In beam experiment at 38 MeV

The experiment was performed in the MC40 cyclotron facility at the University of Birmingham [108]. The proton beam had an energy of 38 MeV and intensity of 10^8–10^9 protons per second. The beam was pulsed at a radio frequency of 26 MHz, corresponding to a period of approximately 38.46 ns. The beam spot size was $\sigma \approx 2$ mm, which is comparable to the one applied in clinical treatments.

5.1.1 Methods

Three targets were irradiated during the experiment: the 5% concentration iron NPs target, the water phantom and the PMMA target, described in chapter 3. All three targets were placed on the moving platform, to scan the emitted PG at different depths.

The CLLB detector, of radius 1.5 inches, was placed behind two identical lead blocks that created a single collimation slit of (3.5±0.5) mm. The blocks were placed 12.7 cm away from the beam line, and the CLLB detector was placed immediately behind the collimation slit, as shown schematically in figure 5.1. The collimation system was used to guarantee that the measured PGs are the ones emitted perpendicularly to the beam line. Simultaneously, a plastic scintillator was placed at the beginning of the beam line to monitor the incoming structure and timing of the protons. Both detectors were individually connected to the CAEN digitiser DT5730. Coupling the CLLB detector with the plastic counter in coincidence mode will allow us to reject the background and neutron-induced noise. A picture of the real experimental set-up obtained during the DAQ process can be seen in figure 5.2.

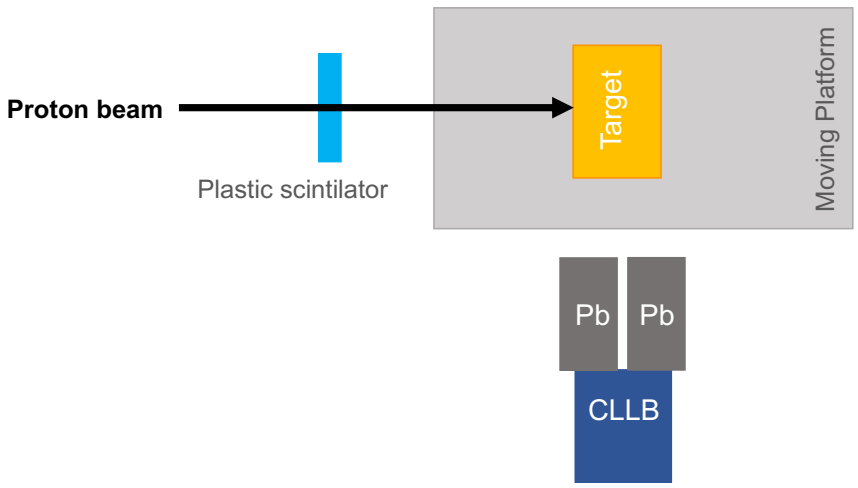

Figure 5.1: Schematic drawing of the experimental set-up used at the University of Birmingham for the irradiation with a proton beam of 38 MeV (top view, not in scale).

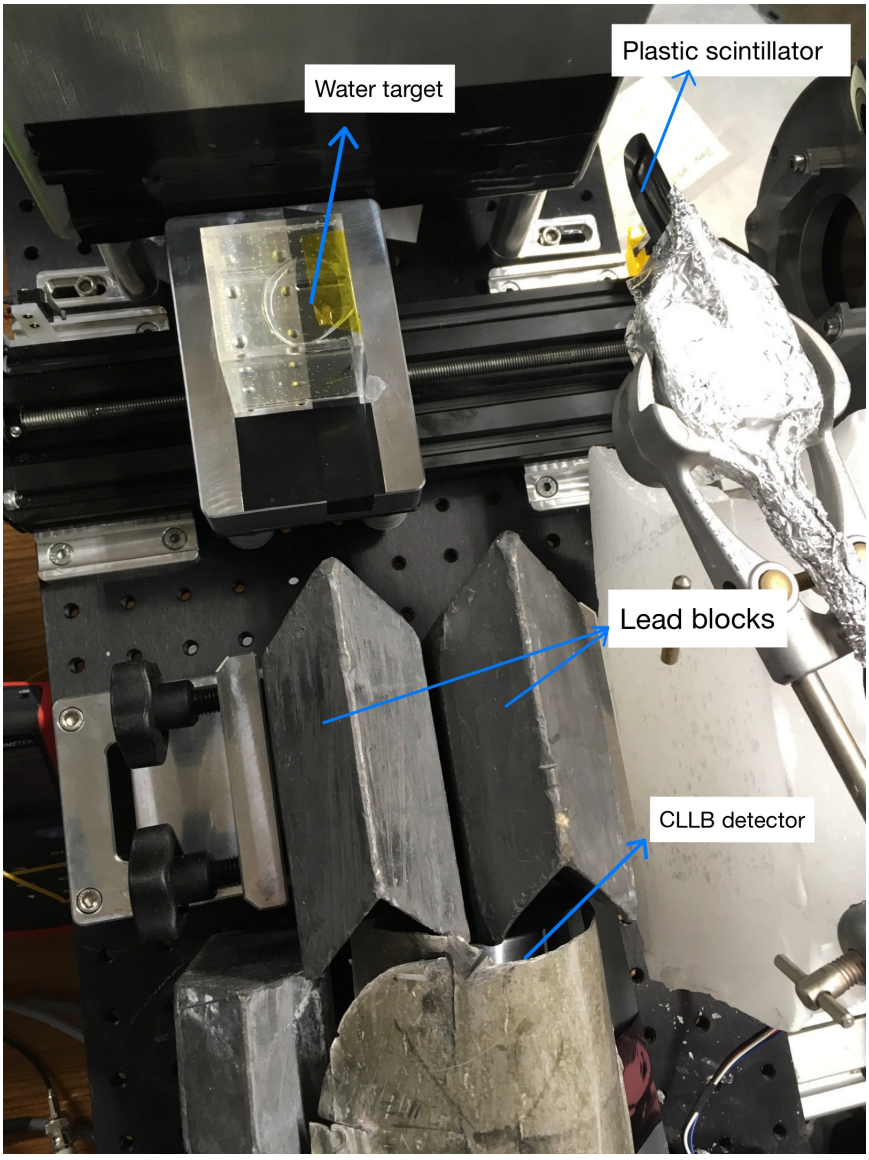

Figure 5.2: Experimental set-up used at the University of Birmingham for the irradiation with a proton beam of 38 MeV (top view, beam comes from the right hand side)

The CLLB detector was initially calibrated with two radioactive sources: ^{22}Na (with γ decays of 511 and 1275 keV) and ^{24}Na (with γ decays at 1358 and 2754 keV). The uncalibrated energy spectra of both radioactive sources can be seen in figure 5.3, where the peaks are labelled. Due to the threshold applied during the experiment, the 511 keV gamma ray is not visible, and therefore can not be used for calibration. In the same figure, we can observe two more gamma-rays, at energies 1732 keV and 2243 keV, that correspond to the single and double escape of the 2754 keV gamma-ray from ^{24}Na.

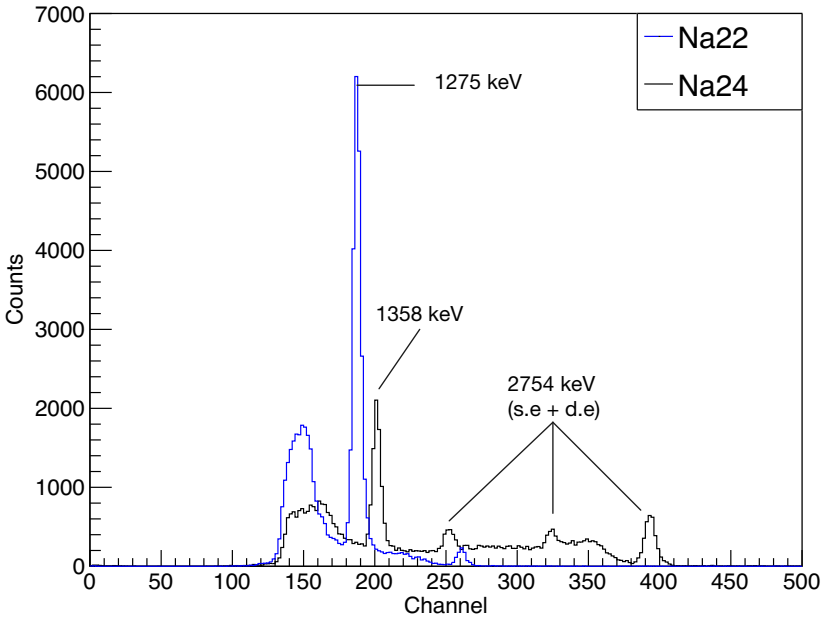

Figure 5.3: Uncalibrated energy spectra from ^{22}Na and ^{24}Na detected in the CLLB.

The CLLB detector is a dual gamma-neutron detector, therefore, to discriminate the neutrons the DPP algorithm has to be implemented during the experiment is PSD. This algorithm allows for the separation of gammas and neutrons, based on the different decay times of both particles, as discussed in section 3.4.1. To apply the PSD algorithms we measured the energies with two different windows: a short one (EnergyShort) and a long one (Energy). Plotting a function of the two in a 2D histogram will allow us to separate the neutrons from the gammas, as shown in figure 5.4. A comparison of the measured energies of the secondary particles emitted after the irradiation of a water target can be seen in figure 5.5, with and without applying PSD. There is no reduction in the number of gammas detected, because the neutron induced noise is minimum. However, we observe that the thermal neutron-induced

peak is completely removed after the discrimination. When the neutron peak is eliminated, we observe a gamma-ray with an energy of 3.42 MeV, which corresponds to the double escape peak of the gamma line of interest $^{16}O(p,x)^{12}C$ at 4.44 MeV.

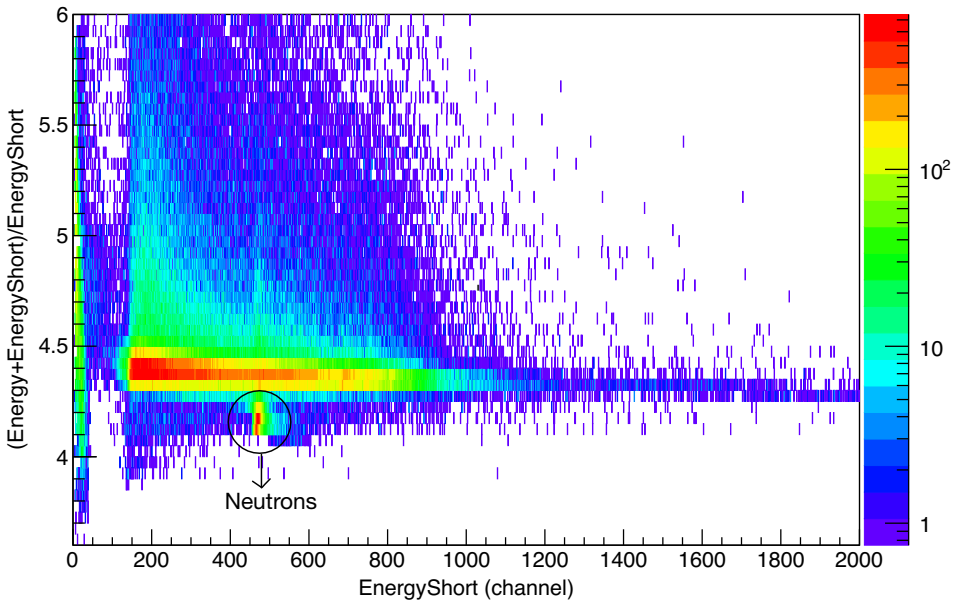

Figure 5.4: Pulse shape discrimination ratio obtained with the CLLB for a 38 MeV proton beam. Two regions are clearly differentiated for neutrons and gamma rays.

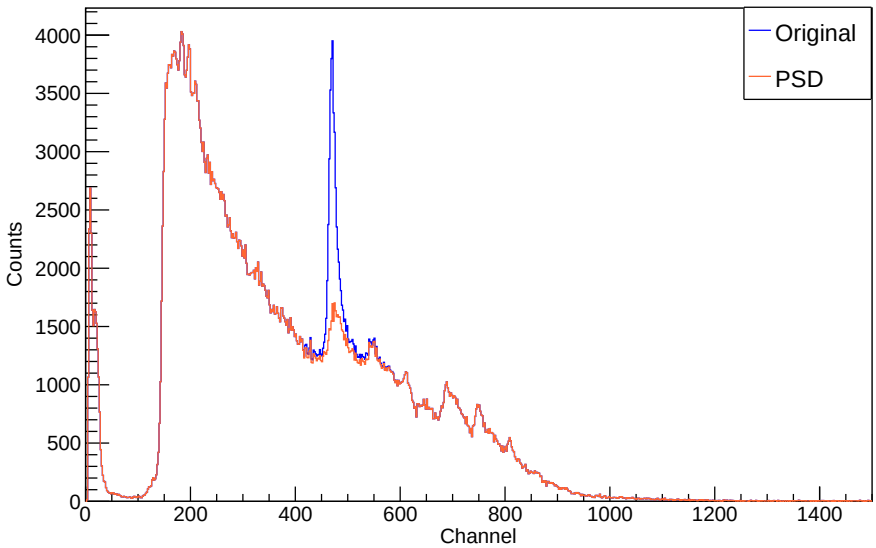

Figure 5.5: Uncalibrated spectrum from a water phantom irradiated with a proton beam of 38 MeV with and without PSD. The neutron thermal peak is clearly visible at channel $\approx$ 500.

5.1.2 PGs in the CLLB

The neutron cut will be applied to all the runs in order to study the emission of PGs in the different target media. Figure 5.6 shows the uncalibrated PG energy histograms for the three target materials: water, PMMA and magnetite. The gamma lines from the reactions of interest, ^{16}O(p,pα)^{12}C at 4.44 MeV and ^{16}O(p,p')^{16}O at 6.13 MeV, are indicated. The three runs have been acquired at the same depth in the target, and they are normalised to the total integrated charge. We observe that the maximum emission of gammas at 4.44 MeV comes from the PMMA target, as it has a carbon component that is not present in the other two materials, so the PG will not only be emitted from ^{16}O(p,pα)^{12}C, but also from the inelastic scattering of Carbon ^{12}C(p,p')^{12}C. On the contrary, the intensity of the 6.13 MeV PG is maximum in the water target. These results are expected, as the oxygen concentration is much higher in water. The emission of PGs at this energy is significantly higher for magnetite compared to PMMA, which can be explained with the material's composition: the magnetite NPs are diluted in water, therefore the oxygen concentration is higher for the NPs target.

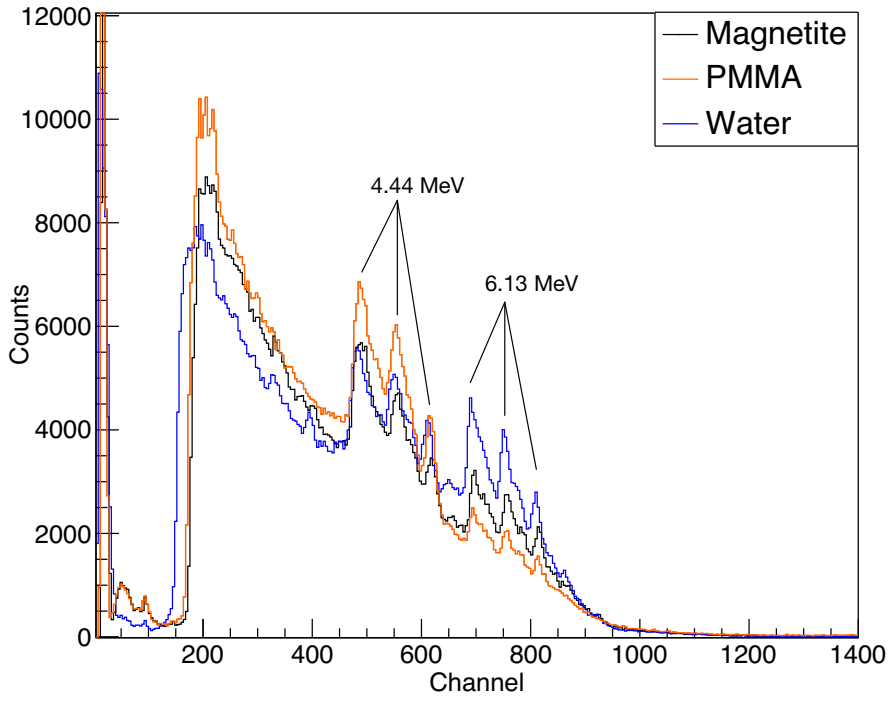

Figure 5.6: Uncalibrated energy spectra for the magnetite, PMMA and water targets for a beam energy of 38 MeV. Each spectrum has six characteristic peaks with its energies labelled.

The PG emission is enhanced for different materials at different energies. Comparing the three materials we observe that for low energies (below 3 MeV) the PG emission is enhanced for magnetite and PMMA, while in medium energies (between 3 MeV and 5 MeV) the enhancement only occurs on the PMMA target. In the high energy region, the enhancement is only visible in the water target. To study the regions separately, the histograms shown in figure 5.6 must be calibrated. After the calibration, the enhancement can then be calculated numerically, by dividing the histograms of magnetite and PMMA by water, and applying a coarse binning. The experimental results can be seen in figure 5.7, where the value of the ratio changes for the different energy regions and target materials. These results suggest that the ratio can be used for range verification purposes.

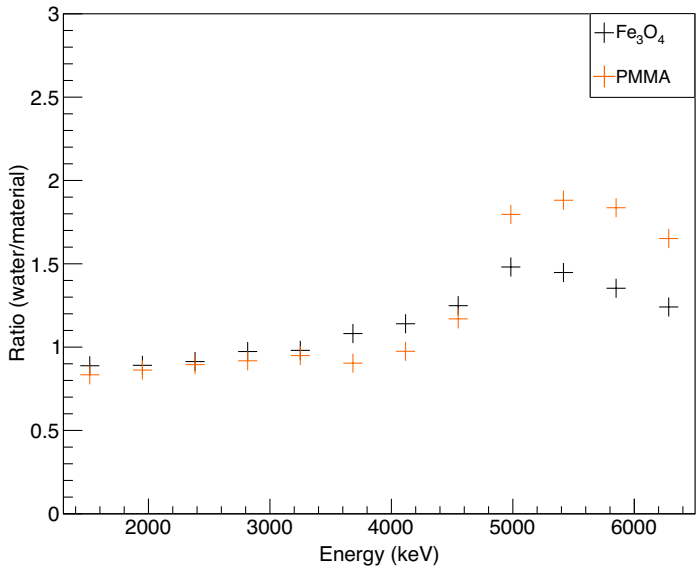

Figure 5.7: PGs intensity ratio of two histograms H_2O/Fe_3O_4 and H_2O/PMMA obtained with a coarse energy binning.

While this method does not determine the precise position of the BP, it is a good indication to determine if a certain tissue or material has been irradiated in comparison to water. The low energy resolution and statistics do not affect the results and, even without resolving any peaks, we can determine if the tumour has been irradiated or not. This can be applied to real-time beam monitoring during the treatment: in vivo measurement of the PG emission from ^{16}O must be performed and, depending on the material, the value of the ratio must reach a certain value. If the ratio is outside the tolerance limits, it indicates that the BP is located in a different tissue, and therefore the irradiated region is not the tumoural area.

After these results, the analysis will focus on the detection of characteristic PG from the magnetite NPs target. All the runs shown in figure 5.6 were obtained with a threshold of 210 least significant bit (lsb), that corresponds to approximately 1000 keV. This value is too high to detect characteristic PGs from iron, so we lowered it to 400 keV (60 lsb). Figure 5.8 shows the magnetite spectra for the same position of the collimator with two different thresholds. We can observe that the structures created in the high threshold run in the region between 1 MeV and 1.5 MeV, are artefacts and not characteristic PGs. However, in the low threshold runs there are several structures that are related to the magnetite target.

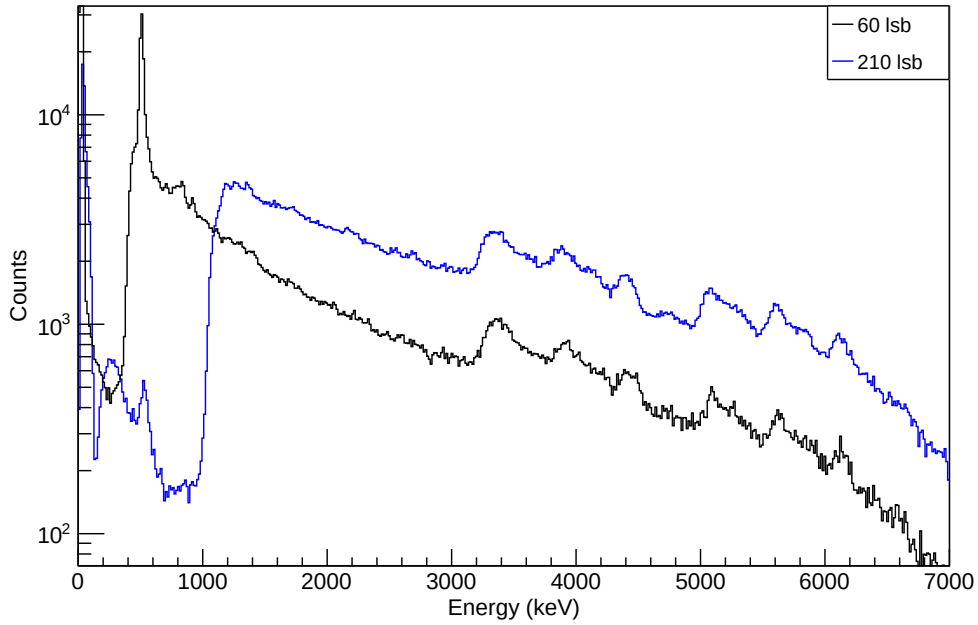

Figure 5.8: Calibrated energy spectra from a proton irradiated magnetite target for two different thresholds (60lsb and 210 lsb), acquired with the CLLB detector. The runs are not normalised to the total integrated charge.

To study the characteristic magnetite structures in the region of interest we obtain the energy spectra at two different collimator positions: 8 mm into the target and 12 mm. Each of these measurements needs to be corrected to obtain the absolute position, considering the plastic thickness of the front side of the box ($z_{container}$=2.8 mm) and the thickness of the plastic scintillator ($z_{plastic}$=1 mm). The absolute position, for which the runs have been acquired, can be calculated with equation 5.1.

$$z_{abs} = z_{collim} + z_{container} + z_{plastic} \tag{5.1}$$

The correction factor is 3.8 mm for this experiment, hence the experimental measurement were acquired in the region after the BP, as the range of a 38 MeV proton beam in water is 13.55 mm [109]. Hence, the statistics of the gamma-rays emitted are lower than desired, and from the simulation results we expect to only detect the PG at 847 keV. The obtained histograms for both positions can be seen in figure 5.9, where we observe similar structures for the two runs, as they correspond to the same region (past the BP).

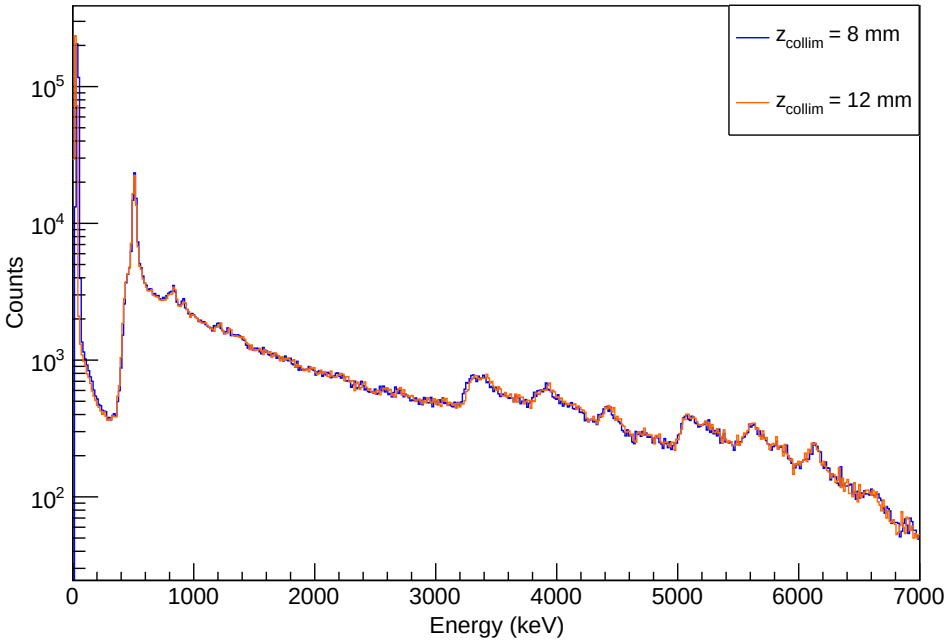

Figure 5.9: Calibrated PG energy spectra from a magnetite target with the collimators placed at two different positions: 8 mm (blue) and 12 mm (orange).

To confirm that the PGs detected are characteristic from the target, and not background related, we subtract the run in the furthest position from the BP to the one with the collimators in the closer position. This subtraction will eliminate all the background components, showing only the PGs originating due to the proton irradiation of the target. Figure 5.10 shows the subtraction of the runs, where we can observe a clear peak structure between 800 keV and 900 keV. To determine the peak energy, it is fitted with a Gaussian function and the obtained centroid corresponds to 849(2) keV. This value agrees well with the value reported in the literature for the transition from the 2^+ to 0^+ ground state of ^{56}Fe [110]. The experimental result confirms that characteristic gamma-rays from a NPs target can be detected during the proton irradiation of the target.

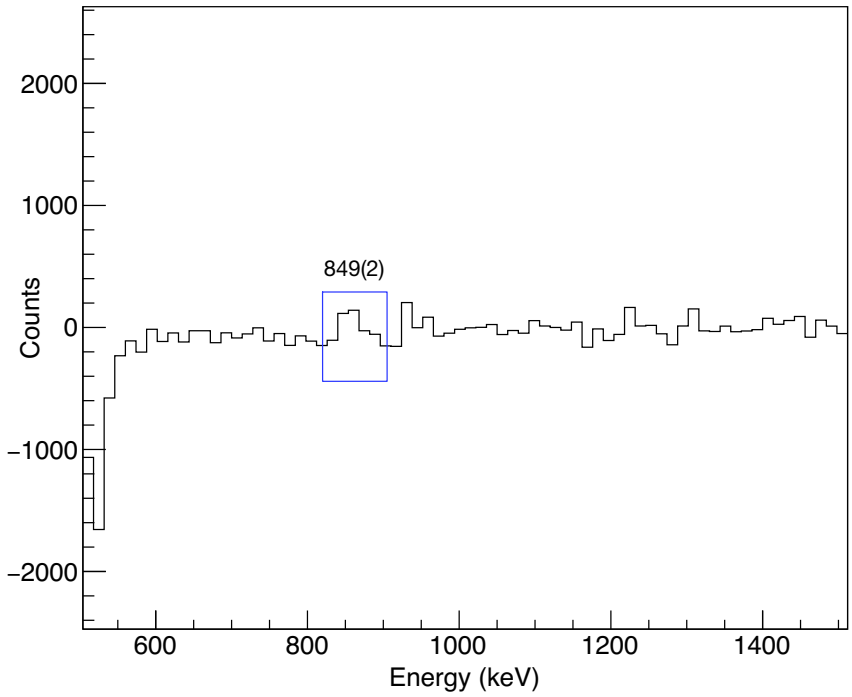

Figure 5.10: Subtracted spectrum of the magnetite target irradiated with a proton beam of 38 MeV. A clear structure is identified at 849(2) keV, that corresponds to the $2^+ \rightarrow 0^+$ transition from ^{56}Fe with an energy of 847 keV.

5.1.3 Conclusions

This subsection illustrated the experimental set-up, methods and results for the in-beam experiment at the University of Birmingham, using a proton beam of 38 MeV. The energy of the beam is ideal for studying the production of characteristic proton-induced gamma rays in different targets. The experimental set-up was initially tested with well-known targets, such as water and PMMA. Thereafter, the in-house designed magnetite target was placed in a moving platform and irradiated, and the gamma-ray energy spectrum was measured with the CLLB at different target positions. After comparing the spectra of the three materials we observe that the ratio of emission relies on the concentration of certain elements in the media. The yield of PGs at the characteristic 4.44 MeV and 6.13 MeV vary for PMMA, water and magnetite, and therefore this result could determine which material has been irradiated. This method can be applied for in vivo measuring of the range and will help to determine if the material in which the BP is located is the desired one, based on the ratio obtained at

different energies.

The detection of characteristic PGs from magnetite is the second part of the experiment. Due to the limited beam time, only two runs with the appropriate threshold were acquired. The interference of the plastic scintillator and front of the target modified the absolute depth that the protons reached in the target, and the measured positions correspond to the region after the BP. As expected from the simulation, in this region the emission of characteristic gammas is reduced to one single gamma, at 847 keV. After performing the subtraction of the two runs to eliminate the background, we detected a gamma-ray transition corresponding to an energy of 849(2) keV, which agrees well with the currently accepted value of 847 keV for the $2^+ \rightarrow 0^+$ transition in ^{56}Fe. This result confirms the initial idea that a NPs target can be used as a gamma emitter for range verification in proton therapy.

5.2 In-beam experiment at 66.5 MeV

The second experiment took place at KVI-Center for Advanced Radiation Technology (KVI-CART), in Netherlands. The cyclotron at this facility reaches higher energies, so the experiment can be performed in conditions closer to those applied in clinic. The aim of this experiment is to detect characteristic gamma-rays emitted from the NPs target placed in a water phantom, to emulate human-body environmental conditions.

5.2.1 Methods

The beam was pulsed at a radio frequency of 25 MHz, corresponding to a period of 40 ns. The intensity of the beam was 10^9 protons per second, and all the measurements took place in a two minute window, so a total of 1.2×10^{11} protons irradiated the targets in each run. The energy of the beam was 66.5 MeV, which is a clinically suitable energy.

The detection system is similar to that used in Birmingham, and a schematic diagram depicting the setup can be seen in figure 5.11. The phantom configuration varies to adapt the targets to a higher beam energy, as the range of the protons increases with the energy. For this reason, and due to its dimensions, the magnetite target needs to be placed inside a water phantom, so the protons slow down in the water and completely stop inside the NPs target for a maximum gamma-ray emission.

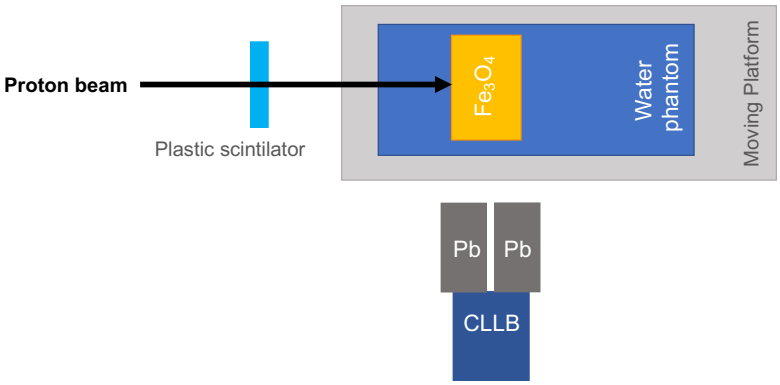

Figure 5.11: Schematic drawing of the experimental setup used at KVI-CART for the irradiation with a proton beam of 66.5 MeV (top view, not in scale).

The CLLB detector was collimated with two lead blocks separated by 3 mm. The blocks are placed 12 cm away from the beam line and perpendicular to the beam. Both targets will be placed in the linear moving platform, in order to evaluate the intensity of the detected PGs from the nanoparticles target for different collimated regions, before, during and after the BP. A picture of the setup used during the experiment is shown in figure 5.12.

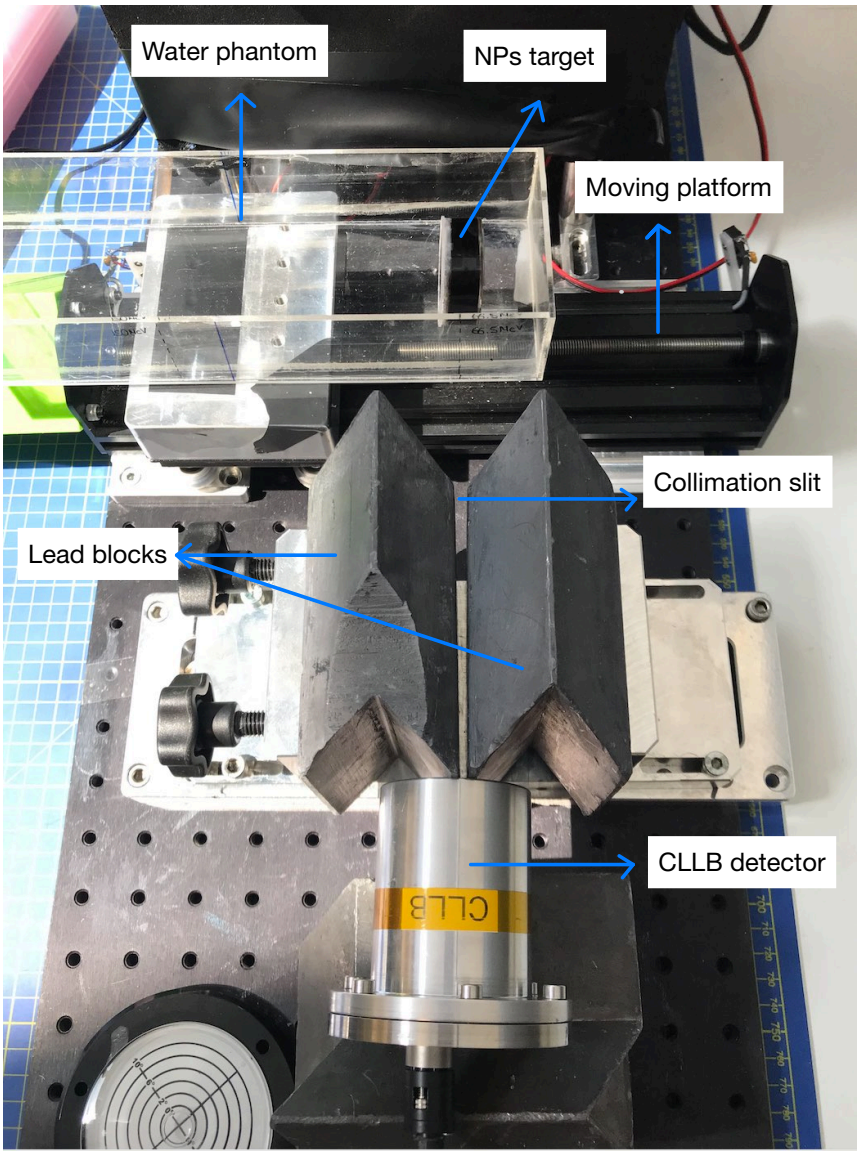

Figure 5.12: Experimental set-up used during the beam irradiation at KVI-CART with a proton beam of 66.5 MeV. The picture was taken before the experiment, and the separation between the different elements does not correspond to the actual dimensions during the beam irradiation.

In this section, the experimental results that were obtained for a proton beam of 66.5 MeV are presented. Before starting the irradiation of the targets, the gamma-ray energy spectra of two radioactive sources, ^{137}Cs and ^{152}Eu, placed together was obtained with the 1.5 inch CLLB detector. The first peak, at 662 keV corresponds to the ^{137}Cs source, while the five remaining have their origin in the ^{152}Eu source. Each of the peaks will be fitted with a Gaussian function plus a linear function for background, as shown on figure 5.13 for the ^{137}Cs photopeak. Each of the obtained centroids will then be associated to the well-known energies to obtain a second degree calibration polynomial. The polynomial obtained for the CLLB in this experiment is shown in equation 5.2, where we observe that the response of the CLLB is almost linear and has an offset of 10.52 keV, which agrees well with previous calibrations of the detector.

$$E\ (keV) = 0.001877x^2 + 7.155x + 10.52 \tag{5.2}$$

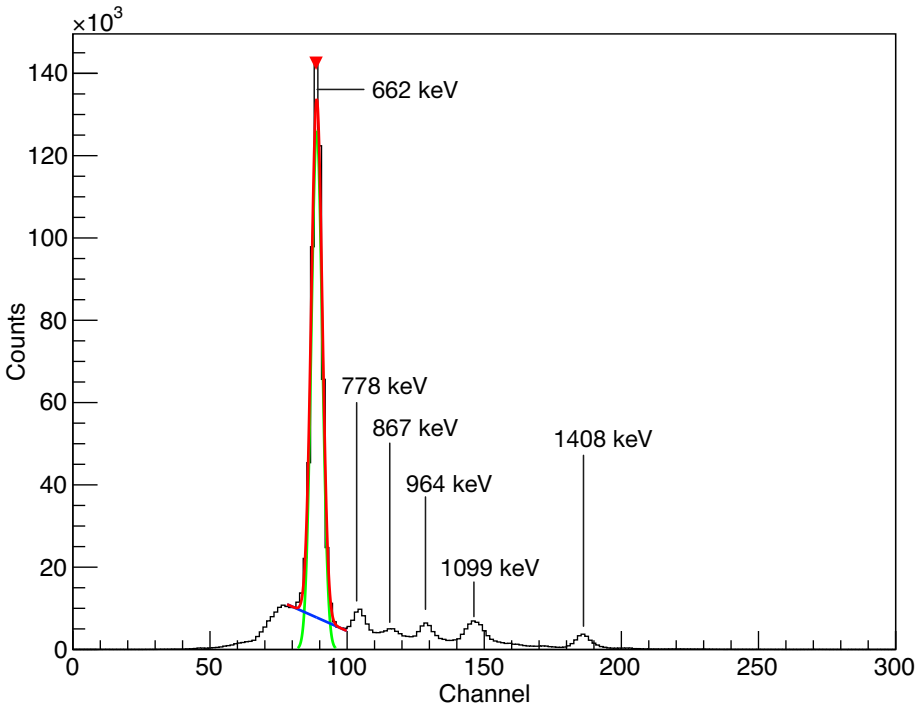

Figure 5.13: Uncalibrated energy spectrum from ^{137}Cs and ^{152}Eu obtained with the CLLB with all the peaks labelled. The energy peak at 662 keV peak is fitted to a Gaussian function (green) plus a linear function (blue). The final fitting function will be the sum of the two, and is shown in red.

Once the calibration polynomial has been obtained, we apply it to all the runs acquired during the experiment to determine the energy of the PGs detected with the set-up. Figure 5.14 shows that there is a shifting between the runs: the later they are acquired with respect to the calibration sources (measured at the beginning of the experiment) the more they shift towards lower energies. This shifting in the spectra is due to the instability of the temperature through out the experiment, that affects the SiPM performance, as its noise increases with the temperature. The drift between the different runs can be modelled by analysing the shifting of the neutron peak with time, and calculating a correction coefficient based on the neutron peak shifting. The correction coefficient is calculated as a function of the centroid position of the neutron peak for the first run when t=0 ($\mu_0^{neutron}$), and the centroid position of the run of study at a certain time t ($\mu_t^{neutron}$), as shown in equation 5.3. Figure 5.15 shows the correction coefficient versus time for the experiment, where we can appreciate that the trend is relatively smooth, due to a progressive variation of the temperature in the experiment room.

$$corr(t) = 1 - \frac{\mu_0^{neutron} - \mu_t^{neutron}}{\mu_t^{neutron}} \tag{5.3}$$

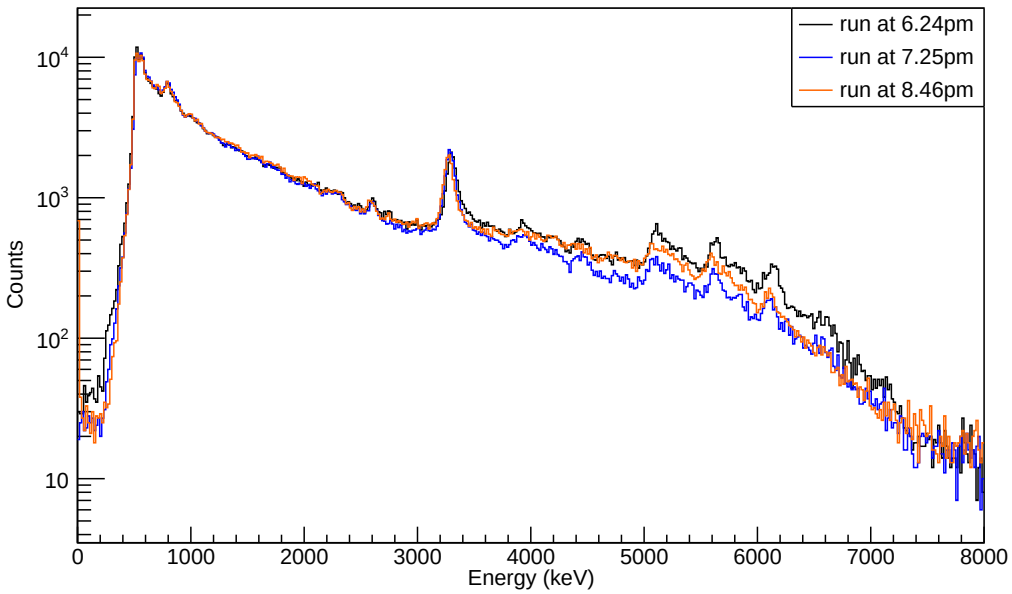

Figure 5.14: Calibrated energy spectrum from CLLB detector for different times and collimator positions. A shift between the runs is observed.

Figure 5.16 shows the difference in the position of the neutron peak, before and after applying the correction, and compares it with the initial run. We observe that the correction is needed to align the different spectra accurately, and this is crucial for obtaining an accurate energy of the characteristic PGs.

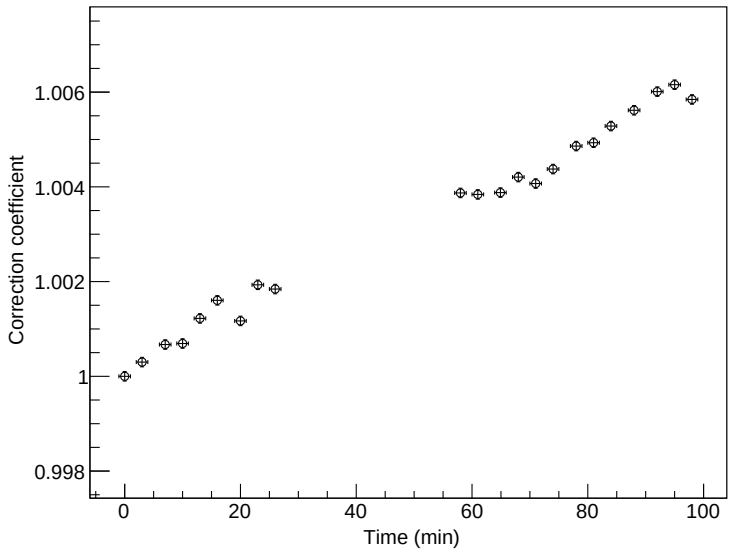

Figure 5.15: Correction coefficient versus time for the 66.5 MeV proton beam experiment, obtained with the neutron peak.

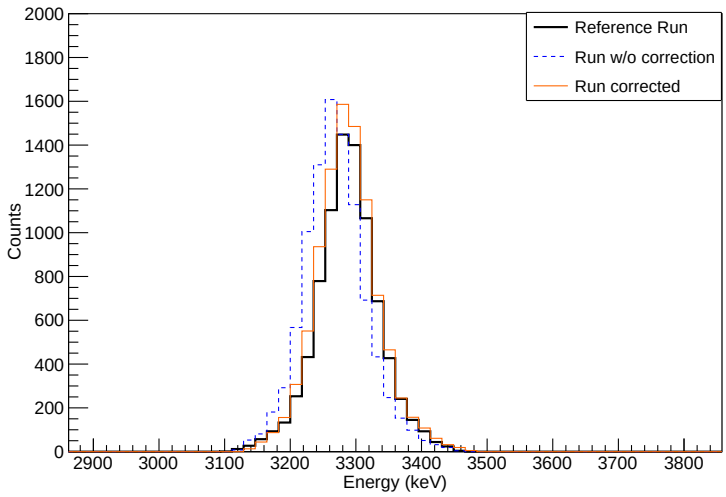

Figure 5.16: Neutron peak positions for the reference run (black), and a different run, with (orange) and without (blue dashed line) applying the correction factor.

Once the correction factor has been applied to all the runs, and all the checks with the neutron peak have been made, we proceed to suppress this structure. The pulse processing algorithm was again PSD, therefore we can apply restrictions to the obtained spectra in order to eliminate the thermal neutrons peak. Following the same procedure that we used in section 5.1.1, we obtain the 2D histogram of the energy function with two different gates to differentiate the gamma ray and neutron contributions. Figure 5.17 shows the two well differentiated regions for neutrons and gamma rays. The neutron region has a longer tail than in the Birmingham experiment, because there are more neutrons contributing to the specta. Once PSD has been applied we observe that the thermal neutron-induced peak is removed, and the background is slightly reduced, as shown in figure 5.18, where we can observe the calibrated energy histograms of secondary particles emitted from the magnetite target placed in water with and without PSD.

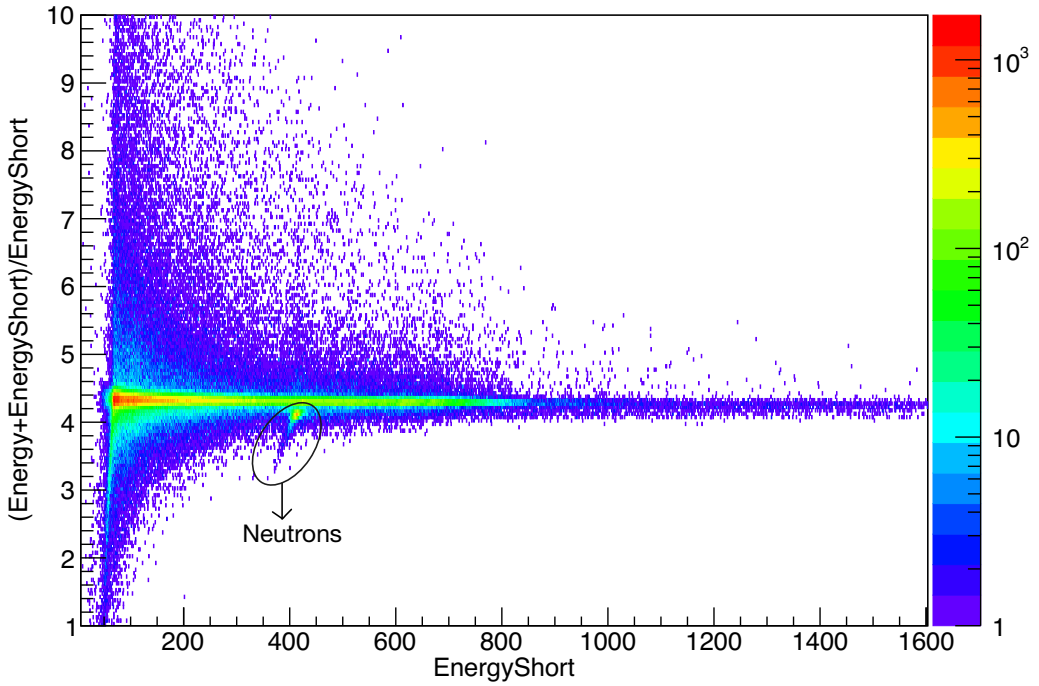

Figure 5.17: Pulse shape discrimination ratio obtained with the CLLB for a 66.5 MeV proton beam. Two regions are clearly differentiated for neutrons and gamma rays.

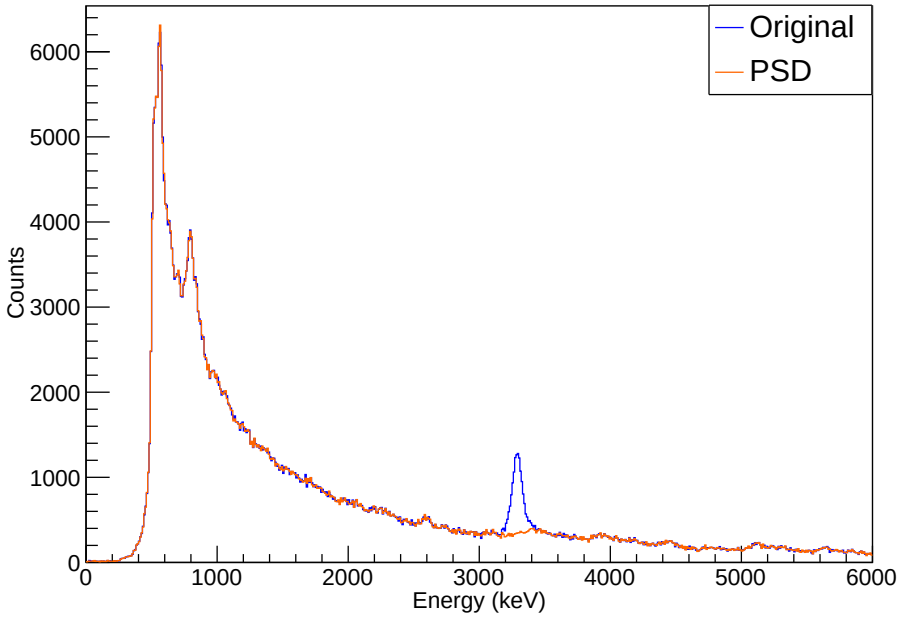

Figure 5.18: Calibrated energy spectrum from a magnetite target placed in water with (orange) and without (blue) PSD. The characteristic neutron peak is obvious.

5.2.2 PG in the CLLB

After the calibration and discrimination of the CLLB detector, the runs for the different targets can be analysed. Two sets of data were taken for each position of the collimators: one with the water target alone and one with the magnetite target placed inside the phantom. A comparison of the two spectra can be seen in figure 5.19, where both materials show the six characteristic gamma-rays from water, as expected due to the presence of a large water phantom in both of them. These come from the transitions ^{16}O(p,x)^{12}C, at 4.44 MeV, and ^{16}O(p,p')^{16}O at 6.13 MeV. Due to the small size of the detector, their single and double escape are also detected. There is also a peak in both materials at an energy of 2.6 MeV, whose origin relies on the lead blocks placed for collimation purposes and therefore is not characteristic from the targets. There are two other structures in the low energy region (below 1 MeV) that are visible for both targets, and are not associated with any known transitions in the irradiated materials. Therefore we can considerate these structures as artefacts due to the threshold applied for the DAQ process.

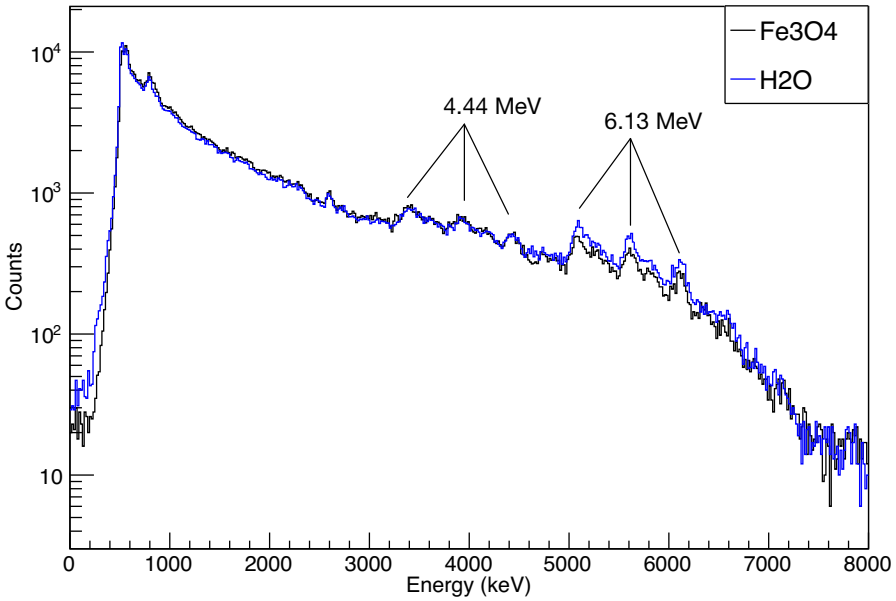

Figure 5.19: Experimental spectra for the water target and magnetite target placed in water irradiated with a proton beam of 66.5 MeV and obtained with the CLLB detector collimated at the same depth.

The figure above shows a difference in the intensity between the magnetite and the water histograms, especially for the 6.13 MeV PG. In the previous experiment we determined the ratio for two different materials, and such ratio provides conclusions on the irradiated material. After obtaining positive results in the previous experiment, we now want to perform the same ratio analysis, but only the magnetite material and for different positions of the collimators: before, during and after the BP. The obtained results for the ratio of the water phantom divided by the magnetite, for different positions are plotted in figure 5.20. At low energies (below 4 MeV) the ratio is smaller than the unit, and after that it increases because the emission of characteristic PGs is higher in water than in magnetite. We observe that for the high energy region (above 5 MeV), the ratio is minimal for the region beyond the BP. The region between 5 MeV and 6.13 MeV shows a higher value for the region before the BP, and this agrees well with the expected results, as the collimation window creates a FoV in which not only the PGs in the middle of the collimator are detected, but also the ones emmited within the FoV. This explains that before the BP the FoV includes more PG than in the BP, as the FoV also contains the section beyond the BP in which the emission of gammas is null.

These experimental results can be used not only to draw conclusions on the material that has been irradiated, but as an indicator of the region irradiated and if it corresponds to the BP or not. The variation of the ratio in different regions proves again that, with a very low resolution and low statistics set-up we can obtain an indicator of whether the BP region has been reached, hence we can deduce if the NPs have been hit or not, allowing us to stop the beam helping to determine the position of the BP and if the tumour has been irradiated during the proton therapy treatment.

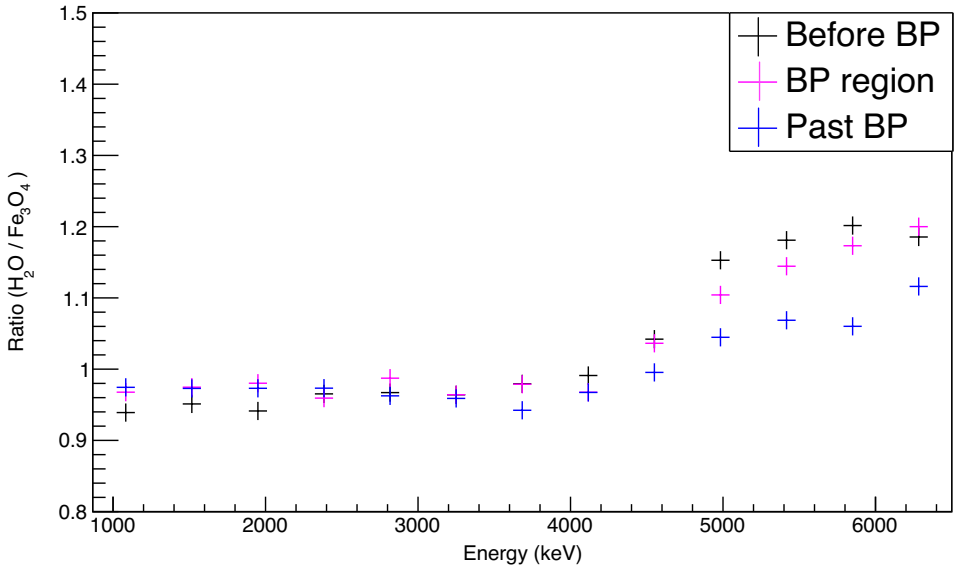

Figure 5.20: PGs intensity ratio of H_2O/Fe_3O_4 for three different positions: before, after and during the BP with a coarse energy binning.

After the analysis of the ratio, the goal is to obtain the emitted gamma-rays from the radiomarker target. In order to do so, we need to clear the spectrum and eliminate the previously mentioned structures that are not characteristic of the irradiated material, as well as any other structures that do not come from the magnetite target and any background contribution. Hence, the subtraction of the two runs must be performed. The resulting subtracted histogram for the BP position run is shown in figure 5.21, where we observe a significant structure in the 800 keV region. After applying a Gaussian function to fit the structure, we obtain that its centroid corresponds to an energy of 845(2) keV. This value agrees well with previous experimental results, and corresponds to the currently accepted value for the transition from the first excited state to the ground state of ^{56}Fe.

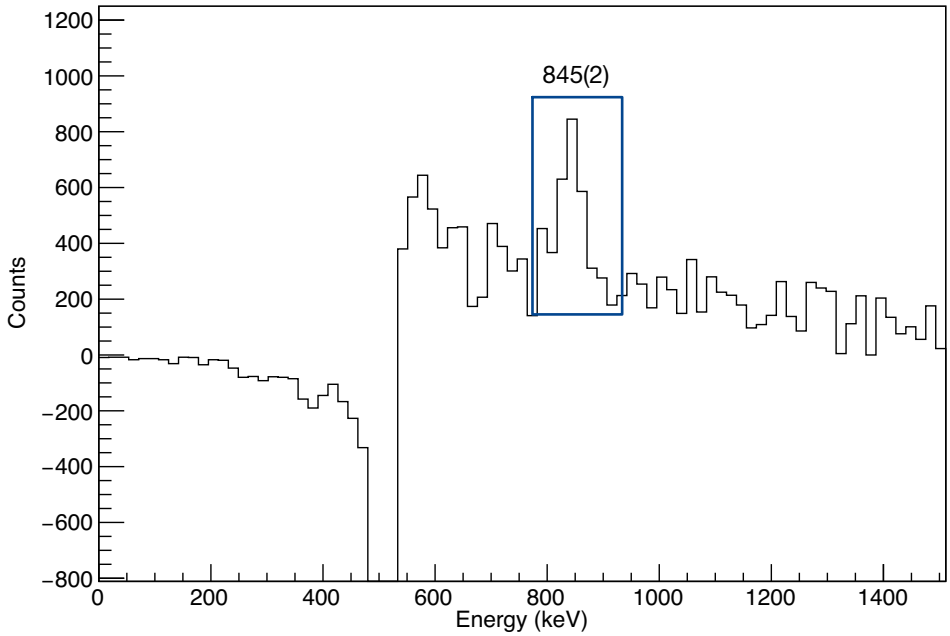

Figure 5.21: Subtraction of the magnetite placed in water and water only experimental PG histograms to determine characteristic gammas from the magnetite target. A clear structure is visible at 845(2) keV.

The same analysis is performed for all the acquired runs, before and after the BP, and we can confirm that the 847 keV structure is visible in all of them. The number of counts obtained for each run can be seen in table 5.1, where we observe that the statistics of the peak are quite low. This explains why no other characteristic structures are visible in the spectrum. From the simulation results obtained in table 4.3, we know that the following PG with highest intensity is at 1238 keV, but its emission yield is 0.57 times the yield of the 847 keV. Therefore, the number of counts for the second most likely structure will be in the order of a thousand, and divided over a few bins the counts are too low to form a clear structure.

Position (mm)	**Counts in 847 keV**
36	2058
37	2162
38	1679
39	1557
43	731

Table 5.1: Number of counts for 847 keV PG obtained at different detector positions in a magnetite target irradiated with a 66.5 MeV proton beam.

To study how the number of each detected events changes depending on the position of the collimator, the subtraction for all the pair of runs we have obtained has been performed. Later on, the integration of the number of counts under the peak is calculated to determine how many PG are emitted at each position. The results obtained in table 5.1, have been plotted in figure 5.22, to show graphically how the number of counts varies with the position. The number of counts increases, reaching a maximum at 37 mm, which corresponds to the position before the Bragg Peak. The value then decreases, as predicted by the simulation, that is also plotted in figure 5.22. The variation in the number of counts between experiment and simulation is due to the perfect efficiency of the detectors in the simulation.

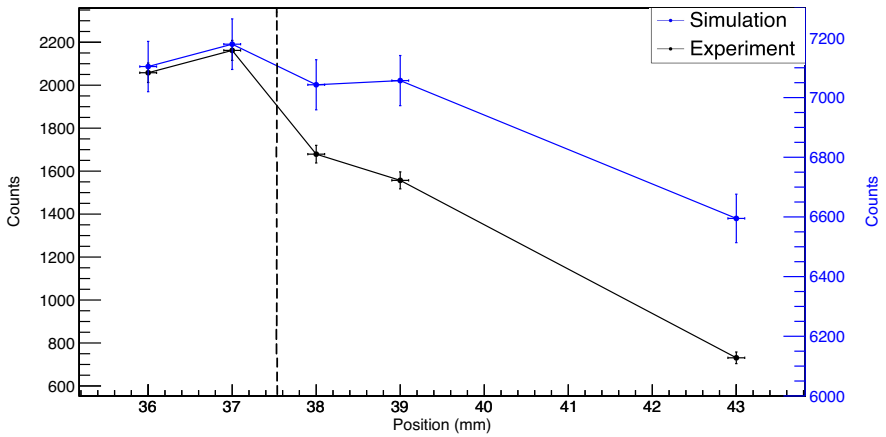

Figure 5.22: Integrated counts versus position for the PG detected at 845(2) keV after the subtraction of the magnetite plus water runs minus the water alone. The position of the BP is indicated with a dashed line.

The change in the counts versus the position shows that the positioning and perpendicular alignment of the collimation slit is key to obtaining good quality data. The experimental spectra for the magnetite placed in water, acquired at different placements of the collimation slit, can be seen in figure 5.23. This figure shows how the intensity of emission changes at different depths of the phantom. There is a significant change in the number of counts for the high energy PG originating after the interaction of the protons with the oxygen nuclei. The number of counts decreases proportionally to the distance of the collimators in the target, i.e counts are maximal at 34mm, when the FoV of the collimation slit comprises water and magnetite, and minimal at 43 mm, when the collimated region is exclusively magnetite. To study the behaviour of both PGs separately, we apply the same algorithms we used for the

847 keV: integrate the total number of counts for each of the runs and analyse the gradient.

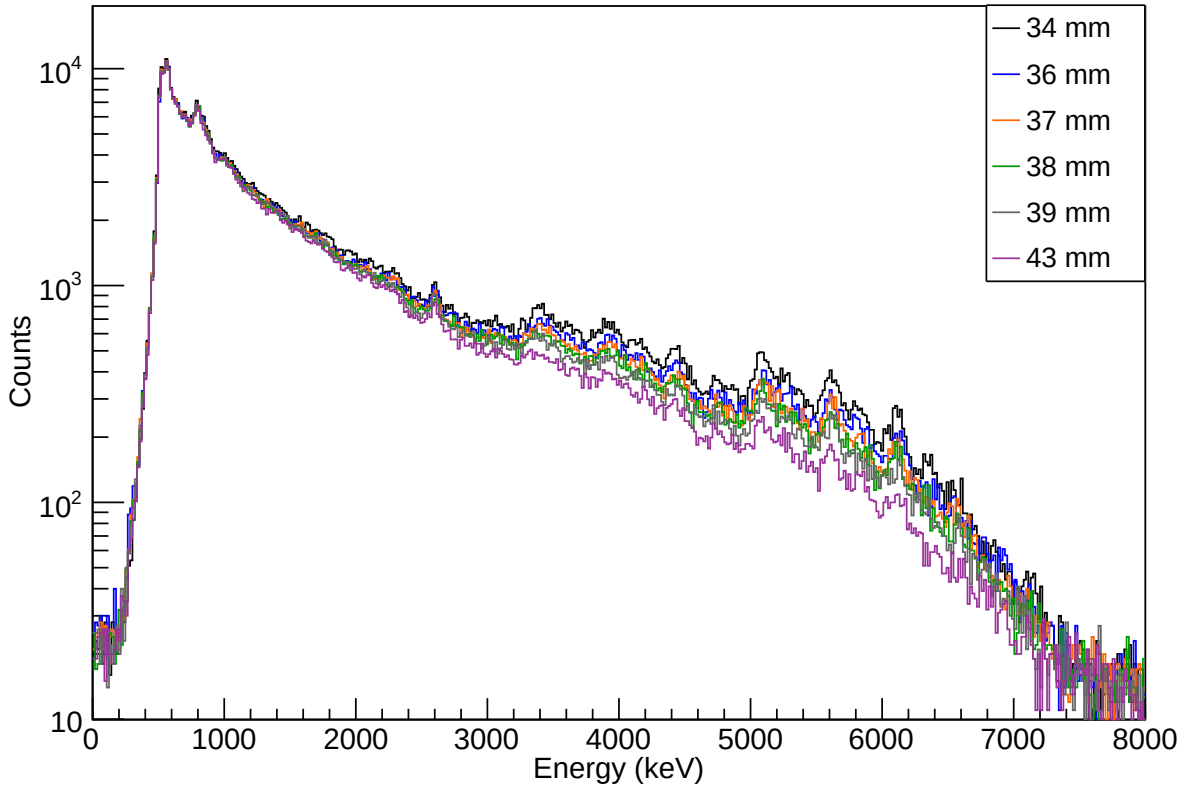

Figure 5.23: Experimental spectra for the magnetite target placed in water irradiated with a proton beam of 66.5 MeV and obtained with the CLLB detector collimated at different depths.

The experimental results of the integration for the gamma-rays at 4.44 MeV and 6.13 MeV can be observed in figure 5.24. In both cases, there is a reduction in the number of counts as we increase the position of the collimator. We also observe that the maximum corresponds to 34 mm, which is before the magnetite target. The change in trend, in comparison to the one obtained for the 847 keV (shown in figure 5.22), is easily explained by the fact that the magnetite target is placed inside a water phantom. This implies that the collimation window does not only allow PG from the magnetite to pass through, but also from the water. It is impossible for us to differentiate which characteristic gammas come from the oxygen component in the magnetite and which ones come from the water phantom, when we place the target in water. This also explains why the maximum number of counts is reached

far away from the BP, at 34mm, because in that region the collimation slit covers a wider region of the water target, and therefore the detected PGs are mostly emitted from oxygen in the water. The water phantom has a higher oxygen concentration, therefore the emission is higher. Simulated results are also represented in figure 5.24, where we observe a good agreement between experiment and simulation, confirming that for the characteristic PGs of water we can not establish a relation between maximum emission and number of PG detected.

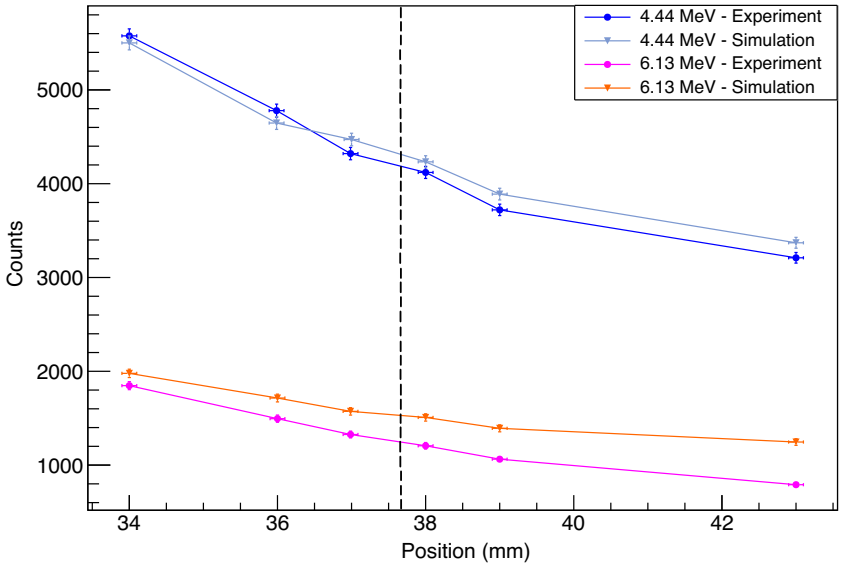

Figure 5.24: Comparison of experimental and simulated intensity of the 4.44 and 6.13 MeV PG (in counts) versus the position of the collimator window (in mm) for the gamma-rays originated after the proton irradiation of the magnetite target placed in water. The position of the BP is indicated with a dashed line.

To study the characteristic emission of 4.44 MeV and 6.13 MeV PGs from the oxygen component in the magnetite target, the target should be irradiated alone. Our experimental data was acquired with the magnetite placed inside the water phantom, therefore a subtraction of the water runs must be applied to the magnetite runs to show the characteristic trend of the PG emitted exclusively from the magnetite target. The experimental results, obtained after the subtraction, for the two gamma-rays are shown separately for each of the energies in figures 5.25 and figure 5.26, respectively.

Figure 5.25 shows the experimental counts for the 4.44 MeV PG, and a comparison with the simulated data. We can observe that the trend is similar for both: the number of counts increases, reaching a maximum before the BP position and then it decreases. The gradient in the number of counts is higher in the simulation, which can be explained with the alignment of the collimator. In the simulation, the detectors are aligned precisely at 90° with respect to the beam, but during the experiment the collimation window was aligned perpendicular to the target with the use of lasers, and so was the target with respect to the beam. The lack of mechanical devices for alignment can lead to small variations in the positioning angles, and therefore in the FoV. Due to this experimental uncertainty, and the width of the 4.44 MeV gamma-ray, it is impossible to determine experimentally the precise position in which the maximum number of counts are obtained for this energy, as a plateau is observed for the maximum yield between 37 and 38 mm. From the simulation, we observe that the maximum emission is obtained at 37 mm, which agrees with the experimental results.

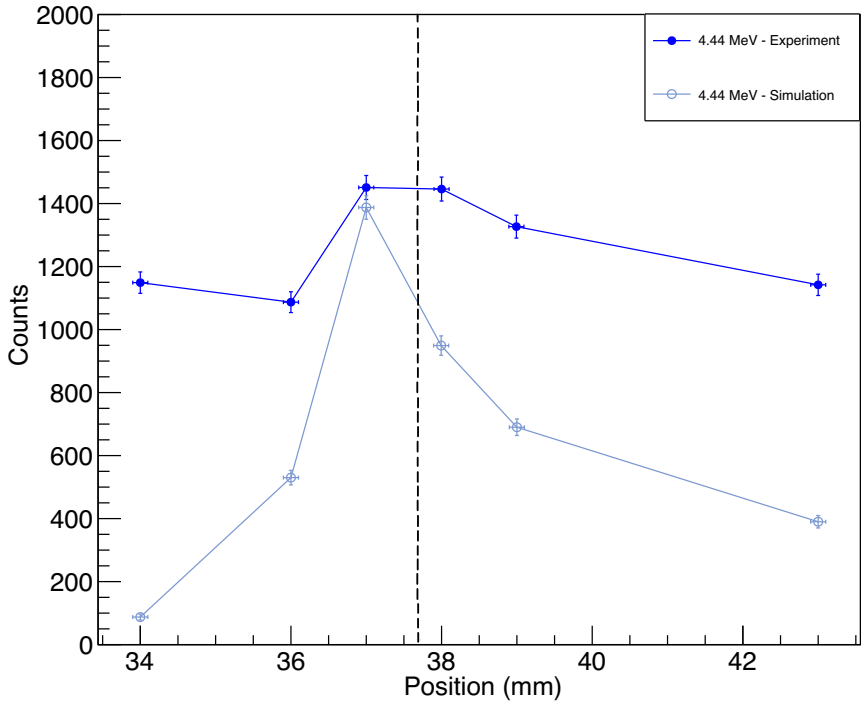

Figure 5.25: Experimental and simulated counts (scaled) versus collimator position for the PG detected at 4.44 MeV after the subtraction of the magnetite placed in water minus the water runs. The maximum emission for simulation is obtained at 37 mm and the BP is indicated with a dashed line.

The same analysis is performed for the 6.13 MeV PG, and the results for simulation and experiment are shown in figure 5.26. The trend of this figure aligns better with the expected results: the number of counts increase, reaching a maximum before the BP position, and then they decrease again. Due to the narrower structure of the 6.13 MeV, the effects of the FoV are not as notorious in this peak, showing a clear maximum emission point at 38 mm. This is 1 mm beyond the peak position obtained for the 4.44 MeV and for 847 keV, which is expected from the theory: while the inelastic scattering of ^{56}Fe peaks at 14 MeV, and the emission of 4.44 MeV via ^{16}O(p,p'α)^{12}C* peaks around 20 MeV, the mechanism responsible for the 6.13 MeV PG, the inelastic scattering of ^{16}O, peaks at a lower energy, and therefore the maximum emission of PG will take place deeper inside the the target, since the protons need to lose more energy through the interaction with the target material to reach the highest production energy that leads to maximum number of gamma-rays emitted.

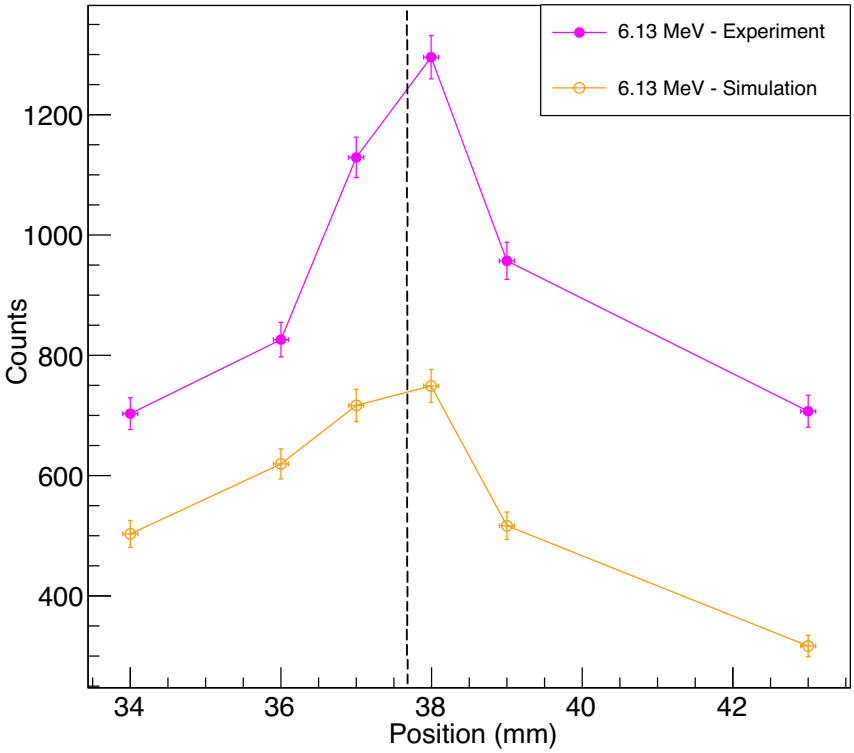

Figure 5.26: Experimental and simulated counts (scaled) versus collimator position for the PG detected at 6.13 MeV after the subtraction of the magnetite placed in water minus the water runs. The maximum emission is reached at 38 mm for experiment and simulation and the BP is indicated with a dashed line.

5.2.3 Conclusions

The experimental set-up, methods and results for the in-beam experiment at KVI-CART using a proton beam of 66.5 MeV have been introduced in this section. Due to the high energy of the beam, the magnetite target was placed inside a water phantom that slows down the protons in order to stop them in the middle of the magnetite target.

The ratio between the magnetite and water runs is performed, showing a ratio value that changes depending on the irradiated material and the position of the collimator. These results can be used to draw conclusion on which region has been irradiated, and determine if the BP has been reached or not.

To obtain characteristic results from the magnetite target, the subtraction of the runs with magnetite and water and with water alone, for the same positions, must be performed. Experimental results show a gamma peak 845(2) keV, that is consistent with the expected PG from inelastic scattering of ^{56}Fe at 847 keV. These results prove the efficiency of a NPs target as a PG emitter, showing that even when the concentration is low and they are placed inside a body-like environment, the emission will be detected. The statistics of the 847 keV peak is low, due to the low concentration of magnetite in the irradiated target. Considering that this is the most intense gamma-ray of all those emitted, it is expected that with the current set up the other characteristic PG emitted after the proton irradiation of the target are not detected.

Further analysis on the intensity of the counts for different collimator positions shows that the number of counts increases before the BP region, and decrease after for the 847 keV, as well as for the 4.44 MeV and 6.13 MeV. The position at which the emission is maximal directly correlates with the cross-section of the responsible process, as these processes that peak at higher energies will have a maximum emission earlier in the target than the ones which peak at lower energies. The experimental results were compared with the simulation, showing a strong agreement between the two.

5.3 Summary

This chapter illustrated the experimental set-up, methods and results for the two in-beam experiments with the CLLB dual scintillator. The first experiment took place at the University of Birmingham, with an energy beam of 38 MeV, and the second one at KVI-CART with a proton beam of 66.5 MeV. In both cases the magnetite target with a 5% magnetite NPs concentration diluted in water was placed on top of the moving platform and irradiated, but for the 66.5 MeV experiment it was placed inside a water phantom to emulate human body-like conditions and allow for the protons to stop inside the target.

In both experiments the characteristic PG at 847 keV, emitted from the inelastic scattering of ^{56}Fe, was detected. These results show the feasibility of NPs target as PG emitters, and therefore they can be used for range verification while simultaneously enhancing the dose. While the experimental results at 38 MeV only show the feasibility of the target as a PG emitter, the analysis of the 66.5 MeV results expand beyond this, showing that by measuring the PG profile at different depths we can obtain a clear trend in the number of counts versus the position which directly correlates with both the cross section of the responsible process and the range of the protons. The relation with the cross section can be seen when comparing PGs originating from different processes: those that have a maximum cross section at higher energies will emit a maximum number of gamma rays earlier than those whose cross-sections peak at low energies, as the energy of the beam is reduced with the depth. The experimental results obtained for 847 keV, 4.44 MeV and 6.13 MeV confirm this, and their comparison with the simulation provides a positive agreement. They will peak at different depths depending on their cross-sections, but all of them peak before the BP position.

The ratio of the magnetite to water runs was also performed in both cases, determining that the yield of PGs can be used to study which material has been irradiated, and if we are in the BP region, before of after. These results can be used, not to determine numerically the BP, but to experimentally determine when the irradiated tissue corresponds to the tumoural region, in which the NP are located and when we are irradiating healthy structures. The results can be used to determine when to stop the beam during therapy, reducing the irradiation of the healthy tissue.

The emission of characteristic PG from the magnetite NPs target will allow us to verify the range of the protons, as the number of counts in the characteristic PGs will change significantly with the position. This information can be used in order to stop the proton beam once the 847 keV is not detected, as this means the irradiated region does not correspond to the NP material that is accumulated in the tumour, and therefore healthy tissues are being irradiated.

The experimental results show that when NPs are accumulated in the tumoural region and a low resolution system is used, we can determine if the tissue irradiated corresponds to the tumour or not, based on the ratio of the different gamma rays. Furthermore, this system can be used to study the intensity variation of PGs, which correlate with the proton range.

Chapter 6

In-beam experiment with the HPGe

In this chapter we introduce the improved experimental set up, including a high resolution germanium detector, that was used for the in-beam experiment at the MC40 cyclotron facility at the University of Birmingham.

This experiment aims to characterise the HPGe detector performance for PGs and extend the experimental results, by detecting more characteristic gamma-rays from a radiomarker target. Segmented targets were used in order to precisely study the variation in the intensity of the gammas with the position of the collimators. The results obtained for a 36 MeV proton beam are then presented and compared to simulation.

6.1 Methods

The proton beam was pulsed at a radio frequency of 26 MHz, corresponding to a period of 38.5 ns. The beam energy was fixed at 36 MeV, while the beam current varied through the experiment, and was limited by the count rate of the detectors (10^9 protons/s).

A photograph of the experimental setup is shown in figure 6.1. In the center of the photograph, aligned with the beam is a moving platform in which the targets were placed during the experiment. On one side of the moving platform we placed a single-slit CLLB collimated system consisting of two lead blocks, situated 10.5 cm away from the beam line, forming a (3.0 $\pm$ 0.1) mm collimation slit. The CLLB detector is placed directly behind the collimation blocks to measure the PGs emitted perpendicular to the beam line. On the other side of the target, another (3.0 $\pm$ 0.1) mm collimation slit is created with two identical lead

blocks, placed at the end of the moving platform The HPGe detector is situated 12 cm away from the blocks, due to constraints of the support structure. Both detectors were connected to different channels of the DT5730 digitiser, discussed in chapter 3, and data was acquired using the PHA firmware, as the experiment was optimised for the HPGe detector.

Four different targets were placed on top of the moving platform: two segmented targets (one filled with magnetite and one with water), the long water phantom and the cubic PMMA target. The water and PMMA targets are used for calibration and testing of the detectors, as the energies of their emitted gamma-rays are well known. The magnetite target is irradiated to detect characteristic gamma-rays from the material and study their intensity profile.

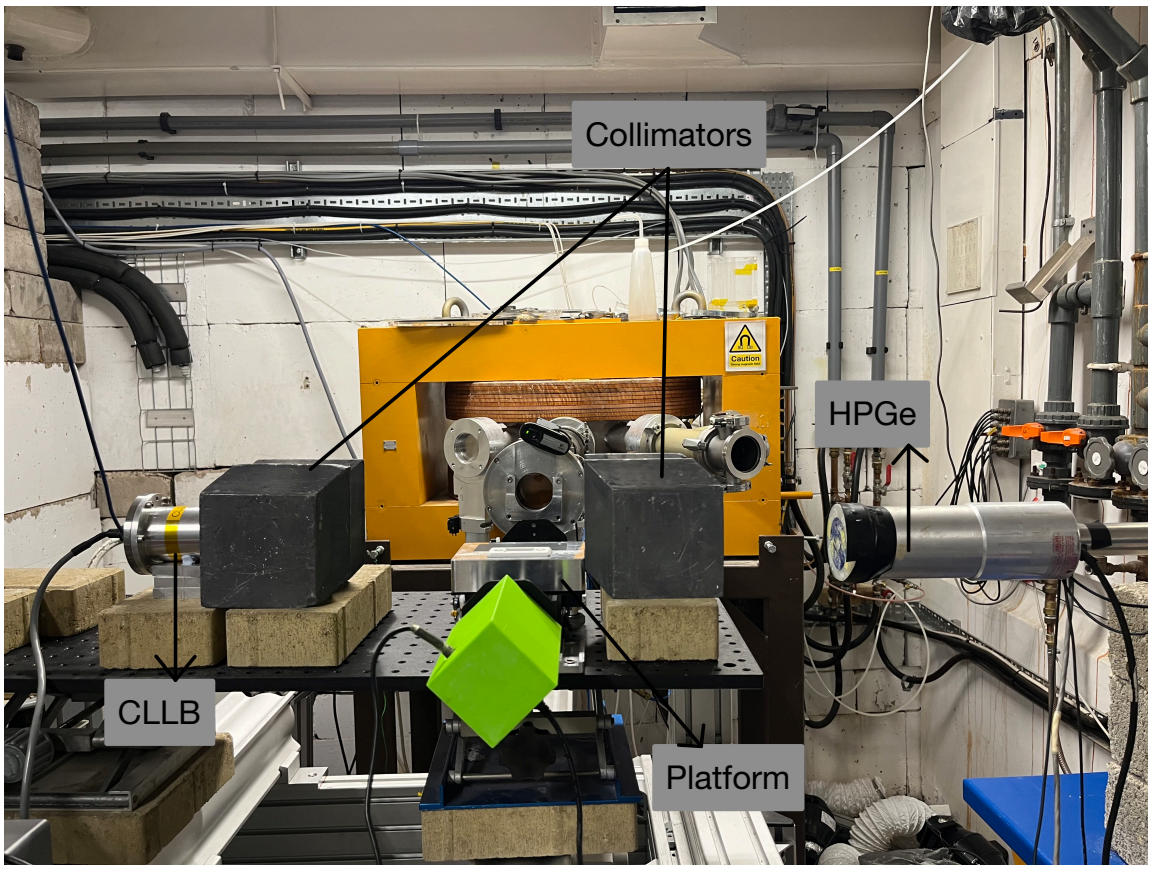

Figure 6.1: Front view of the experimental set up used during the beam irradiation at Birmingham University with a proton beam of 36 MeV. The main components are indicated.

The two detectors were simultaneously calibrated, by placing the radioactive sources in the centroid between the detectors. Three different radioactive sources were used to cover a wide energy range: ^{60}Co (γ decay at 1173 and 1332 keV), ^{137}Cs (γ decay at 662 keV) and ^{152}Eu (γ decay at 344, 779, 1085, 1112 and 1408 keV). The obtained spectra for the radioactive sources will be analysed separately for each detector.

The calibration histograms for the CLLB detector can be seen in figure 6.2. Due to the detector resolution, the gamma-rays at energies 1085 and 1112 keV cannot be separated in the energy histogram, and they merge into a single gamma of energy 1099 keV, as shown in figure 6.2. Each peak is associated to its corresponding energy, and the obtained function for the energy calibration is given by equation 6.1, where we observe that the second degree coefficient is small, compared to the others, due to the good linear response of the CLLB.

$$\mathrm{E}_{CLLB}\ (\mathrm{keV}) = 0.003856x^2 + 12.94x - 13.77 \tag{6.1}$$

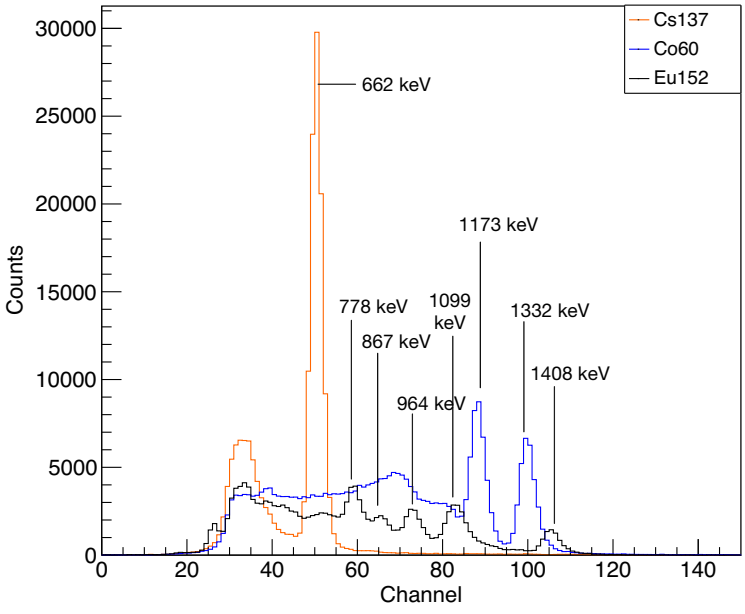

Figure 6.2: Uncalibrated energy spectrum from ^{60}Co, ^{137}Cs and ^{152}Eu obtained with the CLLB detector.

The uncalibrated spectra, acquired with the HPGe detector, can be seen in figure 6.3. We observe that the the peaks are narrower than the ones obtained for the CLLB, which is expected due to the better resolution of the detector. However, we can observe that all

the peaks are in a low ADC channel number, which is due to the sub-optimal adjustment of the coarse gain. The spectrum resolution does not reflect the detector's intrinsic energy resolution, as for HPGe a value of 0.25 keV/channel would be a suitable setting for the ADC, while in this experiment the value is approximately 11 keV/channel. This deteriorates the effective resolution of the detector in the acquired runs, and therefore the results presented here have this ADC-related limitation. Due to the insufficient ADC channels in the peaks, the calibration can not be performed with the fitting of a Gaussian function plus a linear background, as the entire Gaussian distribution often fits within one or two ADC channels. To overcome this limitation, an algorithm that reproduces Gaussian distributions, with different mean and sigma values will be created and applied for all the peaks that cover more than one bin. All the calculated Gaussian functions will produce a histogram that is then compared to the selected peak. The χ^2 function is calculated, and the values of the mean and sigma that minimise the deviation between the experimental and the simulated histograms will be used for the calibration. Figure 6.4(a) shows the 2D histogram that represents the χ^2 function with respect to the sigma and mean values, and it will allow to determine the optimal combination of parameters for each peak.

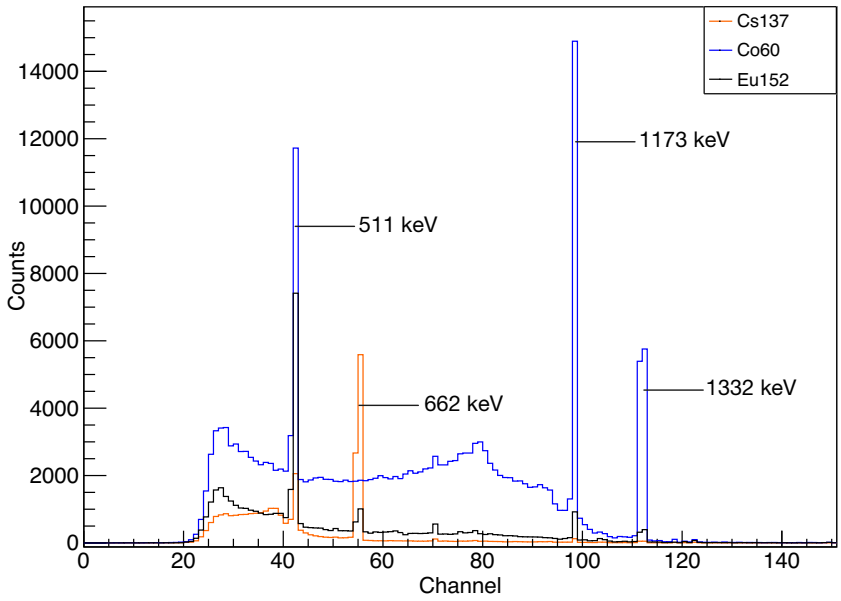

Figure 6.3: Uncalibrated energy spectrum from ^{60}Co, ^{137}Cs and ^{152}Eu detected in the HPGe.

Once the minimum χ^2 is determined, the values of the mean and sigma are fixed and the histogram is reproduced taking into consideration how many counts form the peak. A comparison between the reproduced and experimental histograms can be seen in figure 6.4b, where we observe a good agreement between the two.

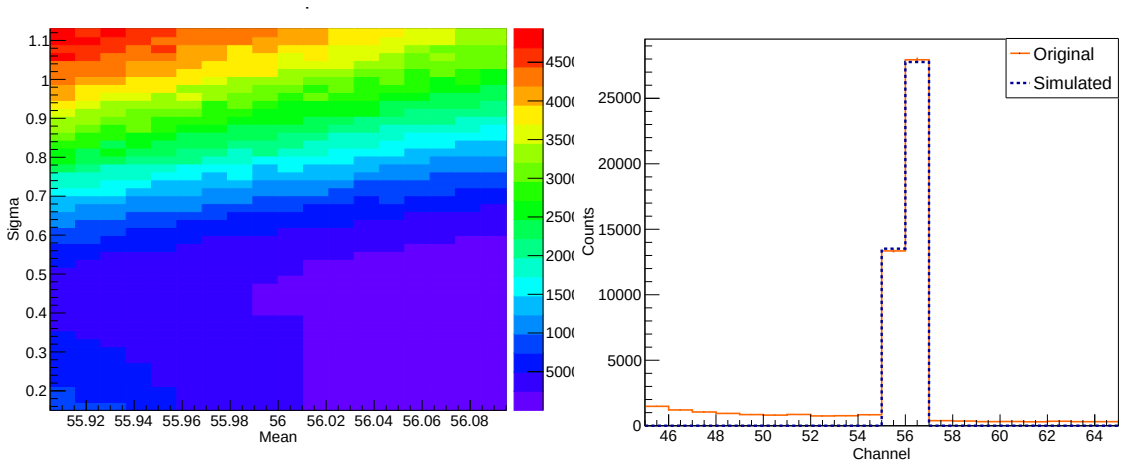

(a) (b)

Figure 6.4: (a) 2D plot of the deviation between the calculated Gaussian distribution and the experimental results for various mean and sigma values. (b) Calculated Gaussian distribution and comparison to the original data.

This method was repeated for all the peaks that spread over at least two bins. The extracted mean values will be used for an initial HPGe energy calibration, in which the channel number is proportional to the energy. The function, f(x), that gives the relation between the two can be seen in equation 6.2, where x corresponds to the channel number. After applying this initial calibration to the radioactive sources runs, a study of the quality of the approximation was performed. For this purpose, an analysis of the correlation between the tabulated energy and the energy obtained with this polynomial must be performed. The comparison, shown in figure 6.5, shows a direct correlation that can be fitted with a second degree polynomial, g(x), shown as a purple line. The equation for the second degree polynomial is given by equation 6.3, where we observe that the quadratic component is minimum.

$$\mathrm{f}\ (\mathrm{x}) = 11.78x \tag{6.2}$$

$$\mathrm{g(x)} = -6.218 \cdot 10^{-6}x^2 + 1.014x + 5.09 \tag{6.3}$$

The final calibration function for the HPGe detector is obtained as a composition of the two functions, as shown in equation 6.4. This final second degree polynomial constitutes the function for the energy calibration of the detector. This calibration function also shows a very small coefficient for the second degree component, due to the excellent linear response of the HPGe.

$$\mathrm{E}_{HPGe}\ (\mathrm{keV}) = f(x) \circ g(x) = -8.629 \cdot 10^{-4} x^2 + 11.945x + 5.09 \tag{6.4}$$

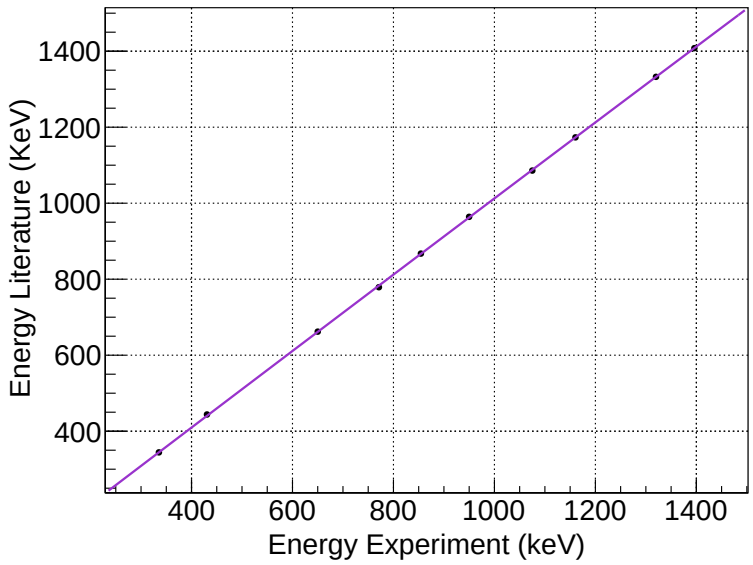

Figure 6.5: Energy of the calibration sources obtained during the experiment after applying a Gaussian modelling, versus energy of the sources in the literature.

After applying the energy calibration functions to both detectors (eq. 6.1 and 6.4, for the CLLB and HPGe, respectively), we can calculate the energy resolution at different energies. Table 6.1 shows the values obtained for four different energies. The CLLB resolution is slightly worse in comparison to the measurements acquired with the PSD firmware, in which a value of 6.02% was obtained for 662 keV. This relies on the fact that the DAQ and DPP algorithms were optimised for the HPGe detector. The HPGe resolution is affected by the compression of the spectra towards lower ADC channel numbers, due to the sub-optimal gain setting, reaching a value of 0.56% for 1332 keV in comparison to the 0.162% obtained during the initial testing of the detector with an analogue shaping amplifier and a multi-channel analyser. This deteriorates the quality of the in-beam spectra, but the results obtained with

this configuration, for the HPGe readout, still allows for a 5.8 times better distinguishability between gamma-rays than the one obtained with the CLLB detector.

Energy (keV)	**Resolution CLLB (%)**	**Resolution HPGe (%)**
662	6.55(2)	1.12(1)
779	5.02(1)	0.89(7)
1173	4.05 (3)	0.69(4)
1332	3.75(3)	0.56(3)

Table 6.1: Resolution values for the CLLB and HPGe detectors at different energies obtained with radioactive sources during the experiment.

6.2 PGs in the HPGe

The HPGe detector is implemented in the set-up with the objective of detecting more characteristic PGs, and discriminating between PGs close in energies. The experiment was optimised for this detector, and therefore PHA algorithms are applied for the data acquisition process.

From previous experiments, we know that the CLLB detector can handle beam intensities of 10^9 protons/s when placed behind the 3 mm single slit collimator [89], but it is required to test the response of the HPGe detector before acquiring data.

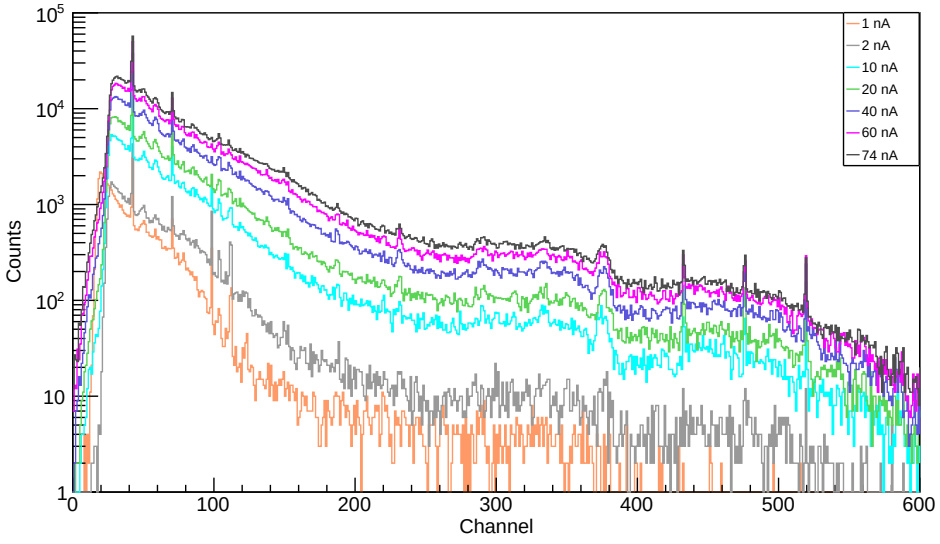

Figure 6.6: Uncalibrated energy spectra for different beam currents in the HPGe detector.

The detector response was tested by progressively increasing the beam current, between 0.5 nA and 74 nA. The detector response to different beam currents is shown in figure 6.6, where we observe a direct relation between the number of counts and the beam intensity.

While we observe a good spectrum for all the beam intensities, a compromise between the beam current and the capacity of the detectors must be reached in order to acquire good quality data. From the obtained histograms shown in figure 6.6, we can confirm that setting the beam current to 40 nA is adequate for our experiment, as it corresponds to an intensity of 1.6×10^9 protons/s, a value that can be handled by both detectors.

After determining a suitable beam current, the targets were alternated individually on top of the moving platform, placing each of them individually. Each target was irradiated for 3 minutes, with a total of 2.88×10^{11} protons impinged on them at a given position. A medium threshold was applied to exclude the background in the low energy region, removing the events at energies below 200 keV but retaining the important PGs. The obtained calibrated histograms, for the segmented targets, with the collimation slit placed in the BP region can be seen in figure 6.7, where we can observe that in the region below 2000 keV there are many characteristic gamma-rays that are only present in the magnetite runs, which agrees with the Geant4 simulation.

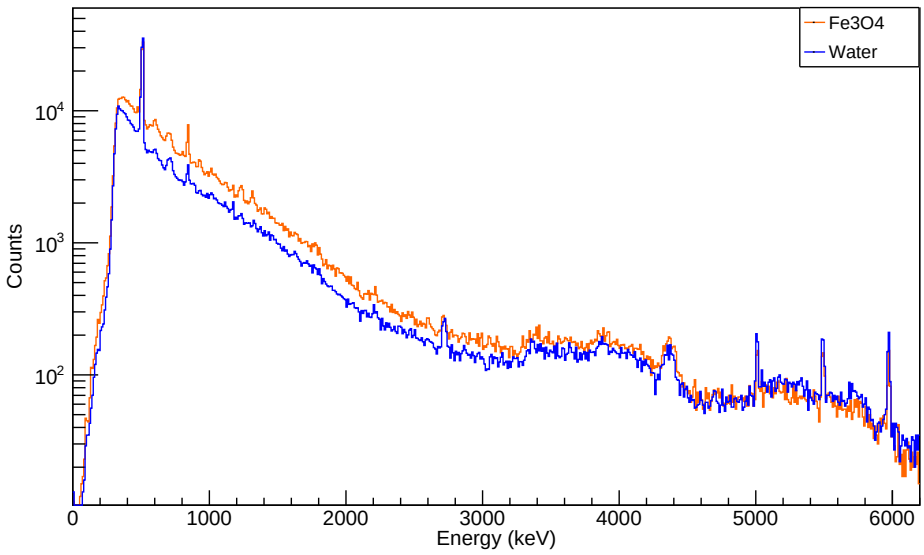

Figure 6.7: Calibrated energy histograms for segmented water and magnetite targets using a proton beam of 36 MeV and 2.88×10^{11} protons.

It is important to note that the energy of the main gamma-rays in the low energy region, which coincides with the energy of the calibration sources, is well reproduced. This can be seen by the 511 keV gamma-ray line, while the high energy region suffers a deviation from the expected values, indicating that the calibration obtained with sources cannot be safely extrapolated to these high energies gamma rays. The characteristic 6.13 MeV gamma-ray is shifted towards lower energies, and the same occurs for the 4.44 MeV gamma-ray. A new calibration, including the oxygen-originating gamma-ray values as well as their single and double escape peaks, is performed. The new calibration polynomial that covers the entire energy range is given by equation 6.5, where we observe significant differences in the second order and the offset terms, and a very small variation in the first degree term. A comparison of the magnetite spectrum with the two calibrations is shown in figure 6.8, where the new calibration only shifts the peaks in the high energy region, improving the results.

$$\mathrm{E}_{HPGe}\ (\mathrm{keV}) = -2.17 \cdot 10^{-4} x^2 + 11.88x - 3.23 \tag{6.5}$$

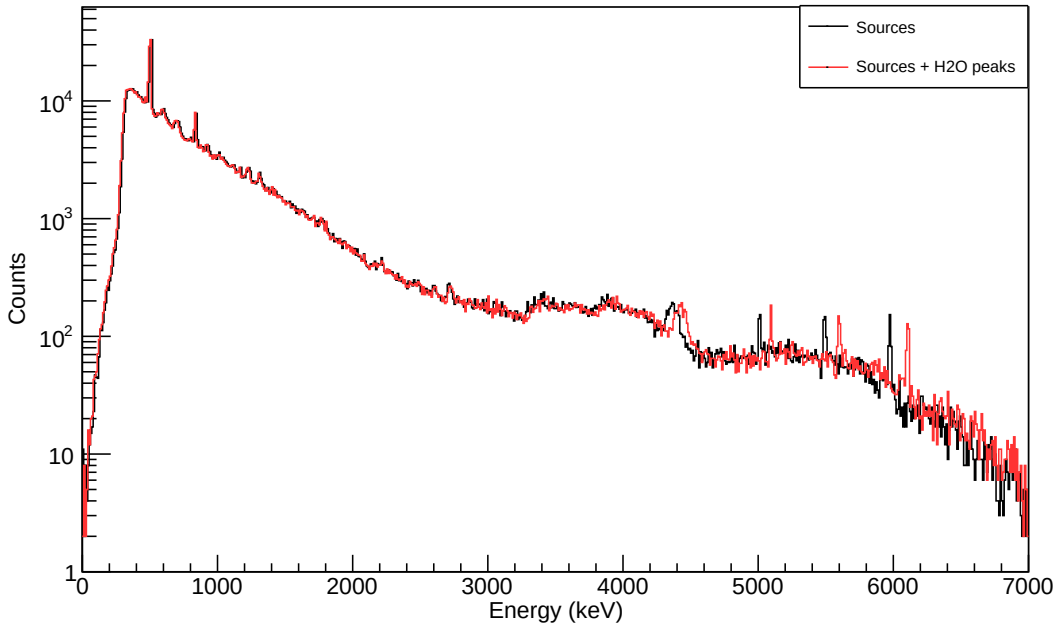

Figure 6.8: Comparison of the magnetite PG spectra for two different calibrations: if only radioactive sources are used the high energy region is shifted towards lower energies. Including the high energy gamma-ray lines in the calibration gives a good result throughout the entire energy region of interest.

The analysis of the characteristic PGs from magnetite was then performed using this new calibration. From the results obtained in the simulation, particularly in figure 4.8, we know that the majority of the characteristic gamma-rays from magnetite are emitted with energies between 800 keV and 1400 keV, hence the search for PGs that are a signature of magnetite will be restricted to this region. The obtained spectra can be seen in figure 6.9, where several structures are detected. The value of the energies obtained with the fit are labelled on the figure, while the error in these values corresponds to 6 keV, as this is the minimum difference between gammas we can measure due to the limited energy resolution imposed by the ADC channel width. For this reason, the peaks at 930 and 935 keV cannot be detected separately, and they merge into a peak structure with a mean of 933(6) keV. The same applies to the PGs at 1225 keV and 1238 keV, that coalesce into another structure at 1233(6) keV. All the other peaks of interest are individually detected. The peak with the highest intensity corresponds to the 847 keV gamma-ray, due to the higher cross section for the inelastic scattering of the proton with the ^{56}Fe nucleus.

A comparison between the experimental energies obtained after the fitting, the Geant4 simulation, the literature values and the associated nuclear reactions are summarised in table 6.2. All the PGs can be associated with a main proton induced reaction, which indicates that the signature of PGs from magnetite can be detected. There is a very good agreement between the literature, simulation and experimental results, which confirms that the magnetite NPs target is a good PG emitter, that can be used to draw conclusions on the proton range.

$\mathbf{E}_{exp}$ **(keV)**	$\mathbf{E}_{simu}$ **(keV)**	$\mathbf{E}_{lit}$ **(keV)**	**Reaction**
808(6)	812(1)	812	^{56}Fe(p,n)^{56}Co
845(6)	847(1)	847	^{56}Fe(p,p')^{56}Fe
933(6)	930(1)	931	^{56}Fe(p,n+p)^{55}Fe
933(6)	935(1)	935	^{54}Fe(p,n)^{54}Co
1038(6)	1037(1)	1037	^{56}Fe(p,p+2α)^{48}Ti
1233(6)	1225(1)	1224	^{56}Fe(p,γ)^{57}Co
1233(6)	1238(1)	1238	^{56}Fe(p,p')^{56}Fe
1317(6)	1316(1)	1316	^{56}Fe(p,n+p)^{55}Fe

Table 6.2: Energies of the experimental gamma-rays detected with the HPGe, simulated with Geant4 and obtained values from the literature, as well as the nuclear reactions channels from which they originate.

As the magnetite NPs are diluted in water, the high energy region of the experimental spectrum must show the characteristic high energy PGs from water. The PGs detected between 3 MeV and 7 MeV are shown in figure 6.10, where six structures are indicated. They correspond to the 4.44 MeV PG from ^{16}O(p,x)^{12}C and the 6.13 MeV PG from ^{16}O(p,p')^{16}O, as well as their single and double escapes due to the small size of the detector. We can observe that in this region the peaks are narrower, as the relative resolution improves and the limitation imposed by the coarse ADC plays a smaller role. This shows that the sub-optimal adjustment of the coarse gain is a limiting factor in the low energy region, but not in the high-energy part of the spectrum.

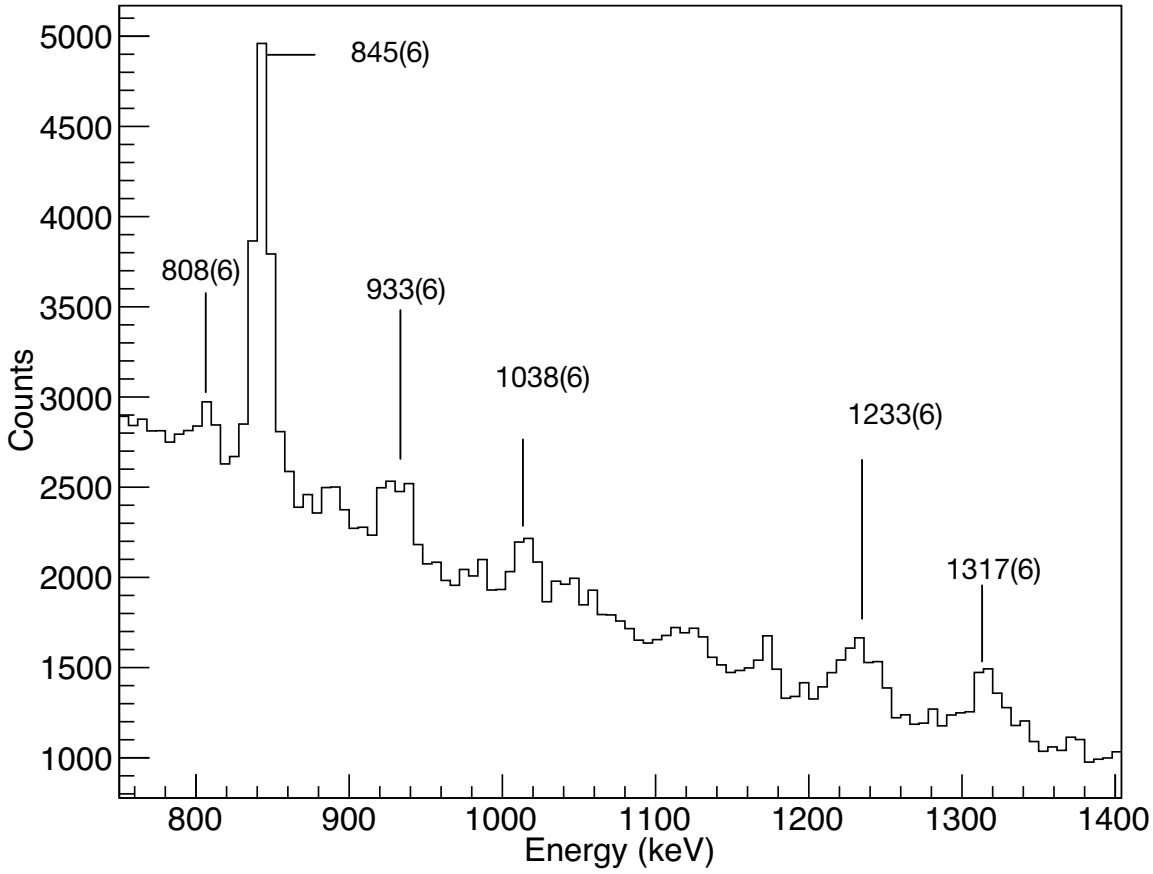

Figure 6.9: Experimental spectrum for the magnetite segmented target in the region between 750 and 1400 keV. The energies of the PGs of interest are indicated for each peak.

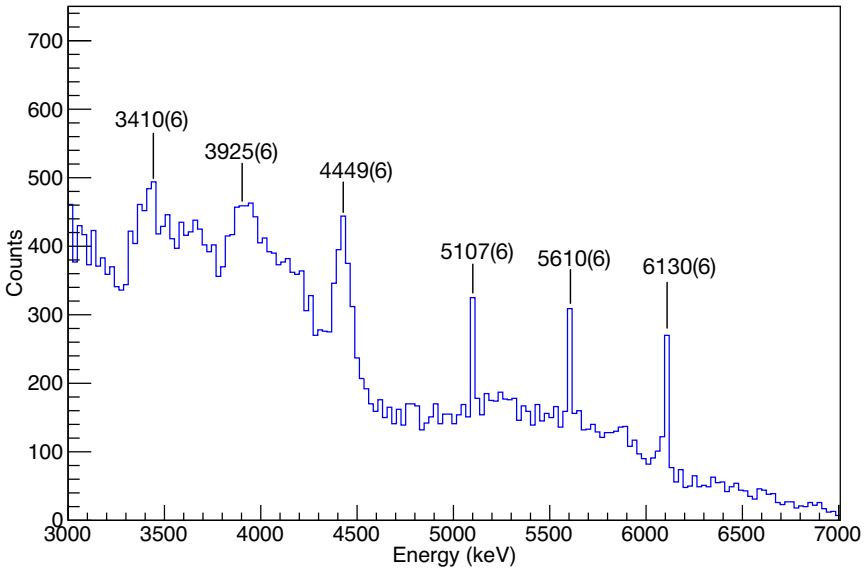

Figure 6.10: Experimental spectrum for a magnetite segmented target in the region between 3000 and 7000 keV. Characteristic PGs from the oxygen in the water are clearly seen, as the magnetite NPs are diluted in water.

6.2.1 Intensity profile

Once the spectrum has been calibrated throughout the entire energy region and the characteristic PGs from the magnetite target have been identified, the intensity variation of the PG with the position of the collimator can be studied. The analysis is initially performed for the 847 keV gamma ray, as the statistics are higher for this value. Figure 6.11 shows the number of counts under the peaks versus the position of the collimator for the experiment, for the emitted gamma ray counts originating from a particular 3 mm region along the beam axis (scaled by a factor 2000) and for the detected gamma ray counts in the simulation. There is a good agreement between simulation and experiment, as both show the maximum number of counts in the same collimator positions. There are two experimental maxima: one in the first part of the target, when the collimator is placed at 3 mm and the second maximum is reached in the second segment of the target, precisely at 24mm. While the first maximum is due to the collimator width effect (explained in section 4.16), the second maximum relates to the proton range, as this position corresponds to the maximum emission of PG that takes place before reaching the BP. From the comparison of experiment and simulation, we can conclude that the PG emission for the segmented magnetite target at 847 keV is maximum at

an absolute depth of (24.0 ± 1.5) mm in the target material. It is also worth noting that the number of emitted counts from the simulation drops to zero in the region between the targets, as no PGs are emitted perpendicularly to the target for said region. The simulated results for the detected counts in the HPGe detector, however, show that the number of counts detected is reduced drastically, but is not zero. This discrepancy can be explained based on the fact that the emitted number of PGs is obtained with the projection of the target emission, and therefore in the air gap there are no counts emitted. However, the detected PGs are gamma rays that have been created in the target, and travelled through the collimator window, which could include PGs that are not emitted completely perpendicular to the target, such as scattered PGs, background and gamma-rays from any region of the phantom that leak through the collimator. Experimental results confirm this, showing the detection of characteristic PGs in the air region, which originate from the magnetite regions.

These results confirm that a collimated HPGe detector is capable of measuring the 1D intensity profile for each gamma ray, and a study on the variation of the number of counts for characteristic PGs leads to conclusions about the range of the proton beam. The detection system could be applied to determine the region of the BP.

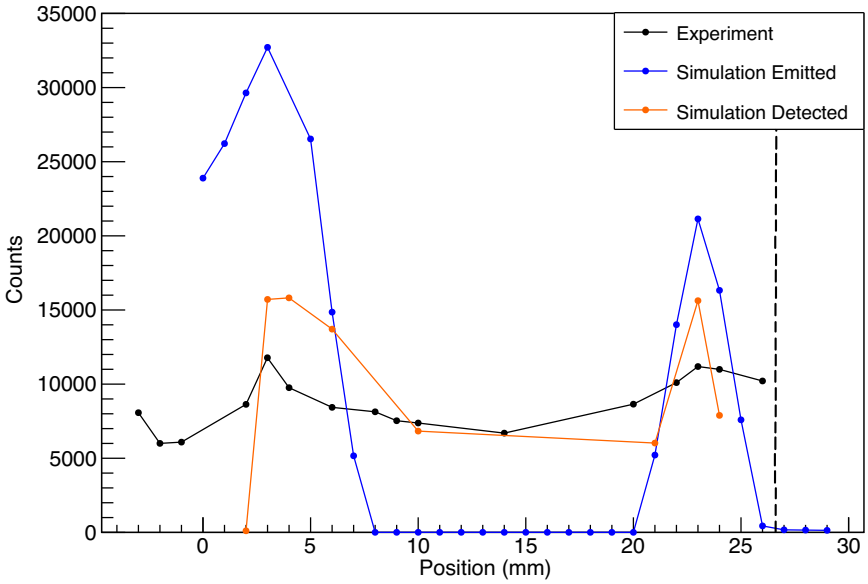

Figure 6.11: Comparison of the number of counts in the 847 keV PG versus the position for experiment (black line), and simulation (blue line for emitted, and orange line for detected). A good agreement is observed, and all three cases reach their maximum in the same positions.

The same analysis is performed for two peaks corresponding to the other two reactions most likely to occur: 812 keV, from ^{56}Fe(p,n)^{56}Co and 1317 keV from ^{56}Fe(p,np)^{55}Fe. The results are presented in figure 6.12, where we can observe that the first peak always occurs at 3 mm, confirming that this maximum is due to the combination of the segmented target and the collimator window, and is not a direct consequence of the particular reaction, as studied with the simulation in section 4.6. The position of the second peak changes for the different reactions, reflecting the energy dependence of the cross section for each reaction. The PG from ^{55}Fe peaks at 22 mm, this is before the ^{56}Fe, that peaks at 24 mm while the ^{56}Co peaks at 26 mm. These results agree well with their cross sections: the cross section for ^{55}Fe is maximum at higher energies than the others (as shown in figure 2.3), therefore the maximum emission of PG will be reached at a higher energy than for the other two processes, and this happens at a smaller depth in the target as the beam reduces its energy in the interactions with the target material.

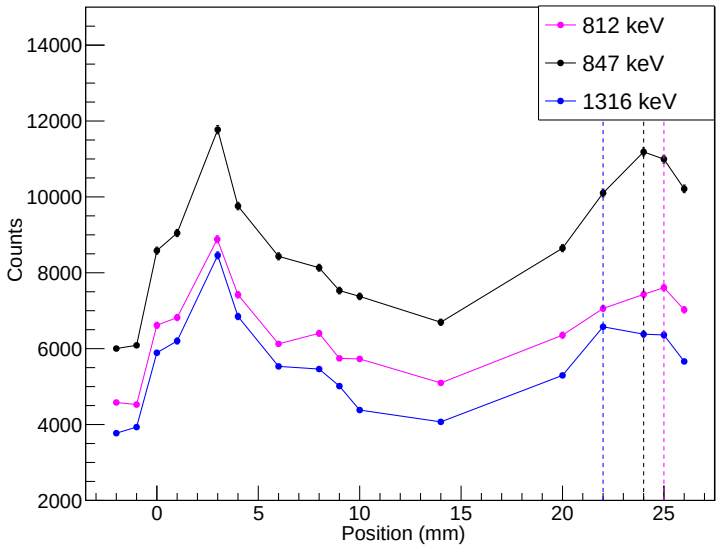

Figure 6.12: Comparison of the number of counts versus the position for three different gamma-rays: 812 keV from ^{56}Co (pink solid line), 847 keV from ^{56}Fe (black solid line) and 1317 from ^{55}Fe (blue solid line). Each of them peak at a different depth, indicated with a dashed line, due to their different cross sections.

The intensity variation for each gamma ray can be used to determine the region of the BP, as the intensity of every PG drops drastically. Furthermore, the obtained results show an excellent agreement with the known cross sections for the corresponding reactions, con-

firming that the identification of PG is correct and they are associated to the aforementioned transitions.

6.3 PGs in the CLLB

The data acquired with the CLLB in previous experiments showed positive results for the 847 keV gamma-ray, as discussed in sections 5.1 and 5.2. During this experiment, the CLLB detector acquired data in PHA mode, therefore the discrimination between neutrons and gammas is not possible, hence the thermal neutron peak will be visible at 3.2 MeV. Figure 6.13 shows the obtained experimental spectra for the segmented water target, after applying the calibration obtained in equation 6.1. We observe that the peaks in the low energy region agree with the expected results by looking at the 511 keV, but the high energy region is shifted towards lower energies, similarly to the HPGe spectra.

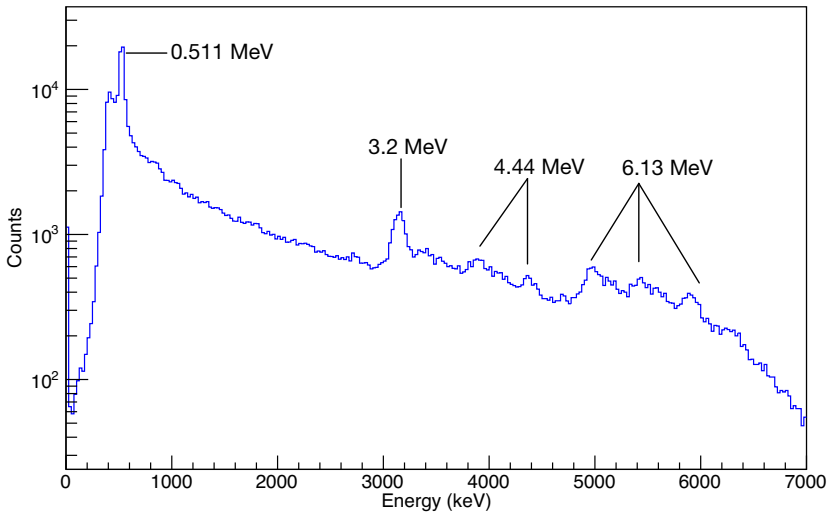

Figure 6.13: Calibrated energy spectrum, acquired with the CLLB detector in PHA mode, for the segmented water target after the irradiation with a proton beam of 36 MeV and 2.88×10^{11} protons. The 511 keV gamma-ray peak, the neutron peak at 3.2 MeV and the water characteristic PG peaks at 4.44 MeV and 6.13 MeV are indicated.

It is noted that the higher the energy of the gamma ray, the higher the deviation is, as the calibration was performed with radioactive sources whose energies are below 2 MeV. To apply the calibration to the whole energy region, we need to correct it by adding the gamma-rays from water to the calibration polynomial. The centroids for the 6.13 MeV, as well as

its double and single escape will be added, while for the 4.44 MeV only the single escape peak can be added, as the double escape is hidden underneath the neutron peak. The final calibration function, given by equation 6.6, is applied to the whole energy region of interest.

$$\text{E (keV)} = 0.005129x^2 + 12.75x - 7.256 \tag{6.6}$$

The calibrated histograms for water and magnetite, at the same collimator position, and normalised by the integral charge, can be seen in figure 6.14. The spectra shows a higher detection of PGs for the magnetite target in the region below 4 MeV, as expected, because the characteristic PGs from the iron component are emitted in this energy range. The intensity of the gamma-rays converge after the 4.44 MeV PG. For higher energies, the trend is the opposite: the statistics are higher for water, as the 6.13 MeV peak comes from the irradiation of oxygen, and the Oxygen concentration is higher in the water-only target compared to the NPs solution. These results agree well with the experimental results, obtained in the two previous experiments, at 38 MeV and 66.5 MeV (reported in chapter 5).

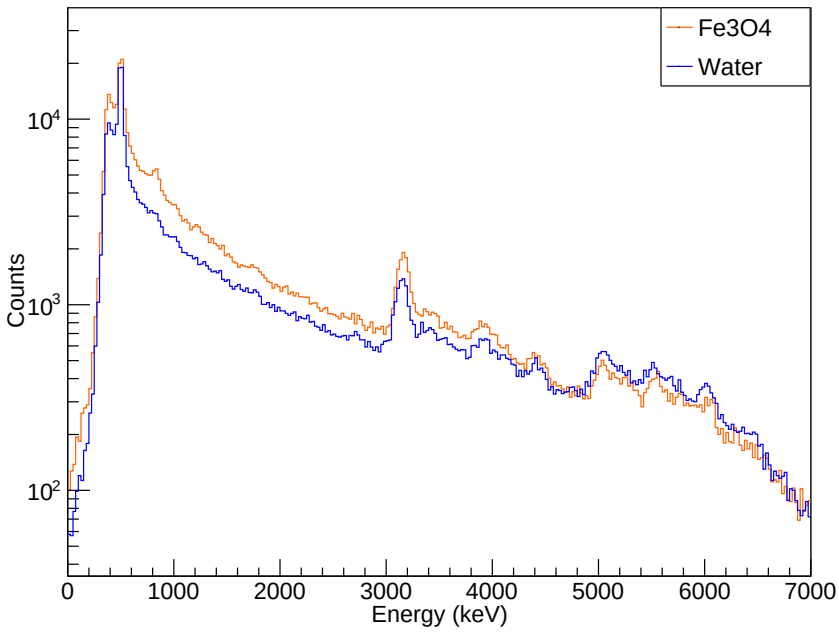

Figure 6.14: Calibrated energy spectrum acquired with the CLLB detector in PHA mode, for the segmented water target, after the irradiation with a proton beam of 36 MeV and 2.88×10^{11} protons. The 511 keV, neutron peak at 3.2 MeV and water characteristic PGs at 4.44 MeV and 6.13 MeV are indicated.

The ratio between water and magnetite runs can be performed, to quantify numerically the difference between both runs at different energies. The experimental ratios, obtained by dividing the water histograms by the magnetite histograms at two different collimator positions, before the BP and in the BP region, are shown in figure 6.15. The trend of the ratio is overall smooth, as it increases progressively. However, it is important to note that the drop in the ratio that occurs in the 3.2 MeV region does not relate to the emission of the PGs, as it is caused by the thermal neutrons detected with the CLLB. These come from the impossibility to eliminate the thermal neutron peak from our acquired PG spectra, and therefore those points do not need to be considered for the analysis.

The ratio value is smaller than the unit at low energies, and increases after that because the emission of PGs from iron dominates the low energy region, and the oxygen reactions are enhanced in the high energy region. The trend of the ratios agree well with the obtained results from KVI-CART (shown in figure 5.20), which shows consistency and confirms that, even with a coarse energy region, the combination of NPs and a low resolution detector can be used to determine if the BP region has been reached or not during the treatment.

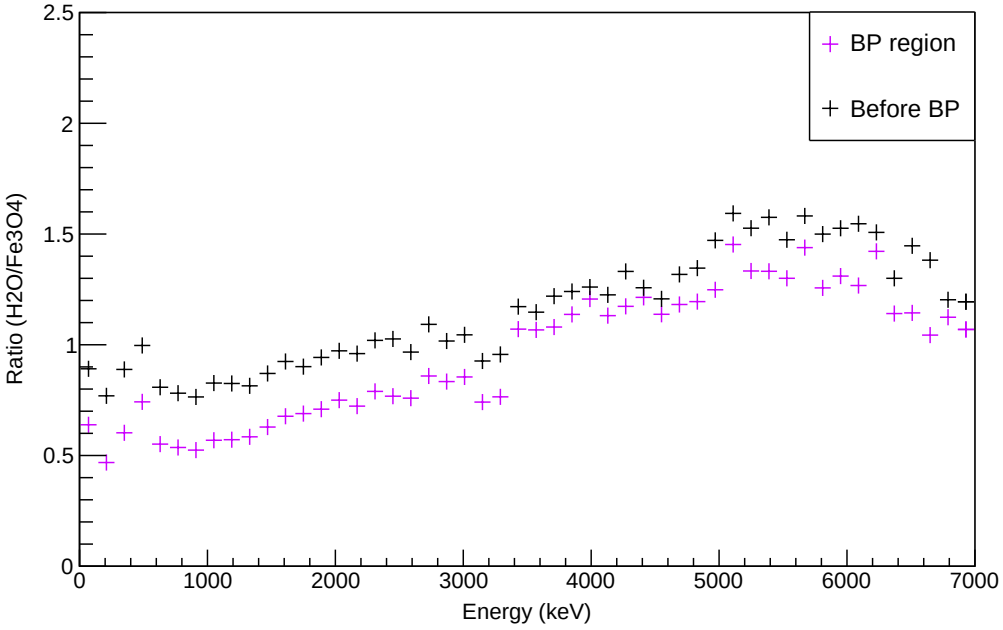

Figure 6.15: Experimental ratio of water runs divided by magnetite runs, for two positions (in the BP, and before the BP). It is observed that the ratio increases with the energy of the gamma rays.

Focusing the analysis on the NPs segmented target, we observe in figure 6.16 the experimental spectra obtained for different collimator positions. As we look at deeper sections of the target, the number of gammas noticeably increases. This increase is very clear in the PGs that originate from the proton irradiation of the oxygen, but also in the low energy region (between 500 and 1000 keV), where we can observe a clear structure for the run at 16 mm, which is not visible in the other two runs. Fitting the position to a Gaussian function plus a linear background, we obtain that the energy of the peak corresponds to 835(4) keV. This result is deviated 10 keV from the expected PG from inelastic scattering of ^{56}Fe, in which the deviation can be explained by the resolution of the detector. The energy resolution of the CLLB obtained during the experiment is 4.050% at 1173 keV, so in lower energies the value of the resolution will be higher. Therefore the 812 keV and 847 keV gamma-ray coalesce to a wider structure, whose centroid will have an energy value between the two of them.

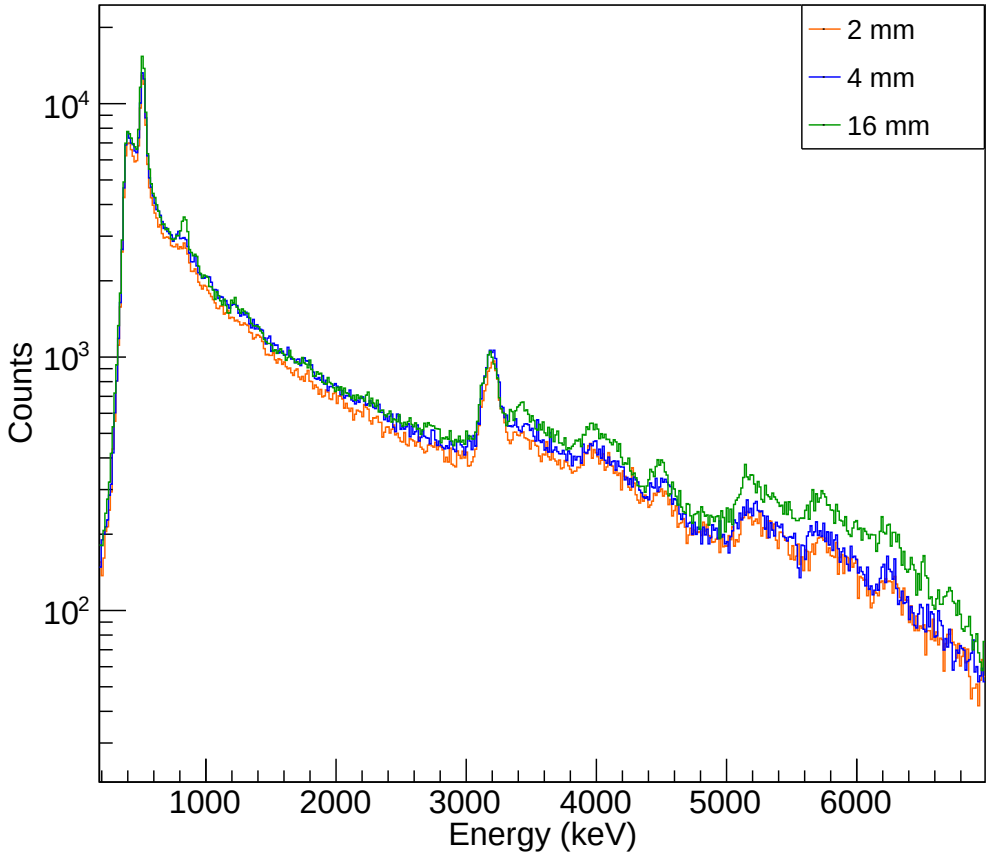

Figure 6.16: Calibrated energy spectrum acquired with the CLLB detector in PHA mode for the segmented magnetite target at different collimator positions for a 36 MeV proton beam.

A close-up of the 800 keV region can be seen in figure 6.17, where we observe the merged structure of the 812 keV and 847 keV PGs. For comparison, the histogram obtained with the simulation, in which the experimental resolution has been convoluted is shown, supporting the claim that the distinction of these two neighbouring peaks is not possible. This figure also shows that no other characteristic PGs from the magnetite are detected in the region of interest. Comparing the results with those obtained for the HPGe in figure 6.9, explains why we do not detect any other gammas, as the structures will broaden and merge with the background.

A direct consequence of the resolution of CLLB is that an intensity profile for the characteristic 847 keV gamma ray cannot be obtained, as this gamma ray merges with others, from different processes, into the same structure. A direct comparison with the HPGe intensity profile is therefore not possible.

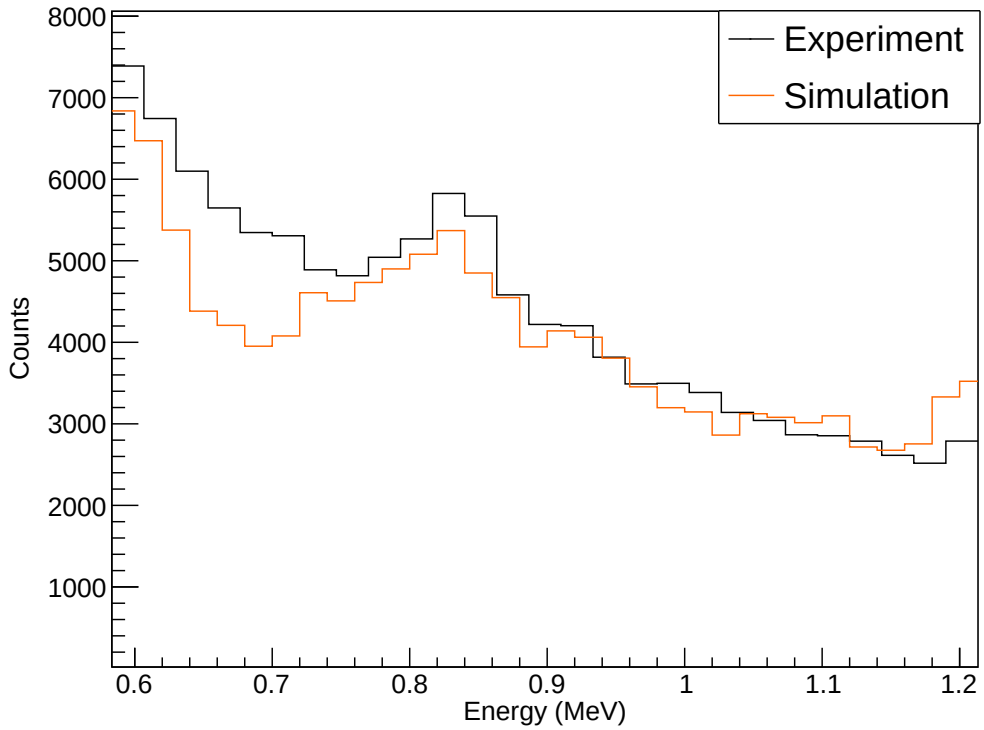

Figure 6.17: Comparison between experiment and simulation for the CLLB detector. A clear structure at 835(4) keV is visible for both cases.

6.4 Summary

This chapter illustrated the results for the in-beam experiment, using a 36 MeV proton beam and segmented targets, that took place at the University of Birmingham. The segmented targets were irradiated with a proton beam of 2.88×10^{11} protons, and two detection systems were used simultaneously. The first detection system is the HPGe detector, that was implemented with the main objective of detecting more characteristic gamma rays from a magnetite target, and to study the intensity profile of particular PGs as a function of depth. The second detection system, the CLLB scintillator, was used to study the ratio of the PGs between two different materials.

The resolution of both detectors was obtained, showing a value of 4.05% for the CLLB and 0.698% for the HPGe, at 1173 keV. These results indicate that the HPGe will differentiate structures that coalesce in the CLLB, as it was later proved for the 847 keV PG.

The analysis of the PG spectra was performed separately for both detectors. The HPGe showed very positive results, detecting not only the 847 keV PG, but another five characteristic gamma rays originating from the irradiation of iron in the magnetite compound. The study of the intensity versus the position of the collimator shows an excellent agreement with the simulated data, where we observe a maximum in the first segment of the target, that is due to the collimator window, and a second one in the region before the BP. This second maximum is of particular interest for this project, as it directly relates to the cross sections of the different processes and allows us to draw conclusions on the range of the proton. The intensity study was performed for three different PGs (at 812 keV, 847 keV and 1316 keV) that originated from different reaction mechanisms. The region of maximum emission changed for each of the PGs, and the results showed a good agreement with the tabulated cross sections. The results can be used to indicate the region of the BP, by studying how the intensity of each gamma ray changes with the depth of the target. The maximum will be reached in the region before the BP, independently of the reaction that induces the PG. These results can be applied in a clinical environment by studying the characteristic emission at different depths, and when the value begins to decrease the irradiation must be stopped, as the BP region would have been reached.

The CLLB results will not show all the characteristic PGs, as the detector's resolution is worse and the set-up is not optimised for this detector. A comparison between the magnetite and water targets shows that the intensity in the spectra varies for the different regions, and hence the ratio of the two is obtained at different positions. The ratio shows a maximum value for the high energy region, where characteristic PGs from water dominate. Furthermore, the overall ratio is lower in the BP region than out of it. A clear distinction between regions can be determined from the ratio value, and therefore it can be used during the treatment to determine if the BP region has been reached in the tumou,r in which the NPs are accumulated. The ratio can be obtained in-vivo, and a decrease in the value must be observed. The irradiation must stop once the ratio value starts increasing again, as this determines that the BP is no longer located in the NPs region, and healthy structures beyond the tumour are being irradiated.

Overall, positive results are obtained for both detection systems which can be used for range verification purposes. The HPGe detects characteristic PGs from the NPs, and the variation in intensity allows to determine when the BP region has been reached. The CLLB determines the region of the BP with the variation of the ratio for the divided histograms.

Chapter 7

Summary and outlook

In this final chapter a general overview of the thesis is presented. Thereafter, the main experimental and simulated results of the project are discussed. Conclusions are drawn concerning the aforementioned results. Finally, an outlook is provided to examine the potential work in PGI of nanoparticles for range verification in proton therapy treatments.

7.1 Summary

PT is an emerging modality for cancer treatment that induces a better dose conformation compared to traditional proton therapy, and due its the localised dose deposition (i.e the BP) the dose applied to healthy structures and tissues nearby is greatly reduced. However, there are many sources of uncertainties in clinical practice that affect the range of the proton beam. A miscalculation in the range leads to the under-dose of the tumoural region, while overdosing the normal tissues in a more severe way than traditional photon therapy, which leads to a reduction of the effectiveness of the treatment.

Therefore, to reduce beam range uncertainties, in-vivo monitoring of the range is crucial to fully exploit the advantages of PT. Several range verification methods have been developed in the past that rely on the detection of PGs or beta emitters. PG radiation has a crucial advantage compared to other methods, as it is produced instantaneously and exits the patient's body without interacting with any organs or tissues. Consequently, the information they carry is undisturbed and can be used to draw conclusions on the beam range.

Another technique used to exploit the advantages of PT is the use of radio enhancers, to increase the effectiveness of the treatment. Metallic NPs have been used as radiosensitisers because, due to their high atomic number, they have the ability to increase the therapeutic effect of PT. In the past few years, the use of nanoparticles as dose enhancers has been widely extended. Due to their small size, they have the ability to travel through the blood and accumulate in the tumoural region, without extravasating to other healthy structures, according to the EPR effect.

This project focuses on the combination of both techniques: a NPs dose enhancer material is used to determine the range of the proton beam. This novelty combination improves PT treatments by allowing the verification of the proton range, while enhancing the dose in the tumoural region. Several dose enhancer materials were considered, but due to its low price, high atomic number and biocompatibility, magnetite (Fe_3O_4) was the chosen material. Two NPs targets of magnetite diluted in water were designed in house for this project. A dedicated detection system, consisting of a scintillator and a HPGe, was developed and tested at two different facilities, to explore the PG emission at three different beam energies: 36 MeV, 38 MeV and 66.5 MeV. Simultaneously, a Geant4 Monte Carlo simulation was developed to prove the feasibility of the material as a dose enhancer agent, and a prompt gamma-ray emitter.

Three in-beam experiments have been conducted as part of this project. Initially, the detection system was assessed with a proton beam of 38 MeV, to study the performance of the CLLB detector in a low neutron-induced background. Then, a more clinically-realistic experiment was performed at an energy of 66.5 MeV. Finally, a HPGe detection system was added to the detection system, and tested with a beam energy of 36 MeV.

The results obtained with the CLLB showed the detection of the characteristic PGs from magnetite, proving the feasibility of a NPs material as a gamma-ray emitter. The current results also support that a modest energy resolution gamma-ray detector can be used with sufficient sensitivity in resolving different target materials by applying the ratio method that is sensitive to coarse energy regions, rather than individual gamma rays. This is possible due to the increased emission of prompt gamma-rays in the low energy region of the spectrum from the localised nanoparticles, as opposed to the more abundant elements in the tissues, which emit relatively few low-energy gamma rays.

The ratio method can also be used to verify the position of the BP, as the value of the ratio decreases notoriously for this region. The results suggest that the overall ratio is lower in the BP region, so a differentiation between regions can be used to determine if the BP region has been reached.

It is also found that, when using a realistic nanoparticle concentration, the intensity profile can be obtained from the gamma-ray yields of several reactions, if the detector has sufficient resolution to avoid the coalescing of two structures. The intensity profile directly correlates with the cross section of the originating processes. The dependence of the BP position with the cross sections can be used to localise the BP region with a precision of a few mm. This provides an additional method for in-vivo range verification. To obtain the required intensity profile, a gamma-ray detector of with a few keV resolution is required to resolve the required characteristic gamma-rays independently, as they are often close to each other in energy due to the relatively high level density observed in iron.

7.2 Outlook

The experiments performed for this project prove the practicality of a NPs target as dose enhancer agent and a prompt gamma-ray emitter. The emission of characteristic prompt gamma-rays, after the proton irradiation of the NPs, can be used to draw conclusions on the range of the protons, and the composition of the irradiated tissue.

The ratio results obtained with the CLLB suggest that a low energy resolution scintillator can be used in PT to obtain PG measurements, as the ratio of coarse energy regions is sensitive to tissue composition and behaves as an indicator of whether the NPs inside tumour have been irradiated or not. There is no need to resolve any structures, as the density and composition of the material are enough to determine which region has received radiation. This technique could be implemented, as low energy resolutions are widely available.

The study of the intensity profile of the characteristic PGs, showed a good agreement with the tabulated cross sections, and therefore can be trusted to determine the position of the BP region. However, for this application higher resolution detectors are needed, in order to separate the gamma rays and evaluate their intensity profiles separately.

We can confirm that the studied technique has the potential to improve PT treatments. The next proposed step in this research is to evaluate the ratio values and intensity profile in a more realistic phantom, with higher proton beam energies to replicate clinical conditions.

A further analysis into different NP materials would be beneficial, to expand the obtained results to other elements, but also to reduce the technical demand for a high resolution detector. If the emitted characteristic gamma-rays from the NPs material are distant in energy, the measurements could be acquired with the same low resolution detector that can determine the ratio of the materials, eliminating the need for a high resolution detector and reducing the cost of implementing this technique in clinic.

Bibliography

[1] R. Orecchia, A. Zurlo, A. Loasses et al. *Particle beam therapy (hadrontherapy): basis for interest and clinical experience.* Eur. J. Cancer, volume 34 (1998)(4): pp. 459–468.

[2] H. M. Kooy and C. Grassberger. *Intensity modulated proton therapy.* Br J Radiol, volume 88 (2015)(1051): p. 20150,195.

[3] A.-C. Knopf and A. Lomax. *In vivo proton range verification: a review.* Physics in Medicine and Biology, volume 58 (2013)(15): pp. R131–R160. URL `https://doi.org/10.1088/0031-9155/58/15/r131`.

[4] E. N. Bodine and K. L. Monia. *A proton therapy model using discrete difference equations with an example of treating hepatocellular carcinoma.* Mathematical Biosciences Engineering, volume 14 (2017)(4): pp. 881–899.

[5] H. Paganetti. *Range uncertainties in proton therapy and the role of Monte Carlo simulations.* Phys Med Biol, volume 57 (2012)(11): pp. 99–117.

[6] H. Paganetti (Editor). *Proton Therapy Physics.* CRC Press, 2016. URL `https://doi.org/10.1201/9780367803551`.

[7] B. Arjomandy, P. Taylor, C. Ainsley et al. *Aapm task group 224: Comprehensive proton therapy machine quality assurance.* Medical Physics, volume 46 (2019)(8): pp. e678–e705. URL `https://aapm.onlinelibrary.wiley.com/doi/abs/10.1002/mp.13622`.

[8] M. Goitein. *Calculation of the uncertainty in the dose delivered during radiation therapy.* Medical Physics, volume 12 (1985)(5): pp. 608–612. URL `https://doi.org/10.1118/1.595762`.

[9] J. Schuemann, S. Dowdell, C. Grassberger et al. *Site-specific range uncertainties caused by dose calculation algorithms for proton therapy.* Physics in Medicine and Biology, volume 59 (2014)(15): pp. 4007–4031. URL `https://doi.org/10.1088/0031-9155/59/15/4007`.

[10] H. D. Maccabee, U. Madhvanath and M. R. Raju. *Tissue activation studies with alpha-particle beams.* Phys Med Biol, volume 14 (1969)(2): pp. 213–224.

[11] K. Parodi. *PET monitoring of hadrontherapy.* Nuclear Medicine Review, volume 15 (2012)(C): pp. 37–42. ISSN 1506-9680. URL `https://journals.viamedica.pl/nuclear_medicine_review/article/view/28472`.

[12] U. Oelfke, G. K. Y. Lam and M. S. Atkins. *Proton dose monitoring with PET: quantitative studies in lucite.* Physics in Medicine and Biology, volume 41 (1996)(1): pp. 177–196. URL `https://doi.org/10.1088%2F0031-9155%2F41%2F1%2F013`.

[13] T. Tomitani, J. Pawelke, M. Kanazawa et al. *Washout studies of 11C in rabbit thigh muscle implanted by secondary beams of HIMAC.* Phys Med Biol, volume 48 (2003)(7): pp. 875–889.

[14] I. Martínez-Rovira, C. Jouvie and S. Jan. *Technical note: Implementation of biological washout processes within GATE/GEANT4–a Monte Carlo study in the case of carbon therapy treatments.* Medical physics, volume 42 (2015): p. 1773.

[15] X. Zhu and G. El Fakhri. *Proton therapy verification with PET imaging.* Theranostics, volume 3 (2013)(10): pp. 731–740.

[16] K. Parodi, T. Bortfeld and T. Haberer. *Comparison between in-beam and offline positron emission tomography imaging of proton and carbon ion therapeutic irradiation at synchrotron- and cyclotron-based facilities.* International Journal of Radiation Oncology-Biology-Physics, volume 71 (2008)(3): pp. 945–956. URL `https://doi.org/10.1016/j.ijrobp.2008.02.033`.

[17] A. Kraan, G. Battistoni, N. Belcari et al. *Proton range monitoring with in-beam PET: Monte Carlo activity predictions and comparison with cyclotron data.* Physica medica:

official journal of the Italian Association of Biomedical Physics (AIFB), volume 30 (2014).

[18] X. Zhu, S. España, J. Daartz et al. *Monitoring proton radiation therapy with in-room PET imaging.* Physics in Medicine and Biology, volume 56 (2011)(13): pp. 4041–4057. URL `https://doi.org/10.1088/0031-9155/56/13/019`.

[19] H. Meißner, H. Fuchs, A. Hirtl et al. *Towards offline PET monitoring of proton therapy at MedAustron.* Zeitschrift für Medizinische Physik, volume 29 (2019)(1): pp. 59–65. URL `https://doi.org/10.1016/j.zemedi.2018.05.003`.

[20] C. H. Min, C. H. Kim, M.-Y. Youn et al. *Prompt gamma measurements for locating the dose falloff region in the proton therapy.* Applied Physics Letters, volume 89 (2006)(18): p. 183,517.

[21] J. Polf, S. Peterson, G. Ciangaru et al. *Prompt gamma-ray emission from biological tissues during proton irradiation: A preliminary study.* Physics in medicine and biology, volume 54 (2009): pp. 731–43.

[22] J. M. Verburg, H. A. Shih and J. Seco. *Simulation of prompt gamma-ray emission during proton radiotherapy.* Physics in Medicine and Biology, volume 57 (2012)(17): pp. 5459–5472. URL `https://doi.org/10.1088/0031-9155/57/17/5459`.

[23] J. C. Polf, D. Mackin, E. Lee et al. *Detecting prompt gamma emission during proton therapy: the effects of detector size and distance from the patient.* Phys Med Biol, volume 59 (2014)(9): pp. 2325–2340.

[24] C. Golnik, F. Hueso-González, A. Müller et al. *Range assessment in particle therapy based on prompt-ray timing measurements.* Physics in Medicine and Biology, volume 59 (2014)(18): pp. 5399–5422. URL `https://doi.org/10.1088/0031-9155/59/18/5399`.

[25] T. Werner, J. Berthold, W. Enghardt et al. *Range verification in proton therapy by prompt gamma-ray timing (PGT): Steps towards clinical implementation.* In *2017 IEEE Nuclear Science Symposium and Medical Imaging Conference (NSS/MIC)*, (pp. 1–5). 2017.

[26] F. Hueso-González, M. Rabe, T. A. Ruggieri et al. *A full-scale clinical prototype for proton range verification using prompt gamma-ray spectroscopy.* Physics in Medicine & Biology, volume 63 (2018)(18): p. 185,019. URL `https://doi.org/10.1088/1361-6560/aad513`.

[27] J. M. Verburg and J. Seco. *Proton range verification through prompt gamma-ray spectroscopy.* Phys Med Biol, volume 59 (2014)(23): pp. 7089–7106.

[28] Z. Kuncic and S. Lacombe. *Nanoparticle radio-enhancement: principles, progress and application to cancer treatment.* Physics in Medicine & Biology, volume 63 (2018)(2): p. 02TR01. ISSN 1361-6560. URL `https://iopscience.iop.org/article/10.1088/1361-6560/aa99ce`.

[29] S. K. Golombek, J.-N. May, B. Theek et al. *Tumor targeting via EPR: Strategies to enhance patient responses.* Advanced Drug Delivery Reviews, volume 130 (2018): pp. 17–38. URL `https://doi.org/10.1016/j.addr.2018.07.007`.

[30] Y. Matsumura and H. Maeda. *A new concept for macromolecular therapeutics in cancer chemotherapy: mechanism of tumoritropic accumulation of proteins and the antitumor agent smancs.* Cancer Res, volume 46 (1986)(12 Pt 1): pp. 6387–6392.

[31] J. F. Hainfeld, D. N. Slatkin and H. M. Smilowitz. *The use of gold nanoparticles to enhance radiotherapy in mice.* Physics in Medicine and Biology, volume 49 (2004)(18): pp. N309–N315. ISSN 0031-9155, 1361-6560. URL `https://iopscience.iop.org/article/10.1088/0031-9155/49/18/N03`.

[32] C. T. Badea, D. P. Clark, M. Holbrook et al. *Functional imaging of tumor vasculature using iodine and gadolinium-based nanoparticle contrast agents: a comparison of spectral micro-CT using energy integrating and photon counting detectors.* Phys Med Biol, volume 64 (2019)(6): p. 065,007.

[33] A. K. Hauser, M. I. Mitov, E. F. Daley et al. *Targeted iron oxide nanoparticles for the enhancement of radiation therapy.* Biomaterials, volume 105 (2016): pp. 127–135.

[34] C. Wälzlein, E. Scifoni, M. Krämer et al. *Simulations of dose enhancement for heavy atom nanoparticles irradiated by protons.* Physics in Medicine and Biology, volume 59 (2014)(6): pp. 1441–1458. ISSN 1361-6560.

[35] J. Choi, G. Kim, S. B. Cho et al. *Radiosensitizing high-Z metal nanoparticles for enhanced radiotherapy of glioblastoma multiforme.* Journal of Nanobiotechnology, volume 18 (2020)(1): p. 122. ISSN 1477-3155. URL `https://doi.org/10.1186/s12951-020-00684-5`.

[36] B. Gottschalk. *Radiotherapy proton interactions in matter*, 2018. URL `https://arxiv.org/abs/1804.00022`.

[37] W. D. Newhauser and R. Zhang. *The physics of proton therapy.* Phys Med Biol, volume 60 (2015)(8): pp. 155–209.

[38] H. Bethe. *Zur theorie des durchgangs schneller korpuskularstrahlen durch materie.* (1930).

[39] W. H. Bragg and R. Kleeman. *XXXIX on the particles of radium, and their loss of range in passing through various atoms and molecules.* The London, Edinburgh, and Dublin Philosophical Magazine and Journal of Science, volume 10 (1905)(57): pp. 318–340. URL `https://doi.org/10.1080/14786440509463378`.

[40] H. Paganetti. *Range uncertainties in proton therapy and the role of Monte Carlo simulations.* Physics in medicine and biology, volume 57 (2012): pp. R99–117.

[41] N. Bohr. *LX on the decrease of velocity of swiftly moving electrified particles in passing through matter.* The London, Edinburgh, and Dublin Philosophical Magazine and Journal of Science, volume 30 (1915)(178): pp. 581–612. URL `https://doi.org/10.1080/14786441008635432`.

[42] L. Landau. *On the energy loss of fast particles by ionization.* J. Phys. (USSR), volume 8 (1944): pp. 201–205.

[43] P. V. Vavilov. *Ionization losses of high-energy heavy particles.* Sov. Phys. JETP, volume 5 (1957): pp. 749–751.

[44] W. T. Chu, B. A. Ludewigt and T. R. Renner. *Instrumentation for treatment of cancer using proton and light-ion beams.* Review of Scientific Instruments, volume 64 (1993)(8): pp. 2055–2122. ISSN 0034-6748. URL `http://inis.iaea.org/search/search.aspx?orig_q=RN:24069706`.

[45] T. Bortfeld. *An analytical approximation of the Bragg curve for therapeutic proton beams.* Med Phys, volume 24 (1997)(12): pp. 2024–2033.

[46] B. Gottschalk, A. M. Koehler, R. J. Schneider et al. *Multiple Coulomb scattering of 160 MeV protons.* Nuclear Instruments and Methods in Physics Research B, volume 74 (1993)(4): pp. 467–490.

[47] H. Paganetti. *Nuclear interactions in proton therapy: Dose and relative biological effect distributions originating from the primary and secondary particles.* Physics in medicine and biology, volume 47 (2002): pp. 747–64.

[48] S. Kodaira, T. Konishi, H. Kitamura et al. *On the use of CR-39 PNTD with AFM analysis in measuring proton-induced target fragmentation particles.* Nuclear Instruments and Methods in Physics Research Section B: Beam Interactions with Materials and Atoms, volume 349 (2015): pp. 163–168. ISSN 0168-583X. URL `https://www.sciencedirect.com/science/article/pii/S0168583X15001779`.

[49] S. Kodaira, H. Kitamura, M. Kurano et al. *Contribution to dose in healthy tissue from secondary target fragments in therapeutic proton, He and C beams measured with CR-39 plastic nuclear track detectors.* Scientific Reports, volume 9 (2019).

[50] J. Verburg, H. Shih and J. Seco. *Simulation of prompt gamma-ray emission during proton radiotherapy.* Physics in medicine and biology, volume 57 (2012): pp. 5459–72.

[51] A. Koning, D. Rochman, J.-C. Sublet et al. *Tendl: Complete nuclear data library for innovative nuclear science and technology.* Nuclear Data Sheets, volume 155 (2019): pp. 1–55. ISSN 0090-3752. URL `https://www.sciencedirect.com/science/article/pii/S009037521930002X`. Special Issue on Nuclear Reaction Data.

[52] M. Planck. *Ueber das gesetz der energieverteilung im normalspectrum.* Annalen der Physik, volume 309 (1901)(3): pp. 553–563. URL https://doi.org/10.1002/andp.19013090310.

[53] G. F. Knoll. *Radiation Detection and Measurement.* John Wiley & Sons, Chichester, England, 4 edition, 2010.

[54] R. D. Evans. *Atomic Nucleus.* Krieger Publishing Company, Melbourne, FL, 1982.

[55] R. D. Evans and A. Beiser. *The Atomic Nucleus.* Physics Today, volume 9 (1956)(12): pp. 33–34. URL https://doi.org/10.1063/1.3059850.

[56] O. Klein and Y. Nishina. *Über die Streuung von Strahlung durch freie Elektronen nach der neuen relativistischen Quantendynamik von Dirac.* Zeitschrift für Physik, volume 52 (1929)(11): pp. 853–868. ISSN 0044-3328. URL https://doi.org/10.1007/BF01366453.

[57] F. H. Attix. *Introduction to Radiological Physics and Radiationdosimetry.* John Wiley & Sons, Nashville, TN, 1986.

[58] I. Obodovskiy. *Chapter 7 - interaction of neutrons with matter.* In I. Obodovskiy (Editor), *Radiation*, (pp. 151–160). Elsevier, 2019. ISBN 978-0-444-63979-0. URL https://www.sciencedirect.com/science/article/pii/B9780444639790000070.

[59] *Neutron Slowing Down*, chapter 10, (pp. 385–414). John Wiley Sons, Ltd, 2007. ISBN 9783527611041. URL https://onlinelibrary.wiley.com/doi/abs/10.1002/9783527611041.ch10.

[60] D. R. McAlister. *Neutron shielding materials*, 1955. URL https://www.eichrom.com/wp-content/uploads/2018/02/neutron-attenuation-white-paper-by-d-m-rev-2-1.pdf.

[61] D. Kwatra, A. Venugopal and S. Anant. *Nanoparticles in radiation therapy: a summary of various approaches to enhance radiosensitization in cancer.* Translational Cancer Research, volume 2 (2013)(4). ISSN 2219-6803. URL https://tcr.amegroups.com/article/view/1550.

[62] A. Russo, J. Mitchell, T. Kinsella et al. *Determinants of radiosensitivity.* Semin Oncol, volume 12 (1985)(3): pp. 332–349.

[63] D. E. Citrin and J. B. Mitchell. *Altering the response to radiation: sensitizers and protectors.* Semin Oncol, volume 41 (2014)(6): pp. 848–859.

[64] S. Barua and S. Mitragotri. *Challenges associated with Penetration of Nanoparticles across Cell and Tissue Barriers: A Review of Current Status and Future Prospects.* Nano Today, volume 9 (2014)(2): pp. 223–243.

[65] T. Shukla, N. Upmanyu, S. P. Pandey et al. *Chapter 14 - site-specific drug delivery, targeting, and gene therapy.* In A. M. Grumezescu (Editor), *Nanoarchitectonics in Biomedicine*, (pp. 473–505). William Andrew Publishing, 2019. ISBN 978-0-12-816200-2. URL https://www.sciencedirect.com/science/article/pii/B978012816200200013X.

[66] K. Greish. *Enhanced permeability and retention (EPR) effect for anticancer nanomedicine drug targeting.* Methods in molecular biology (Clifton, N.J.), volume 624 (2010): pp. 25–37.

[67] J. Wu. *The Enhanced Permeability and Retention (EPR) Effect: The Significance of the Concept and Methods to Enhance Its Application.* J Pers Med, volume 11 (2021)(8).

[68] K. Haume, S. Rosa, S. Grellet et al. *Gold nanoparticles for cancer radiotherapy: a review.* Cancer Nanotechnology, volume 7 (2016)(1): p. 8. ISSN 1868-6966. URL https://doi.org/10.1186/s12645-016-0021-x.

[69] S. Her, D. A. Jaffray and C. Allen. *Gold nanoparticles for applications in cancer radiotherapy: Mechanisms and recent advancements.* Advanced Drug Delivery Reviews, volume 109 (2017): pp. 84–101. ISSN 0169-409X. URL https://www.sciencedirect.com/science/article/pii/S0169409X15300144. Radiotherapy for cancer: present and future.

[70] Y. Lin, S. J. McMahon, M. Scarpelli et al. *Comparing gold nano-particle enhanced radiotherapy with protons, megavoltage photons and kilovoltage photons: a Monte Carlo*

simulation. Physics in Medicine and Biology, volume 59 (2014)(24): pp. 7675–7689. ISSN 1361-6560.

[71] A. N. DuRoss, M. J. Neufeld, S. Rana et al. *Integrating nanomedicine into clinical radiotherapy regimens*. Adv Drug Deliv Rev, volume 144 (2019): pp. 35–56.

[72] C. Kim, W. Lee, A. Melis et al. *A review of inorganic scintillation crystals for extreme environments*. Crystals, volume 11 (2021)(6). ISSN 2073-4352. URL `https://www.mdpi.com/2073-4352/11/6/669`.

[73] J. B. Birks. *The Theory and Practice of Scintillation Counting*. Elsevier, 1964.

[74] S. Min, H. Kang, B. Seo et al. *A review of nanomaterial based scintillators*. Energies, volume 14 (2021)(22). ISSN 1996-1073. URL `https://www.mdpi.com/1996-1073/14/22/7701`.

[75] M. F. L'Annunziata. *11 - Solid Scintillation Analysis*. In M. F. L'Annunziata (Editor), *Handbook of Radioactivity Analysis (Second Edition)*, (pp. 845–987). Academic Press, San Diego, second edition edition, 2003. ISBN 978-0-12-436603-9. URL `https://www.sciencedirect.com/science/article/pii/B9780124366039500168`.

[76] Enlitech. *Brief introduction and guidance of characterization for photodiodes*, 2022. URL `https://enlitechnology.com/blog/pd/photodetector-01/`.

[77] S. Gundacker and A. Heering. *The silicon photomultiplier: fundamentals and applications of a modern solid-state photon detector*. Physics in Medicine &amp Biology, volume 65 (2020)(17): p. 17TR01. URL `https://doi.org/10.1088/1361-6560/ab7b2d`.

[78] M. Rizzi, M. D`Aloia and B. Castagnolo. *Semiconductor detectors and principles of radiation-matter interaction*. Journal of Applied Sciences, volume 10 (2010)(23): pp. 3141–3155. URL `https://doi.org/10.3923/jas.2010.3141.3155`.

[79] S. H. Byun. *Radioisotopes and radiation methodology: Med phys 4r06/6r03*.

[80] V. Valkovic. *Radioactivity in the environment*. Elsevier Science, London, England, 2 edition, 2019.

[81] W. R. Leo. *Semiconductor Detectors*, (pp. 215–247). Springer Berlin Heidelberg, Berlin, Heidelberg, 1994. ISBN 978-3-642-57920-2. URL https://doi.org/10.1007/978-3-642-57920-2_10.

[82] Mirion Technologies. *High-resolution gamma-ray spectroscopy with HPGe detectors*. URL https://www.mirion.com/learning-center/lab-experiments/high-resolution-gamma-ray-spectroscopy-with-hpge-detectors-lab-experiments.

[83] U. Fano. *Ionization Yield of Radiations. II. The Fluctuations of the Number of Ions*. Phys. Rev., volume 72 (1947): pp. 26–29. URL https://link.aps.org/doi/10.1103/PhysRev.72.26.

[84] S. Samat and W. Priharti. *Determination of Fano factor and pre-amplifier noise from the measurement of energy resolution of a HPGe detector*. Sains Malaysiana, volume 44 (2015): pp. 761–764.

[85] S. Croft and D. Bond. *A determination of the Fano factor for germanium at 77.4 K from measurements of the energy resolution of a 113 cm^3 HPGe gamma-ray spectrometer taken over the energy range from 14 to 6129 keV*. International Journal of Radiation Applications and Instrumentation. Part A. Applied Radiation and Isotopes, volume 42 (1991)(11): pp. 1009–1014. ISSN 0883-2889. URL https://www.sciencedirect.com/science/article/pii/088328899190002I.

[86] CAEN - Tools for Discovery. *DT5730 / DT5730S - 8 channel 14 bit 500 ms/s digitizer - CAEN - Tools for Discovery. [online]*. https://www.caen.it/products/dt5730/, 2022.

[87] S. H. Ahn, N. Lee, C. Choi et al. *Feasibility study of Fe_3O_4/TaO_x nanoparticles as a radiosensitizer for proton therapy*. Physics in Medicine & Biology, volume 63 (2018)(11): p. 114,001. URL https://doi.org/10.1088/1361-6560/aac27b.

[88] X. Zhang, Z. Liu, Z. Lou et al. *Radiosensitivity enhancement of Fe_3O_4@Ag nanoparticles on human glioblastoma cells*. Artificial Cells, Nanomedicine, and Biotechnology, volume 46 (2018)(sup1): pp. 975–984. URL https://doi.org/10.1080/21691401.2018.1439843. PMID: 29609505.

[89] M. Xiao. *Spectroscopy-aided prompt gamma-ray imaging for real-time range verification in proton therapy.* Ph.D. thesis, University of York, 2020.

[90] C. Saint-Gobain. *CLLB Material Datasheet*, 2022. URL `https://www.crystals.saint-gobain.com/sites/hps-mac3-cma-crystals/files/2021-09/CLLB-Material-Data-Sheet.pdf`.

[91] Saint-Gobain Crystals. *CLLB scintillation crystal.* `https://www.crystals.saint-gobain.com/radiation-detection-scintillators/crystal-scintillators/cllb`, 2022.

[92] CAEN - Tools for Discovery. *DPP-PHA: Digital Pulse Processing for the Pulse Height Analysis.* `https://www.caen.it/products/dpp-pha/`, 2022.

[93] M. Moralles, D. Bonifacio, E. Okuno et al. *Applications of the Monte Carlo method in nuclear physics using the GEANT4 toolkit.* volume 1139. 2009.

[94] P. Andreo. *Monte Carlo techniques in medical radiation physics.* Physics in medicine and biology, volume 36 (1991): pp. 861–920.

[95] S. Agostinelli, J. Allison, K. Amako et al. *Geant4—a simulation toolkit.* Nuclear Instruments and Methods in Physics Research Section A: Accelerators, Spectrometers, Detectors and Associated Equipment, volume 506 (2003)(3): pp. 250–303. ISSN 0168-9002. URL `https://www.sciencedirect.com/science/article/pii/S0168900203013688`.

[96] Geant4. *Physics reference manual - physics reference manual 11.0 documentation.* `https://geant4-userdoc.web.cern.ch/UsersGuides/PhysicsReferenceManual/html/index.html`, 2022.

[97] D. Wright and S. Incerti. *A short guide to choosing physics lists - geant4.* URL `http://geant4.in2p3.fr/IMG/pdf_PhysicsLists.pdf`.

[98] P. Arce, D. Bolst, M.-C. Bordage et al. *Report on G4-Med, a Geant4 benchmarking system for medical physics applications developed by the Geant4 Medical Simulation Benchmarking Group.* Medical Physics, volume 48 (2021)(1): pp. 19–56. URL `https://aapm.onlinelibrary.wiley.com/doi/abs/10.1002/mp.14226`.

[99] R. Gabbasov, M. Polikarpov, V. Safronov et al. *Monte Carlo simulation of dose distribution in water around $^{57}Fe_3O_4$ magnetite nanoparticle in the nuclear gamma resonance condition.* Hyperfine Interactions, volume 237 (2016)(1). URL `https://doi.org/10.1007/s10751-016-1267-8`.

[100] S. Khoei, S. Mahdavi, H. Fakhimikabir et al. *The Role of Iron Oxide Nanoparticles in the Radiosensitization of Human Prostate Carcinoma Cell Line DU145 at Megavoltage Radiation Energies.* International journal of radiation biology, volume 90 (2014).

[101] P. Gonçalves. *Introductory course on Geant4: Sensitive detectors.* `https://indico.lip.pt/event/681/contributions/2103/attachments/1907/2542/Geant4_SD.pdf`, 2022.

[102] M. D. Whitfield. *Doppler-Broadening of Light Nuclei Gamma-Ray Spectra*, 2010.

[103] M. Rawool-Sullivan and J. P. Sullivan. *Understanding Doppler Broadening of Gamma Rays.* URL `https://www.osti.gov/biblio/1130509`.

[104] B. Kozlovsky, R. J. Murphy and R. Ramaty. *Nuclear deexcitation gamma-ray lines from accelerated particle interactions.* The Astrophysical Journal Supplement Series, volume 141 (2002)(2): pp. 523–541. URL `https://doi.org/10.1086/340545`.

[105] National Institute of Standards and Technology. *Atomic weights and isotopic compositions for iron.* `https://physics.nist.gov/cgi-bin/Compositions/stand_alone.pl?ele=Fe`, 2022.

[106] C. C. Chang, N. S. Wall and Z. Fraenkel. *Gamma rays observed from 100-MeV protons interacting with* ^{56}Fe *and* ^{58}Ni. Phys. Rev. Lett., volume 33 (1974): pp. 1493–1496. URL `https://link.aps.org/doi/10.1103/PhysRevLett.33.1493`.

[107] University of York. *Viking - University of York Research Computing Cluster.* URL `https://wiki.york.ac.uk/display/RCS/Viking+-+University+of+York+Research+Computing+Cluster`.

[108] D. Parker and C. Wheldon. *The Birmingham MC40 Cyclotron Facility.* Nuclear Physics News, volume 28 (2018): pp. 15–20.

[109] S. Seltzer. *Stopping-powers and range tables for electrons, protons, and helium ions, NIST Standard Reference Database 124*, 1993. URL `http://www.nist.gov/pml/data/star/index.cfm`.

[110] S. I. Sukhoruchkin and Z. N. Soroko. *Excited Nuclear States for Fe-56 (Iron): Datasheet from Landolt-Börnstein - Group I Elementary Particles, Nuclei and Atoms.* URL `https://materials.springer.com/lb/docs/sm_lbs_978-3-662-48875-1_255`. Copyright 2016 Springer-Verlag Berlin Heidelberg.